DISS. ETH NO. 26785

HYBRID BICOMPONENT FIBRES *for* THERMOPLASTIC COMPOSITES

Towards New Intermediate Materials for High Volume Manufacturing using Stamp Forming

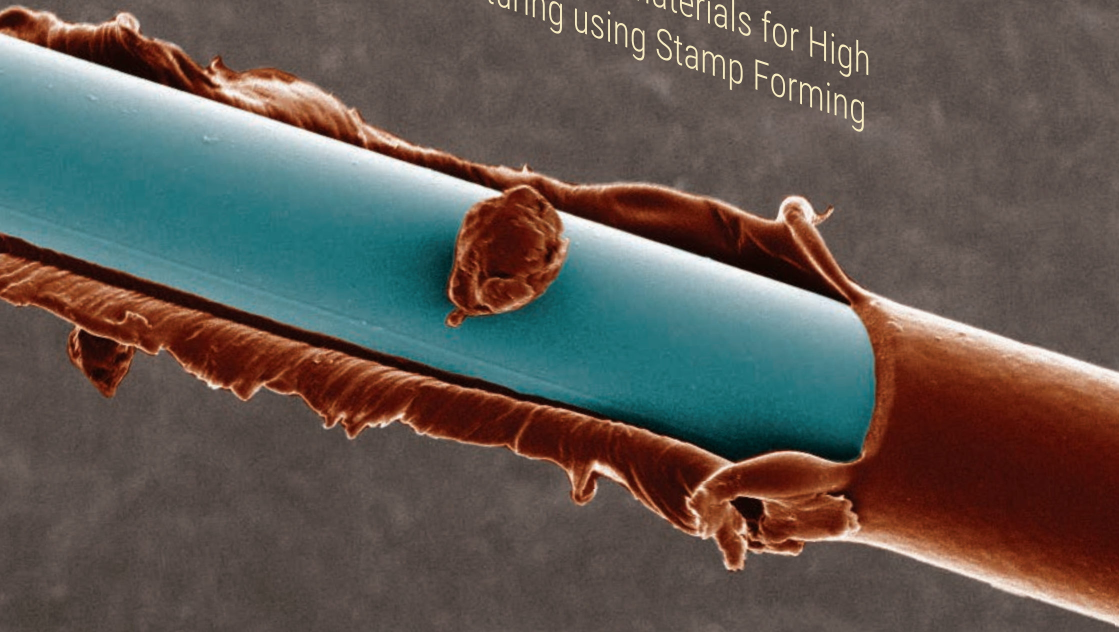

presented by

CHRISTOPH SCHNEEBERGER

DISS. ETH NO. 26785

HYBRID BICOMPONENT FIBRES *for* THERMOPLASTIC COMPOSITES

Towards New Intermediate Materials for High Volume Manufacturing using Stamp Forming

A thesis submitted to attain the degree of
DOCTOR OF SCIENCES *of* **ETH ZURICH**
(Dr. sc. ETH Zurich)

presented by

CHRISTOPH SCHNEEBERGER

Master of Science ETH in Mechanical Engineering
born on 07.06.1988
citizen of Madiswil BE

accepted on the recommendation of
Prof. Dr. Paolo Ermanni, examiner
Prof. Dr. Joanna C.H. Wong, co-examiner
Dr. Shelly Arreguin, co-examiner

2020

©2020
Christoph Schneeberger
All rights reserved

ABSTRACT

Hybrid preforms are used in thermoplastic composite manufacturing processes to reduce the potentially long consolidation times caused by the high viscosities of thermoplastic melts. Darcy's law for fluid flow through a porous medium indicates that the negative effects of high viscosities on impregnation time can be offset by reducing the maximum distances the thermoplastic melts must flow for complete consolidation. In thermoplastic composite preforms, the total impregnation length is reduced by increasing the degree of mingling between reinforcement and matrix. Currently, mingling in such preforms is found on the level of the laminate down to the level of the yarn, but may occur on any of the hierarchical tiers found in fibre-reinforced composite materials. The level and quality of mingling in existing arrangements – such as organosheets, commingled yarns, powder-impregnated yarns and fibre impregnated thermoplastics (FITs), co-woven yarns or stacked laminates – greatly influence the flow lengths, cycle times, achievable part complexity, raw material costs, and suitable manufacturing routes. Given the limited selection of commercially available preform architectures, manufacturers must choose between the low cycle times of organosheets and the better drapeability of unconsolidated hybrids, e.g. commingled yarns, in thermoforming. The development of a material architecture which combines the fast processing of fully impregnated products with the flexibility of unconsolidated preforms would render thermoplastic composites significantly more attractive to high volume production markets, e.g. automotive parts.

This thesis proposes hybrid bicomponent fibres – which consist of continuous reinforcement fibres individually sheathed in a thermoplastic polymer – as a new class of preform materials for thermoplastic composites. By reducing the scale of mingling between the reinforcement and matrix materials to the level of the fibre, a full wet-out of the fibres is ensured while the unconsolidated nature of the material allows the fibres to shift and deform with respect to each other to ensure drapeability even at room temperature. It is hypothesized that preforms made from hybrid bicomponent fibres can be stamp formed with cycle times similar to those of pre-consolidated blanks. Furthermore, it is expected that the void content of laminates stamp formed from hybrid bicomponent fibre preforms is greatly influenced by sintering mechanisms and the removal and/or collapse of air pockets. The presented research aims to answer these hypotheses by developing suitable methods to manufacture such hybrid bicomponent fibres and by processing them into consolidated laminates.

The basic idea of hybrid bicomponent fibres is motivated and introduced in further detail in part I. Part II moves on to discuss materials and their corresponding processing methods for their suitability in realizing bicomponent fibres. A fibre forming approach based on glass-melt spinning combined with an in-line coating process is chosen. Multiple versions of the latter are investigated empirically, namely dip-coating of newly spun glass fibres in either a polymer solution or a sparsely nanofilled polymer melt, as well as the so-called kiss-roll coating method. It is found that drawing glass monofilaments of finite length over a rotating roll which is partially immersed in a dilute polymer solution yields a coating method which can endure high fibre velocities while ensuring the deposition of a sufficiently thick thermoplastic sheath for down-stream conversion into a structural grade composite laminate. The validity of this strategy is proven in the realization of a pilot plant which employs solution kiss-roll coating in-line with melt-spinning of a glass monofilament for the continuous fabrication of bicomponent fibres.

Unidirectional layups of specimens of aluminium borosilicate glass fibres clad in polycarbonate produced with the pilot plant were characterized for their consolidation behaviour, the results of which are reported in part III. Supported by theoretical treatments on issues related to void collapse and autohesion, a parameter study on rapid stamp forming of these preforms was performed and complemented with stamp forming trials processing cross-ply layups of different thicknesses. All experiments yielded excellent laminate qualities with void contents $< 0.7\,\%$, supporting the conclusion that issues related to air removal and void collapse are insignificant. Laminates with a consolidated thickness of 1 mm and a fibre volume content of 0.69 were consolidated with holding times inside the press as low as 5 s, illustrating that virgin hybrid bicomponent fibre preforms can be stamp formed with similar process parameters as pre-consolidated blanks.

Overall, it is concluded that the concept of hybrid bicomponent fibres as a novel type of preform provides enormous advantages for manufacturing continuous fibre-reinforced thermoplastic polymer composites.

The combined value chain of stamp forming solution kiss-roll coated glass fibres offers a first opportunity for the production of continuous fibre-reinforced polymer composites without relying on Darcian impregnation flows anywhere between fibre formation and part production. The research presented in this thesis provides experimental proof for these claims and has established pilot equipment for the continuous spinning of glass/thermoplastic polymer bicomponent fibres, bringing this potentially disruptive technology closer to reality and expediting the adaptation of thermoplastic composites for high volume manufacturing.

ZUSAMMENFASSUNG

Hybride Halbzeuge werden bei der Herstellung von thermoplastischen Verbundwerkstoffen verwendet, um die potenziell langen Konsolidierungszeiten zu reduzieren, die durch die hohe Viskosität der thermoplastischen Schmelzen verursacht werden. Das Darcy-Gesetz für den Fluss durch ein poröses Medium hat zur Folge, dass die negativen Auswirkungen hoher Viskositäten auf die Imprägnierungszeit durch die Reduzierung der maximalen Abstände, welche die thermoplastischen Schmelzen für eine vollständige Konsolidierung fliessen müssen, ausgeglichen werden können. Bei thermoplastischen Verbundhalbzeugen wird die Gesamtdauer der Imprägnierung durch eine Erhöhung des Vermischungsgrades zwischen Verstärkung und Matrix verringert. Gegenwärtig findet die Vermischung in solchen Vorformen auf der Ebene des Laminats bis hinunter zum Garn statt, kann aber auf jeder der hierarchischen Ebenen erfolgen, die in faserverstärkten Verbundwerkstoffen vorkommen. Das Niveau und die Qualität der Vermischung in bestehenden Anordnungen – wie z.B. Organoblechen, Mischgarnen, pulverimprägnierten Garnen, Mischgeweben oder gestapelten Laminaten – haben grossen Einfluss auf die Fliesslängen, die Zykluszeiten, die erreichbare Bauteilkomplexität, die Rohstoffkosten und die geeigneten Fertigungswege. Angesichts der begrenzten Auswahl kommerziell verfügbarer Halbzeugarchitekturen müssen Hersteller beim Thermoformen zwischen den niedrigen Zykluszeiten von Organoblechen und der besseren Drapierbarkeit von unkonsolidierten Hybriden, z.B. Mischgarnen, wählen. Die Entwicklung einer Materialarchitektur, welche die schnelle Verarbeitung voll imprägnierter Produkte mit der Flexibilität unkonsolidierter Rohlinge kombiniert, würde die Attraktivität thermoplastischer Verbundwerkstoffe für Märkte mit hohen Produktionsvolumen, z.B. für Automobilteile, deutlich erhöhen.

Diese Dissertation schlägt hybride Bikomponentenfasern – die aus kontinuierlichen Verstärkungsfasern bestehen, welche einzeln mit einem thermoplastischen Polymer umhüllt sind – als eine neue Klasse von Halbzeugen für thermoplastische Verbundwerkstoffe vor. Durch die Reduzierung des Ausmasses der Vermischung zwischen den Verstärkungs- und Matrixmaterialien auf das Niveau der Faser wird eine vollstän-

dige Benetzung der Fasern gewährleistet, während die unverfestigte Natur des Materials es den Fasern erlaubt, sich gegeneinander zu verschieben und zu verformen, um auch bei Raumtemperatur eine hohe Drapierbarkeit zu gewährleisten. Es wird angenommen, dass Rohlinge aus hybriden Bikomponentenfasern mit ähnlichen Zykluszeiten wie vorverpresste Halbzteuge stempelgeformt werden können. Darüber hinaus wird erwartet, dass der Porengehalt stempelgeformter Laminate aus hybriden Bikomponenten-Faser-Halbzeugen stark durch Sintermechanismen und die Entfernung und/oder den Kollaps von Lufteinschlüssen beeinflusst wird. Die vorgestellte Forschung hat zum Ziel, diese Hypothesen durch die Entwicklung geeigneter Methoden zur Herstellung solcher hybriden Bikomponentenfasern und deren Verarbeitung zu verfestigten Laminaten zu beantworten.

Die Grundidee der hybriden Bikomponentenfasern wird im Teil I motiviert und näher vorgestellt. In Teil II werden Materialien und ihre entsprechenden Verarbeitungsmethoden hinsichtlich ihrer Eignung zur Realisierung von Bikomponentenfasern diskutiert. Es wird ein Faserformungsansatz gewählt, der auf dem Glasschmelzspinnen in Kombination mit einem Inline-Beschichtungsverfahren basiert. Letzteres wird in mehreren Varianten empirisch untersucht, nämlich als Tauchbeschichtung von neu gesponnenen Glasfasern entweder in einer Polymerlösung oder in einer spärlich nanogefüllten Polymerschmelze, sowie als sogenannte Kuss-Rollenbeschichtung. Es wird festgestellt, dass das Ziehen von Glasmonofilamenten endlicher Länge über eine rotierende Walze, die teilweise in eine verdünnte Polymerlösung eingetaucht ist, eine Beschichtungsmethode ergibt, welche hohe Fasergeschwindigkeiten erlaubt und gleichzeitig die Ablagerung einer ausreichend dicken thermoplastischen Hülle für die weitere Umwandlung in ein Verbundlaminat von struktureller Qualität gewährleistet. Die Gültigkeit dieser Strategie wird durch die Realisierung einer Pilotanlage bewiesen, welche die Lösungs-Kuss-Rollenbeschichtung in einer Linie mit dem Schmelzspinnen eines Glasmonofilaments für die kontinuierliche Herstellung von Bikomponentenfasern einsetzt.

Mit der Pilotanlage hergestellte unidirektionale Lagen von mit Polycarbonat ummantelten Proben aus Aluminium-Borosilikat-Glasfasern wurden hinsichtlich ihres Konsolidierungsverhaltens charakterisiert, über deren Ergebnisse in Teil III berichtet wird. Unterstützt durch theoretische Behandlungen zu Fragen des Porenkollapses und der Autohäsion wurde eine Parameterstudie zur schnellen Stempelformung dieser Vorformen durchgeführt und durch Versuche ergänzt, bei denen kreuzweise gestapelte Laminate unterschiedlicher Dicke verarbeitet wurden. Alle Experimente ergaben ausgezeichnete Laminatqualitäten mit einem Porengehalt von $< 0.7\,\%$, was die Schlussfolgerung stützt, dass Probleme im Zusammenhang mit Luftentfernung und Porenkollaps unbedeutend sind. Laminate mit einer verpressten Dicke von 1 mm und einem Faservolumengehalt von 0.69 wurden mit Haltezeiten in der Presse von nur 5 s konsolidiert, was zeigt, dass neue hybride Bikomponentenfaser-Halbzeuge mit ähnlichen Prozessparametern wie vorverpresste Rohlinge verarbeitet werden können.

Insgesamt kommt man zu dem Schluss, dass das Konzept der hybriden Bikomponentenfasern als neuartiges Halbzeug enorme Vorteile für die Herstellung endlosfaserverstärkter thermoplastischer Kunststoffverbunde bietet. Die kombinierte Wertschöpfungskette stempelgeformter kuss-rollenbeschichteter Glasfasern bietet eine erste Möglichkeit zur Herstellung von endlosfaserverstärkten Polymerverbundwerkstoffen, ohne irgendwo zwischen Faserbildung und Bauteilproduktion auf Imprägnierungsflüsse gemäss Darcy angewiesen zu sein. Die in dieser Arbeit vorgestellte Forschung liefert den experimentellen Beweis für diese Behauptungen und hat eine Pilotanlage für das kontinuierliche Spinnen von Glas-/Thermoplast-Bikomponentenfasern etabliert, wodurch diese potenziell disruptive Technologie näher an die Realität herangeführt und die Adaptierung thermoplastischer Verbundwerkstoffe für die Grossserienfertigung beschleunigt wird.

Dedicated to my parents Doris & Hansjörg Schneeberger-Thaler,
who enabled and encouraged me to get an academic education,
and to my wife Elena,
for her unconditional love and support.

ACKNOWLEDGMENTS

First and foremost, I would like to acknowledge the various funding agencies which supported my research: the Swiss National Science Foundation (grant № 200021_165994), for the project grant which funded most of my salary and material expenses; the Swiss Innovation Agency (Innosuisse) through the Swiss Competence Center for Energy Research (SCCER) Efficient Technologies and Systems for Mobility, for the complementary funds supporting my salary; and the Scientific Equipment Program of ETH Zurich, for granting the bulk of the acquisition costs of the glass monofilament spinning machine.

I wish to express my deepest gratitude to my supervisor, Paolo Ermanni, for approaching me with the proposal to enlist as a doctoral student, for allowing me to choose my area of research and make it my own, and for supporting me all the way through with technical guidance, career advice, and supplementary funds. Thank you for keeping an open mind during our many discussions, for coming up with new challenges for our technological developments, for taking an interest in my personal development, and last but not least for your expertise, your candour, and your passion for the work we did together. It has been an immense pleasure and I am very much looking forward to many more fruitful discussions in the future.

I am indebted to my co-advisor, Joanna Wong, and would like to recognize the invaluable assistance she provided during my doctoral studies. Thank you for taking Paolo's place during the first minutes of the meeting that started my journey down the rabbit hole lined with orange-brown plastic and seemingly invisible strands of glass. Looking back, it almost seems like a fairytale that you should greet me with my dream-project at the ready and that we made it all the way through to the other end, carrying riches of continuously spun fibre cakes glistening with snow-white coatings. Thank you for putting your trust in me, for teaching me almost everything I know about material science, for sharing an office, an Airbnb, your new laboratory, and a Canadian Thanksgiving with me, and for finding the good in every aspect of life as a researcher.

As my third co-advisor, Shelly Arreguin deserves no less than my sincerest appreciation for the support she provided me with since day one at the office. Thank you for not just thinking outside the box, but for over-analysing every side, edge, and corner from both sides, for being my greatest critic and a patient language and communications teacher, and for always including passion and encouragement in even the most fact-driven discussions.

I would like to pay my special regards to Nicole Aegerter, my Master's student turned partner in crime. Who would have thought that I would ever come across someone so persistent when tasked with the gargantuan dullness that is "fibre separation yoga". Thank you for all the hard work during your past two theses and for the support you have continuously provided since becoming my most trusted colleague. I could not have wished for a better research partner and I am most excited to find out what the future has in store for us.

Most of the work presented in this thesis would not have been realized without the help of many students, whose various theses I had the pleasure to advise. I wish to express my sincere appreciation to the following mechanical engineers and material scientists: Vincent Werlen, Jialu "Mary" Chen, Dominik Kläusler, Audrey Blondé, Paul Schwager, Ivo Marti, Philipp Bischof, Manuela Heinrich, Kerstin Unmüssig, Philipp Keller, and Sara Birk.

As a member of the SCCER Mobility community, I had the immense pleasure to collaborate with some of Switzerland's top scientists in their respective fields, to exchange and discuss results and ideas, and to present my research to a broader audience, both academic and public. Thank you to the members of capacity area A3 for the many enlightening discussions; to the management office for the great support in all matters concerning administration, reporting, and dissemination; to the Complex Materials group at ETH Zürich for use of their scanning electron microscope; and to the Institute of Polymer Engineering at the FHNW School of Engineering for access to and assistance with their drop shape analyser. Furthermore, I would like to recognize the Soft Materials laboratory at ETH Zürich for access to and assistance with their rheometer.

My experimental work depended on the supply of suitable materials and sufficient amounts thereof, some of which were donated in kind: my sincere gratitude goes to Rudolf "Rudy" Koopmans, formerly of Dow Europe GmbH, for providing the poly(ester-amide); to Prof. Edith Mäder of the Leibnitz Institute of Polymer Research Dresden for supplying the glass fibre rovings used prior to the acquisition of our own spinning line; to Fabian Starsich, formerly of the Particle Technology Laboratory at ETH Zürich for providing the silica nanoparticles; and to Thomas Grimm of Covestro Deutschland AG for providing the polycarbonate.

All doctoral research projects, and experiment-based studies in particular, require a great deal of administrative and technical assistance. Thank you to Désirée Hess for administering my project funds; to Martina Rizzoli for taking over the funds administration, for supporting me in every other way possible, and for always sharing chocolates and coffee; and to Thomas Heinrich, Hanspeter "Hampi" Eigenmann, and Markus Müller for the provided support in the laboratories and the workshop and for the many helpful technical exchanges.

I wish to thank all the employees, alumni, and friends of the Laboratory of Composite Materials and Adaptive Structures with whom I have interacted over the past five years for the times we spent together. I feel honoured to have worked among such a diverse group of excellent researchers and I am thankful for the many technical discussions, private exchanges, ski-weekends, hikes, climbing trips, coffees, beers, laughs, and other niceties of life we have shared. You have all contributed to making our shared work and recreational activities a delight.

Last, but by no means least, I would like to thank my family: Ma, Pa, danke för euchi Onderstötzig ond Ermuetigong, dass der mer s'Studium ade ETH ermöglecht hend ond dass der emmer dra gloubt hend, dass min Plan ufgoht. Pa, merci för dini weise Wort wo mech devo öberzügt hend, dasi met mim Doktorat en eimoligi Möglechkeit becho ha, öppis z'entwickle, woni döf stolz druf si. Elena, danke besch du emmer of ond a minere Siite ond gesch du mer d'Freiheit woni bruuche, zom erfolgriich die Arbet chönne z'mache, wo mer wechtig esch. Danke dass du en Fröndin vom CMASLab worde besch ond dass du öis so mängisch met dine Bachkönst beglöckt hesch. Ond aune andere Schneebergers, Thalers, Oberlis ond Zueghörige, merci för euches Interesse a minere Arbet ond mim Wohlbefinde ond dasi be euch ou eifach mol ha döffe abschalte. Tuusig Dank euch aune!

CONTENTS

Abstract v

Zusammenfassung ix

Acknowledgments xv

Nomenclature xxv

I Introduction 1

1 On the importance of lightweighting and efficient composites production 3
- 1.1 Green house gas emissions in Switzerland 4
- 1.2 Efficiency through lightweighting 6
- 1.3 The role of composites in transport 7

2 State of the art 11
- 2.1 Advantages of thermoplastic matrix polymers 11
- 2.2 Thermoplastic matrix preforms 15
- 2.3 Stamp forming 17

3 Hybrid bicomponent fibres 21
- 3.1 On the idea of a perfect preform 22
- 3.2 Hypotheses 24
- 3.3 State of the art in bicomponent fibres 25

II Fabrication 29

4 Material and process selection 31
- 4.1 Reinforcing fibre materials 31
  - 4.1.1 Organic fibres 32
  - 4.1.2 Inorganic fibres 34

4.2 A brief overview of sheathing processes 38

5 Glass fibre spinning **41**
5.1 The direct roving process 42
5.2 Theory of glass melt spinning 44

6 Solution dip-coating **49**
6.1 Properties of coating materials 50
  6.1.1 Density 51
  6.1.2 Rheology 51
  6.1.3 Surface tension 53
6.2 Theory of dip-coating 55
  6.2.1 Potential in-line processing window 57
6.3 Experiments 60
  6.3.1 Reinforcement fibres and coating process 60
  6.3.2 Scanning electron microscopy (SEM) 61
  6.3.3 Image processing 62
  6.3.4 Results and discussion 65
6.4 Comparison of experimental and predicted results . . . 72
6.5 Conclusion 73

7 Dip-coating in a nanofilled hot melt **77**
7.1 Viscosity reduction through nanofilling 77
7.2 Experiments 79
  7.2.1 Sample preparation 79
  7.2.2 Thermal analysis 80
  7.2.3 Rheology 80
  7.2.4 Surface tension 80
  7.2.5 Dip-coating 81
  7.2.6 Imaging 81
7.3 Results and discussion 83
  7.3.1 Observation of decrease in viscosity 83
  7.3.2 Dip-coating of fibres 88
7.4 Conclusion 94
  7.4.1 Potential for bicomponent fibres 94

8 Solution kiss-roll coating 97
8.1 The kiss-roll method 98
8.2 Parameter study 99
8.2.1 Materials and coating setup 99
8.2.2 Design of experiment 100
8.2.3 Imaging 101
8.2.4 Modelling the fluid film on the kiss-roll 102
8.3 Results and discussion 104
8.3.1 Predicted fluid film thickness on roll 104
8.3.2 Results of the parameter study 105
8.4 Conclusion 111

9 In-line coating pilot plant 113
9.1 In-line coating study 115
9.1.1 Spinning and in-line coating 115
9.1.2 Thermogravimetric analysis (TGA) 116
9.1.3 Results and discussion 116
9.1.4 Conclusion 119

III Processing 121

10 Consolidation in theory 123
10.1 Deformation of the molten sheaths 123
10.1.1 Modelling approach 124
10.1.2 Results 125
10.1.3 Comments on void formation and stability . . . 126
10.2 Autohesion of the matrix interfaces 127
10.3 Cooling inside the press 129

11 Achievable consolidation quality and preform void content 133
11.1 Sample preparation 133
11.2 Compression moulding 135
11.3 Microstructure after heating 136

12 Stamp forming experiments 141
12.1 Materials and methods 141
12.1.1 Stamp forming of the samples 141
12.1.2 Imaging 142

12.2 Results and discussion 144
12.2.1 Results of the parameter study 144
12.2.2 Results of the cross-ply trials 147
12.3 Conclusion 150

IV Conclusion **153**

13 Concluding remarks **155**
13.1 Hybrid bicomponent fibre fabrication 156
13.2 Processing hybrid bicomponent fibres 158

14 Outlook **163**

Bibliography **169**

List of publications **181**

Curriculum vitae **185**

NOMENCLATURE

Note that some values are denoted with alternative symbols depending on context and that some symbols are used to denote multiple values. In the latter cases, the different definitions are separated by commas.

Physical values

Φ	Porosity, void volume fraction
Φ_0	Unconsolidated porosity, void volume content
$\dot{\gamma}$	Shear rate
γ	Surface tension, shear strain
γ_m	Surface tension of matrix
η	Dynamic viscosity
η_g	Glass melt viscosity
η_l	Viscosity of pure (unfilled) liquid
θ_c	Supplementary angle of contact (obtuse)
θ_i	Angle of inspection
λ_c	Thermal conductivity of composite
λ_f	Thermal conductivity of fibre
λ_m	Thermal conductivity of matrix
λ_p	Thermal conductivity of tool platen
ρ	Density
ρ_c	Density of composite
ρ_f	Density of fibre
ρ_g	Density of glass
ρ_m	Density of matrix
ρ_p	Density of polymer, density of tool platen
ρ_s	Density of solvent
φ	Particle volume fraction
$\varphi_{\mathrm{SiO_2}}$	Silica particle volume fraction
$\overline{D_c}$	Mean core diameter
$D_{c,j}$	Diameter of glass core j
$D_{p,i}$	Diameter of coated fibre at position i
$\mathbf{F}$	Force vector

$\mathbf{K}$	Permeability tensor
K	Consistency index
K_l	Average consistency index of pure (unfilled) liquid
L	Length
M_w	Molecular weight
Q_v	Volumetric flow rate
R	Resistance to flow, kiss-roll radius
T	Image segmentation threshold value, temperature
T_0	Initial temperature
T_A	Onset of degradation temperature
T_g	Glass transition temperature
$T_{g,\infty}$	Limiting glass transition temperature for infinite molecular weight
T_p	Press temperature
T_{pm}	Peak melt temperature
U	Peripheral kiss-roll velocity
V	Fibre velocity, withdrawal velocity
$\mathbf{a}$	Acceleration vector
$c_{p,c}$	Specific heat capacity of composite
$c_{p,f}$	Specific heat capacity of fibre
$c_{p,m}$	Specific heat capacity of matrix
$c_{p,p}$	Specific heat capacity of tool platen
d	Diameter, Cohen's d (effect size)
$\overline{d_c}$	Mean core diameter
d_c	Core diameter
$d_{t,i}$	Total coated thickness at position i
d_v	Void diameter
g	Gravitational acceleration
$\hat{h}$	Film thickness at the apex of the roll
$\overline{h}$	Mean coating thickness
h	Coating thickness, laminate thickness after consolidation
h_0	Limiting constant film thickness
h_c	Laminate thickness
h_g	Glass melt filling height
h_i	Coating thickness at position i
h_l	Liquid coating thickness

$h_{l,\mathrm{DRQ}}$	Liquid coating thickness estimate after De Ryck and Quéré
$h_{l,\mathrm{LLD}}$	Liquid coating thickness estimate after Landau, Levich, and Derjaguin
$h_{l,\mathrm{WT}}$	Liquid coating thickness estimate after White and Tallmadge
h_p	Thickness of tool platen
k_E	Einstein coefficient
l	Length, characteristic dimension
m	Mass
n	Power law exponent, number of layers
$\langle p \rangle_\Phi$	Pore-averaged fluid pressure
p_i	Inlet pressure
p_m	Pressure carried by matrix
p_o	Outlet pressure
p_v	Total internal void pressure
$p_{v,s}$	Total internal pressure of stable void
r_d	Circular dry area radius
r_f	(Reinforcing) fibre radius
r_m	Matrix fibre radius
t	Time
t_h	Holding time in press
$t_{h,\mathrm{sim}}$	Predicted holding time in press
t_r	Reptation time
t_t	Transfer time from oven to press
$\langle \mathbf{v} \rangle$	Superficial relative fluid velocity vector
$\mathbf{v}$	Velocity vector
$\overline{v_f}$	Mean fibre volume fraction
v_f	(Reinforcing) fibre volume fraction, glass volume fraction
$v_{f,c}$	Consolidated fibre volume fraction
$v_{f,i}$	Fibre volume fraction at position i
$v_{f,\mathrm{lim}}$	Fibre volume fraction limit value
$v_f^{0.7}$	Seventieth percentile of fibre volume fraction distribution
v_p	Polymer volume fraction

Dimensionless numbers

Ca	Capillary number

Ca_U	Capillary number of the kiss-roll at peripheral velocity U
Ca_V	Capillary number of the fibre at velocity V
To	Dimensionless film thickness
We	Weber number

Other symbols

$\mathcal{O}\left(x^i\right)$	Terms of order i of variable x
$\sigma\left(x\right)$	Standard deviation of distribution x
$\mathrm{A, B, C, D}$	Fitting parameters
A, B	Image segmentation areas
$F(x, y)$	Output image pixel
R^2	Coefficient of determination (goodness of fit)
c_i	Multiple regression fitting parameter
$f(x, y)$	Input image pixel
s	Standard deviation
x, y	Coordinates, pixel coordinates

Acronyms

ABS	Acrylonitrile butadiene styrene
APTES	3-aminopropyltriethoxy silane
BCF	(Hybrid) bicomponent fibre
BEV	Battery electric vehicle
BMW	“Bayerische Motoren Werke” (German car manufacturer)
CES	Cambridge Engineering Selector (materials selection software)
CMASLab	Laboratory of Composite Materials and Adaptive Structures
DIN	“Deutsches Institut für Normung” (German standardization organization)
DRQ	De Ryck and Quéré (coating model)
DSA	Drop shape analyser
EN	“Europäische Norm” (European standard)
ETH	“Eidgenössische Technische Hochschule” (Swiss Federal Institute of Technology)
FCEV	Fuel cell electric vehicle
FIT	Fibre impregnated thermoplastic
FOEN	Swiss Federal Office for the Environment

FRP	Fibre-reinforced plastic
GHG	Green house gases
HEV	Hybrid electric vehicle
HEV-p	HEV fueled by gasoline
HM	High modulus carbon fibre
HMS	High modulus and strength carbon fibre
HST	High strain and tenacity carbon fibre
HT	High tensile carbon fibre
ICEV	Internal combustion engine vehicle
ICEV-d	ICEV fueled by diesel
ICEV-g	ICEV fueled by compressed natural gas
ICEV-p	ICEV fueled by gasoline
ICEV-SNG	ICEV fueled by synthetic natural gas
IM	Intermediate modulus carbon fibre
ISO	International Organization for Standardization
LCP	Liquid crystal polymer
LLD	Landau, Levich, and Derjaguin (coating model)
MPP	Mesophase pitch
PA	Polyamide
PAN	Polyacrylonitrile
PC	Polycarbonate
PEA	Poly(ester-amide)
PEEK	Polyether ether ketone
PEI	Polyetherimide
PES	Polyethersulfone
PHEV	Plug-in HEV
PMMA	Poly(methyl methacrylate)
PP	Polypropylene
PS	Polystyrene
PTFE	Polytetrafluoroethylene
SCCER	Swiss Competence Center for Energy Research
SEM	Scanning electron microscopy
TGA	Thermogravimetric analysis
UHM	Ultra-high modulus carbon fibre
UHMWPE	Ultra-high-molecular-weight polyethylene
USA	United States of America
WLF	Williams-Landel-Ferry equation (viscosity model)
WT	White and Tallmadge (coating model)

FIGURES

1.1 Swiss green house gas emissions by sector 5
1.2 Contributions to green house gas emissions for the Swiss transportation sector 5
1.3 Sensitivity of climate change caused by passenger cars to their total mass 7
1.4 Ashby plot of specific strength versus specific stiffness for various materials 8

2.1 Existing hybrid thermoplastic composite preforms 15
2.2 Schematic of stamp forming 18

3.1 Schematic of bicomponent fibre preform 22
3.2 Theoretical unit cells of commingled yarn and bicomponent fibre preforms with random fibre distribution 23
3.3 Distributions of largest circular dry areas from randomly generated unit cells 23

5.1 Schematic illustration of the direct roving glass melt spinning process 43

6.1 Schematic of the proposed in-line dip-coating step 50
6.2 Measured characteristics of the polymer solution versus polymer concentration 51
6.3 Flow curves measured from solutions of poly(ester-amide) in trichloromethane 52
6.4 Dynamic viscosity of the polymer solution versus polymer concentration 53
6.5 Exemplary pendant drop image 54
6.6 Surface tension of the polymer solution versus polymer concentration 54
6.7 Predictions of the liquid coating thickness h_l normalized over the fibre radius r_f plotted against the fibre withdrawal velocity V 57

6.8 Predicted isolines of final fibre volume fraction plotted against the fibre velocity and the polymer concentration in the coating solution 59
6.9 Comparison of predicted fibre velocities in the dip-coating process with those in glass melt spinning 60
6.10 Schematic of the experimental setup for dip-coating of a glass monofilament with a polymer solution 61
6.11 Principle of the advanced transverse image analysis to determine the fibre volume fraction. 63
6.12 Scanning electron micrographs of solution dip-coated bicomponent fibres 66
6.13 Scanning electron micrographs of polished specimens of solution dip-coated bicomponent fibres 68
6.14 A representative scanning electron micrograph with its processed binary image; the total fibre widths $d_{t,i}$; and the distribution of fibre volume fractions $v_{f,i}$ 70
6.15 The distribution of fibre volume fractions $v_{f,i}$ derived from all images of the sample shown in Fig. 6.14 71
6.16 Probability density functions of measured final fibre volume fractions of solution dip-coated bicomponent fibres versus withdrawal velocity 72
6.17 Comparison of the mean measured fibre volume fractions with the predictions given by the analytical models 73

7.1 Qualitative comparison between the relative viscosity of a suspension as predicted by Einstein and as observed experimentally 78
7.2 Illustration of the setup used to dip-coat glass monofilaments with a nanofilled thermoplastic polymer melt. 82
7.3 Scanning electron micrographs of silica nanoparticles; and aggregates of silica nanoparticles after suspension and drop-casting 84
7.4 Distribution curves of aggregate sizes of drop-cast silica nanoparticles 85
7.5 Representative measured flow curves with their corresponding power law fits 86
7.6 Normalized consistency indices of nanofilled poly(ester-amide) melt versus particle concentration for samples prepared using different ratios of solvents and surfactant 87

7.7 Comparison of surface tension measurements for the pure polymer and a nanoparticle concentration of 0.23 vol% . . . 89
7.8 Micrographs of bare and dip-coated glass fibres 90
7.9 Measured coating thicknesses h versus withdrawal velocity V for the pure and sparsely nanofilled polymer compared to predictions 92
7.10 Comparison of withdrawal velocities required to yield a desired coating thickness for the pure and the sparsely nanofilled polymer melt 93

8.1 Schematic of the proposed in-line kiss-roll coating step . . . 98
8.2 Isometric illustration of the setup used to conduct the coating experiments of the parameter study 100
8.3 Scatter plot of the tested parameter combinations according to the face-centred central composite design 101
8.4 Schematic illustration of the material and process parameters involved in kiss-roll coating of fibres 104
8.5 Predicted liquid film thickness on the roll h plotted against the peripheral roll velocity U and compared with the mean diameter of the processed glass fibres 105
8.6 Scanning electron micrographs of kiss-roll coated fibres . . 106
8.7 Mean values $\overline{v_f}$ of the measured fibre volume fraction distributions $v_{f,i}$ of each coated sample plotted against the fibre velocity V for each parameter combination tested 108
8.8 Isosurfaces of fibre velocity required to yield a coating corresponding to a fibre volume fraction of 0.7 109
8.9 Isosurfaces of the yielded fibre volume fraction's sensitivity to changes in fibre velocity 110

9.1 The setup used for the coating trials in-line with the glass monofilament spinning machine 114
9.2 Measured fibre volume fractions v_f of the coated fibres plotted against the capillary number Ca_V at the corresponding fibre velocity V 117

10.1 Simulation results for the coalescence of molten polymer sheaths 125
10.2 Void stability map for a matrix with surface tension $\gamma_m = 27.6\,\mathrm{mN\,m^{-1}}$ 127

11.1 Cake of polycarbonate-clad glass monofilament as obtained from the spinning process 134
11.2 Bicomponent fibre preform inserted into rectangular mould and the same sample in consolidated state 136
11.3 Polished cross-section of a unidirectional glass/polycarbonate bicomponent fibre preform after subjection to a temperature of 300 °C without applying external pressure 137

12.1 Trimetric view of the tooling setup used in the stamp forming experiments 143
12.2 Representative scanning electron micrographs of polished specimens revealing the laminate quality of the stamp formed samples 144
12.3 Main effects plot of the measured void content Φ 146
12.4 Representative scanning electron micrographs of polished specimens revealing the laminate quality of the stamp formed cross-ply layups 148

TABLES

4.1 Mechanical properties of selected organic fibres 33
4.2 Mechanical properties of selected inorganic fibres 35

5.1 Typical parameters in industrial glass melt-spinning 45

7.1 Compositions of dispersing media tested to produce silica suspensions 83
7.2 Average consistency indices of the pure polymer K_l after processing with the different dispersing media mixtures . . 86
7.3 Mean coating thicknesses $\overline{h}$, corresponding standard deviations s and effect sizes d for the influence of nanofilling on the coating thickness in dip-coating 91
7.4 Summary of measured data for dip-coating of fibres from the pure and the sparsely nanofilled polymer melt 93

8.1 The parameter levels used for the experimental study . . . 102

10.1 Predictions of the required holding time t_h for different settings of initial temperature T_0 and press temperature T_p . . 131

12.1 Stamp-formed samples with their corresponding settings and measured results 145
12.2 Stamp-formed cross-ply samples with their corresponding settings and measured results 149

Part I

INTRODUCTION

1

ON THE IMPORTANCE OF LIGHTWEIGHTING AND EFFICIENT COMPOSITES PRODUCTION

> *Climate change is the Everest of all problems, the thorniest challenge facing humankind.*
>
> Lewis William Gordon Pugh

Today's global society carries the great responsibility of halting climate change along with its threats and possibly reversing some of the damage. Solving this challenge and thus scaling Mr. Pugh's proverbial Everest requires us to follow a number of principles which are of similar importance to mountaineering. We should practice sufficiency and only use what energy we need to live our lives, same as climbers only carry the equipment they need to fulfil their task. We should strive to use any energy as efficiently as we can and exploit new and innovative technologies which help us do so, same as alpinists prefer using the best equipment available to them. As mountaineers allow their bodies to rest and regain strength, we should move away from exhausting the world's fossil energy reserves and transition to renewable sources. Finally, as proper explorers clean up after themselves and leave no traces other than their actual footprints, humankind has to significantly reduce green house gas emissions and to widely adapt zero and negative emission technologies. It is clear that this pivotal challenge which Mr. Pugh emphasizes so distinctly has no single, grand solution, but that any developments – technical or otherwise – which carry potential to offset the effects of climate change are worth our attention.

The research presented in this thesis is motivated by the potential to offset emissions in the transport and mobility sector by increasing the widespread use of lightweight composite materials. The related industries experience the need to increase access to light, fibre-reinforced polymer composites for high-volume manufacturing settings. However, this has to be done with production costs and part performance (product value) in mind, which are the key incentives for adapting new technologies. This chapter gives a brief overview of the rationale behind the case for lightweighting strategies in the transport sector, followed by two chapters which outline the associated challenges.

Among other funding sources, the work leading to the presented findings was supported by the Swiss Competence Center for Energy Research (SCCER) Efficient Technologies and Systems for Mobility. The SCCER Mobility is a research program with the central aim to foster research and develop competencies in selected thematic areas where new solutions and products need to be developed to drastically reduce energy consumption and green house gas emissions in the Swiss transport sector. This work has been part of SCCER Mobility's capacity area A3, which investigates technologies and strategies to minimize non-propulsive energy demand of vehicles for improved efficiency. A core strategy focuses on expediting the adaptation of lightweight fibre-reinforced thermoplastic composites for high volume production, which is also the main focus of this work.

1.1 Green house gas emissions in Switzerland

To efficiently combat the sources of climate change, it is essential to look at the largest contributors. A widely accepted metric for this is the emission of green house gases (GHG). Fig. 1.1 shows the relative emissions of the largest contributors in Switzerland. The transport sector, being the largest overall contributor of all, made up almost a third of the total Swiss emissions in 2016. According to the data reported by the Swiss Federal Office for the Environment (FOEN), this distribution has largely remained the same for the last three decades.

Taking a closer look at the distribution of emitters within the trans-

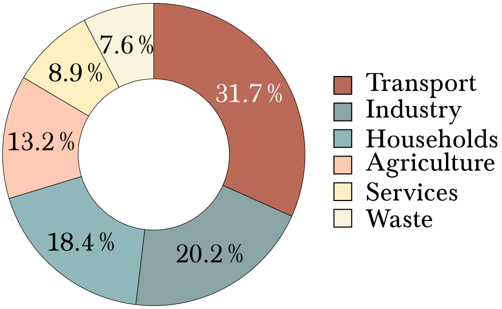

Figure 1.1:
Contributions to Swiss green house gas emissions in 2016 by sector.[1]

port sector, shown in Fig. 1.2, it is obvious that road based transport is by far the largest contributor, with road based mobility causing almost three quarters of annual Swiss GHG emissions. Note that the distribution shown in Fig. 1.2 neglects the contributions made by international aviation.[*] Nevertheless, both road transport and aviation are industries where lightweighting is already an important topic in technical product development.

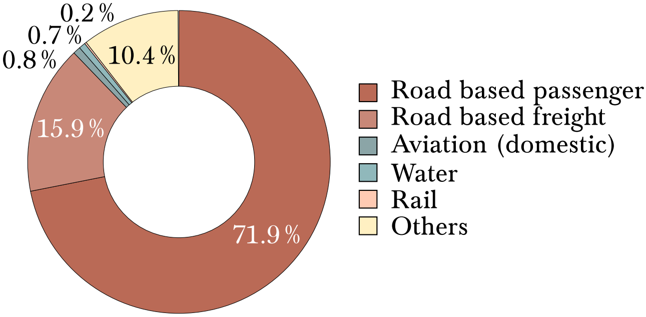

Figure 1.2:
Contributions to green house gas emissions for the Swiss transportation sector in 2016.[1]

---

[*] Quantitatively comparing the contributions to the Swiss GHG emissions made by international aviation is difficult, because it requires differentiation between the causes of each flight to determine a fair attribution of its emissions to the nations involved.

1.2 Efficiency through lightweighting

Let's see then how lightweighting can offset some of these emissions. During the use-phase of a vehicle, green house gas emissions are caused by moving said vehicle. Even in a lossless system it requires energy to set a standing body in motion or vice versa. Newton's second law of motion states that the change of momentum of a body is proportional to the impulse impressed on the body and that it happens along the straight line on which that impulse is impressed.[2] This is valid for constant-mass systems and at speeds which are not measurably influenced by relativistic effects. It can be expressed by the formula given in Eq. 1.1, where $\mathbf{F}$ denotes the force applied to the body, m is the body's mass, $\mathbf{v}$ is its velocity, $\mathbf{a}$ is its rate of acceleration, and t is time.

$$\mathbf{F} = \frac{\mathrm{d}\,(m \cdot \mathbf{v})}{\mathrm{d}t} = m \cdot \mathbf{a} \tag{1.1}$$

It is obvious then that reducing the mass m of a moving body proportionally reduces the force $\mathbf{F}$ which is required to maintain a constant rate of acceleration $\mathbf{a}$, making the system more energy-efficient for the purpose of maintaining that acceleration. In the real case of moving vehicles, additional energy is required to overcome losses caused by rolling resistance, aerodynamic drag, and friction and energy conversion inefficiencies in the drivetrain.

Even in the age of electrified drivetrains, which can recuperate energy during braking, lightweighting remains an important aspect in the design of energy efficient vehicles. This is evidenced by the data shown in Fig. 1.3, which plots the climate change potential per vehicle kilometre against the total vehicle mass for different drivetrain technologies. It is clear that while hybrid and fully electric power trains are causing a lower footprint during their use than internal combustion engines do, the relative sensitivity of the caused climate change to the weight of the vehicle is roughly the same as for the purely combustion-based drivetrains. In addition, lighter cars may be designed to carry smaller batteries, which may already reduce their environmental footprint before leaving the factory.

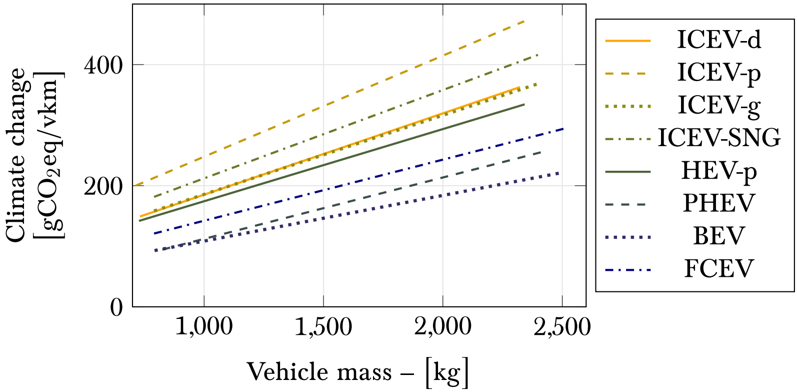

Figure 1.3: Sensitivity of climate change caused by passenger cars to their total mass, as modelled by Cox.[3] The lines show the linear regressions of the data for internal combustion engine vehicles (ICEV) fueled by diesel (-d), gasoline (-p), compressed natural gas (-g), and synthetic natural gas (-SNG), as well as for hybrid electric vehicles (HEV), plug-in hybrid electric vehicles (PHEV), battery electric vehicles (BEV), and fuel cell electric vehicles (FCEV).

1.3 The role of composites in transport

Lightweighting efforts in the transport sector play a major role in the industry of fibre-reinforced polymer composites. This is reflected through the share of this market within the global demand of composite materials:* in 2018, the entire transport sector was responsible for an estimated 36 % of the glass fibre-reinforced plastics production in Europe; the space and aerospace industry (including defense) was responsible for 36 % by weight of the global carbon-fibre composites production; and the automotive sector globally demanded 24 % by weight of produced carbon-fibre composites.[5] But why are these materials so popular for use in lightweight structures and what hinders their widespread adaptation if they are more energy-efficient than conventional metallic structures?

---

*The majority of fibre-reinforced polymers not processed in the transport sector are used for construction and industry infrastructure, sporting and consumer goods, and wind energy.[4]

Compared to metals, fibre-reinforced plastics offer significant benefits in the design of lightweight structures just because of their specific mechanical properties. In properly designed laminates, the fibres are oriented in the direction in which stress is transferred. Such laminates outperform other materials which are traditionally used in the aerospace and automotive industries both in specific strength and stiffness, as is shown in Fig. 1.4. Carbon-fibre reinforced high performance plastics can even surpass steel and light metals when used in a quasi-isotropic layup. Because of this, carbon-fibre has become the load-carrying material of choice for many space and aviation applications, sports cars, and high-performance sporting equipment.

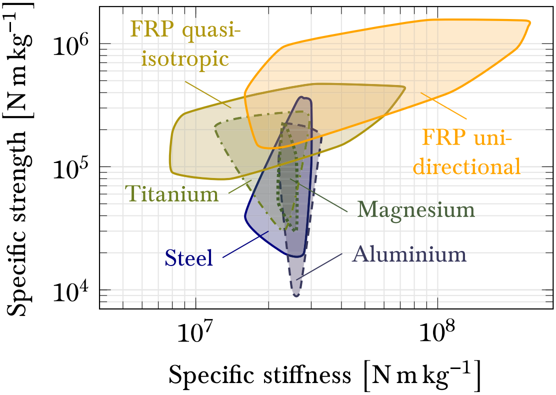

Figure 1.4: Ashby plot of specific strength versus specific stiffness for various metallic alloys and fibre-reinforced plastics (FRP) in both unidirectional and quasi-isotropic layup. Data taken from CES EduPack software.

In spite of the high share the transport sector holds within the composites market, these material solutions have not yet found their way into the mainstream production of load-carrying automotive components. Let's illustrate this with an example: to date, the only "mass-produced" passenger car to have employed continuous-fibre reinforced material in a large percentage of the total body structure has been the BMW i3-series electric urban car. According to the BMW Group, this was done to offset the added weight of the battery-electric drivetrain. Almost half the weight of the i3's body-in-white stems from fibre reinforced plastics, having reduced the overall share of metals to only 26.5 %.[6] Between its launch in 2013 and the end of 2018, an estimated total of 133 397 units have been sold worldwide, averaging 26 384 units per year since 2014.[7–12] The retail prices at its launch started at $42 275 in the United States of America, with slightly higher pricing in Europe.[13–15] Since the introduction of the i series cars, BMW has adapted the use of carbon-fibre for structural parts to its renewed 7 series sedan in 2015. However, its body-in-white only contains sixteen components made from fibre-reinforced plastics, totaling 13 kg and contributing only 3 % by weight to the entire structure.[16] Even this seemingly small percentage requires the plant to manufacture 4000 composite parts per day[16] for the production of the 7 series, of which 56 037 units and 64 311 units have been delivered in 2018 and 2017, respectively.[17] At its introduction in 2015, different versions of the 7 series were advertised for retail prices starting at $82 295.[18]

Now consider that the threshold for mass production in the automotive industry is generally estimated at 100 000 units per year and that the average selling price for a new car in 2012 was just above $30 000.[19] This illustrates that current composite materials and their associated manufacturing technologies are still struggling to penetrate high-volume low-cost markets. This is mostly due to limitations in cost-efficiency and material throughput at some point in the value chain of continuous-fibre reinforced plastics manufacturing. Therefore, cheaper and more efficient material conversion processes are required to expedite the adaptation of this lightweight material technology in automotive structures and other high volume markets.

2

STATE OF THE ART

To understand why current material conversion processes cannot supply sufficient parts to high volume markets like the automotive sector at affordable costs, a few basic aspects of composites manufacturing are outlined in this chapter. They are meant to provide some insight into key performance indicators for high volume production in general and into the benefits and challenges associated with existing solutions.

2.1 Advantages of thermoplastic matrix polymers

The first point of discussion is the categorical choice of matrix material. The matrix in a composite is the constituent filling the space between the reinforcing material. In the case of continuous-fibre reinforced polymers, it is the polymer. Its primary function within the structure is to keep the reinforcing fibres in place and to carry loads which act transversely to the fibre direction. Without the matrix, the fibres cannot maintain the shape of the structure they make up. Without the fibres, the matrix is not stiff or strong enough to withstand the applied load without excessive deformation or structural failure. With regards to the choice of polymer for a given application, possible considerations are its overall mechanical performance, both static and over time, its interaction with the chosen reinforcing fibre, its resistance against moisture, radiation, and chemical attack, its flammability, or its treatment once the composite reaches its end of life. Another performance indicator which becomes of major importance when addressing high volume manufacturing is its processing behaviour. In other words, how fast can the material be processed and how much will it cost?

While the production costs of the polymer itself are highly dependent on its exact formulation, the potential for cost-efficiency and throughput during its conversion into a composite can be discussed categorically. Polymers are divided into two classes: thermoset and thermoplastic polymers. Their characteristics carry some major implications regarding the choice of manufacturing technology. Polymers are made up of long, chain-like macromolecules which in turn are made up of repetitive patterns of elements. The smallest repeat unit is also called "monomer residue", since the synthesis of a macromolecule includes a chemical reaction in which monomers (molecules containing only one repeat unit) are assembled to form the long chain via covalent bonds. These monomer materials are commonly in the liquid state and possess a very low viscosity.

In thermoset polymers, the polymerization reaction also yields cross-links, i.e. shorter chains which branch out from each molecular array and covalently bond them with each other. To be more precise, common thermoset materials, especially epoxy-based formulations, are often pre-polymerized to an intermediate state which is still liquid or at least malleable. Both this pre-polymer and the monomer compound are referred to as "resin". Upon the addition of a hardener, cross-linking and chain extension occurs until the hardener has fully reacted with the resin, ideally resulting in a single macromolecule. This polymerized network is relatively strong, because failure can only be induced by breaking covalent bonds. Depending on its cross-linking density, it is often also relatively stiff, because the orientation of the chains is locked into place by the cross-links. Thermosetting polymers, once fully cured, are solid and cannot be liquefied without destroying the integrity of the molecular network. Therefore, using thermosetting materials as the matrix in composites requires the reinforcement and matrix to be combined prior to curing. In one form or another, this is always done by infusing dry fibre bundles with the liquid resin and hardener mixture, either to produce an intermediate, pre-impregnated preform ("prepreg") or during the fabrication of the final component itself. In the case of prepregs, the curing reaction is however slowed down by freezing the material until it is used. During the production of a part, the curing reaction is accelerated by exposing the material to higher temperatures. However, chemical reactions always take time, which means that it is difficult to achieve sufficiently low cycle times for high volume production when using thermosetting materials. Producers of such compounds have addressed this challenge with the development of so-called “snap-cure” resins, which provide a compromise between fast curing, low viscosity, and their final mechanical properties. In reference to the application example outlined in chapter 1.3, BMW has successfully adopted such resins for the production of their components for the i series and the 7 series. Still, it remains questionable whether this technology can be scaled towards even lower cycle times and higher throughput, or whether part manufacturers like BMW have already approached the limit.

As an alternative class of matrix material, thermoplastic polymers consist of many molecular chains which are entangled with each other, but form no closed network through cross-links. Their mechanical stiffness and strength are mostly a result of intermolecular forces and of their entanglement. If polymer chains are distributed in a random, arbitrary way, the microstructure of this material is also referred to as “glassy” or “amorphous” and is solid. When exposing such a polymer to increasing temperatures, the Brownian motion of the macromolecules eventually overcomes the intermolecular forces and the chains begin to slip past each other if stress is applied. The material transitions from a solid to a viscous melt. The reverse change is commonly referred to as the glass transition. Polymers in which sections of the macromolecules form ordered arrangements are referred to as “semi-crystalline”. These crystalline regions carry stronger interactions between the molecules and therefore more energy is required to allow these chains to move freely. Semi-crystalline polymers soften somewhat above the glass transition temperature, but still maintain significant stiffness and strength. Only at a higher temperature, the crystalline regions loose their mechanical integrity and the material melts into a liquid. Vice versa, cooling the melt at a sufficiently low rate causes crystalline regions to form and grow before the remaining areas transition into the glassy state. This crystallization temperature is highly dependent on the cooling rate and many polymers which tend be semi-crystalline can be “quenched” to lock the macromolecules in place in a purely amorphous arrangement.

In thermoplastic polymers used for engineering applications, the temperatures at which the state changes from solid to liquid or vice versa occur are sufficiently lower than the onset temperature of degradation, at which the molecules start to decompose. This allows thermoplastic materials to be processed in many cycles of melting and solidification simply by heating and cooling, respectively. Process engineers can profit from this behaviour to design manufacturing chains where multiple steps are parallelized to reduce cycle time and overall production cost. Examples for this are pre- and post-forming steps to realize separate features of a structure or simply the separation of heating (melting) and cooling (solidification) steps, meaning that while one part is being solidified, the material for the next part is already being melted. Furthermore, it allows parts made from thermoplastic materials to be welded. Weld constructions are often more structurally efficient than, say, bolted or even adhesively bonded designs, because they avoid excessive stress concentrations. Finally, the fact that thermoplastic structures may be re-processed at their end of life opens up a variety of possibilities for recycling, ranging from simple repair and re-use to a fully circular material economy.

For application as a composite matrix, thermoplastic polymers are however not without drawbacks. The viscosities of thermoplastic melts are relatively high, namely on the order of 10^1 Pa s to 10^5 Pa s.[20] This is owed to the large amount of molecular interactions still present in the liquid state, simply because of the size of these molecules. A polymer's melt viscosity is therefore highly dependent on its molecular weight, as are strength, modulus, and resistance to creep. This means that combining a high molecular weight polymer providing excellent mechanical properties with reinforcing fibres to form a composite is not trivial, because all existing value chains rely on the impregnation of dry bundles of fibres with the matrix material in liquid form. This fluid flow through a porous medium is commonly modelled on the basis of Darcy's law,[21,22] given in Eq. 2.1, where $\langle \mathbf{v} \rangle$ is the superficial relative fluid velocity with respect to the porous medium, $\mathbf{K}$ is the permeability tensor of the porous medium, η is the dynamic viscosity of the fluid, and $\nabla \left\langle p \right\rangle_\Phi$ is the gradient of the pore-averaged fluid pressure driving the flow.

$$\langle \mathbf{v} \rangle = -\frac{\mathbf{K}}{\eta} \nabla \left\langle p \right\rangle_\Phi \qquad (2.1)$$

Eq. 2.1 shows that high viscosities result in low fluid velocities and therefore in long impregnation times, which are impractical for high rate production. Various preforming technologies exist which try to overcome this challenge by reducing the distances the melt needs to flow to achieve full impregnation of the fibre bed. The following section provides a brief overview of these products and their advantages and disadvantages in the context of high volume manufacturing.

2.2 Thermoplastic matrix preforms

In commercially available thermoplastic composite preforms, the total impregnation length is reduced by increasing the degree of mingling between reinforcement and matrix prior to part production. Currently, mingling in such preforms is found on the level of the laminate down to the level of the yarn as schematized in Fig. 2.1, but may occur on any of the hierarchical tiers found in fibre-reinforced composite materials. The level and quality of mingling in existing arrangements greatly influence the flow lengths, cycle times, achievable part complexity, raw material costs, and suitable manufacturing routes.

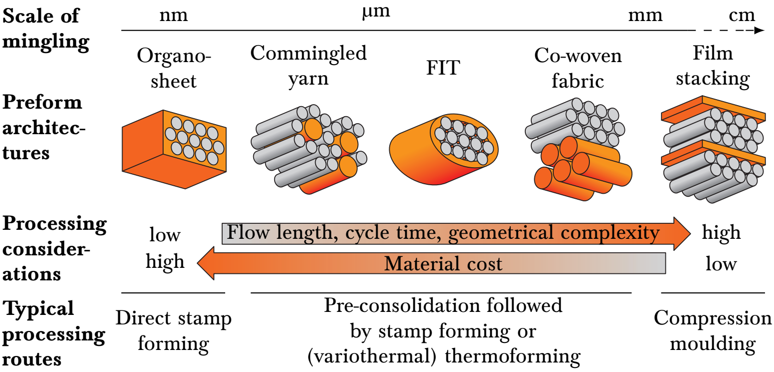
Scale of mingling
nm
µm
mm
cm
Preform architectures
Organo-sheet
Commingled yarn
FIT
Co-woven fabric
Film stacking
Processing considerations
low
high
Flow length, cycle time, geometrical complexity
high
low
Material cost
Typical processing routes
Direct stamp forming
Pre-consolidation followed by stamp forming or (variothermal) thermoforming
Compression moulding

Figure 2.1: Schematics of various existing hybrid preforms for the manufacture of thermoplastic composites.[23]

A classic method of processing a hybrid intermediate product is the alternated stacking of dry textiles and polymer films.[24] Since this does not generate any additional effort compared to the lamination of the desired layup, which is required anyway, this technique offers enormous freedom in the choice of material and the design of the layup itself.

However, the constituents are only mixed at the level of the laminate, whereby the flow length for complete impregnation is only reduced to the thickness of the individual layers. A complete consolidation of such layered laminates is therefore only possible in variothermal compression moulding with sufficient pressure and a significant holding time above the melting temperature of the polymer.

A slight improvement in cost efficiency across the entire process chain can be achieved by using co-woven fabrics.[25] These hybrid textiles are made from two types of yarns, one of which consists of thermoplastic polymer fibres, which impregnate the bundles of reinforcing fibres as the material is consolidated. Depending on the exact design of the fabric architecture, this can somewhat reduce the cycle times in processing compared to film stacking, but the pressing of such hybrid fabrics often results in comparatively inhomogeneous laminates with uneven fibre distribution.

Much more intimate mixing of the constituents is achieved with the production of powder-impregnated yarns.[26] With the aid of suitable spreading methods, attempts were made to impregnate the yarn with the matrix polymer in powder form and thus distribute the material ideally before consolidation. However, it has been proven to be extremely difficult to include a sufficient amount of powder in the yarn without this being lost during further processing into flat semi-finished products (woven textiles or non-crimp fabrics). Fibre impregnated thermoplastics (FITs) addressed this issue by means of a polymer sheath enclosing the yarn, which is made from the same material as the powder.[27] However, problems with the tear resistance of this sheath, especially during weaving, have hindered the extensive adaptation of this technology.

With the use of commingled yarns, an improvement has been found over the hybrid yarn concept of FITs, which is enjoying increasing popularity.[28] The underlying principle is rather simple: Two different yarns, one consisting of the matrix polymer in fiber form, are blended to become a single yarn carrying both constituents in fiber form. This material distribution reduces the flow distances that the polymer melt has to overcome during the consolidation of the laminate to the size of fibre bundles that are smaller than the entire yarn. The production of flat preforms from such commingled yarns is made slightly more difficult by the fact that their production often results in a certain texturing of the yarn. Texturing in this context means that the fibres are not ideally oriented along the yarn direction everywhere, but have a wavy shape and constantly change their position in the cross-section, which reduces the stiffness and strength of the yarn. Still, it could be shown that with sufficient homogeneous blending of the two fibre types, such materials can be processed comparatively efficiently into laminates.[29]

The part production method with the lowest cycle times is however the direct stamp forming of consolidated blanks, also called “organosheets”. These materials are basically already fully consolidated flat laminates, which are moulded into the desired shape in a press. A significant issue with organosheets is the way they are produced. In theory, such blanks can be compression moulded using any of the aforementioned materials as a precursor. In practice, most organosheets are manufactured using a double-belt press, basically a continuous version of the film stacking method. But because this method still relies on the through-thickness impregnation of dry fibre beds with the high viscosity thermoplastic melt, its throughput is relatively low and makes it energy- and cost-intensive. In addition, the pre-consolidated nature of organosheets limits their drapeability, i.e. their ability to conform to complex geometries during forming, especially in thick laminates. In spite of these drawbacks, the conversion of consolidated blanks into a structural component is very effective, as is outlined in the following section.

2.3 Stamp forming

Organosheets are commonly processed into parts using stamp forming. This process, schematically represented in Fig. 2.2, has established itself as the benchmark for high rate production of thermoplastic composites, especially in the automotive market. Ahead of the actual forming step, the consolidated blank is heated above melt temperature outside of the press. This is usually done in a infrared radiation oven, due to its quick heating action and high energy-efficiency. Upon reaching the desired temperature, the material is transferred to the press carrying the mould tool. This tool is kept at a specific temperature below the solidus point of the matrix polymer. When closing the press, the material is simultaneously formed into the desired shape and cooled by the conduction of heat to the larger thermal mass of the mould. Once the entire laminate is solidified, the press is opened and the finished part is demoulded and possibly transferred to a trimming step. The preheating temperature outside the press and the temperature of the mould

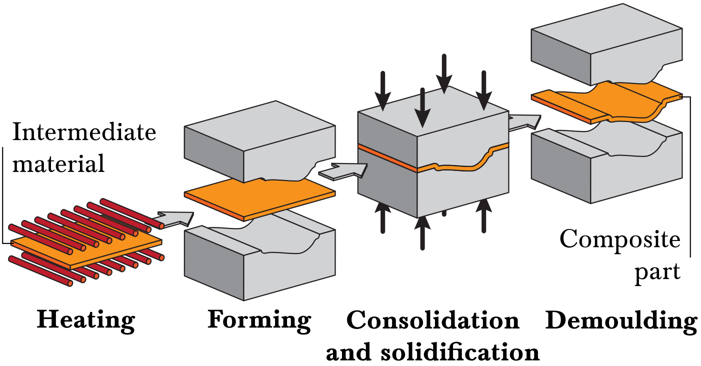

Figure 2.2: Schematic of the distinct processing steps during stamp forming.

tool are chosen such that the heat transfer during cooling is optimized for speed without inducing unwanted thermal stress in the laminate. This process yields the lowest cycle times known in composite part production because the heating and cooling steps are parallelized – i.e. a new blank can already be heated while the former part still resides in the press – and because the mould tool is kept at a constant temperature. Most other thermoplastic press processes, as well as thermoset curing processes, require a thermal cycling of the mould, which takes more time due to the usually much larger thermal inertia of the mould, in comparison to the manufactured part. So, if rapid stamp forming is so effective, why is it not used on a broader scale?

Given the limited selection of commercially available preform architectures, manufacturers must choose between the low cycle times but high material costs of organosheets in stamp forming and the better drapeability but long processing cycles of unconsolidated hybrids, e.g. commingled yarns, in thermoforming. The development of a material architecture which combines the fast processing of fully impregnated products with the flexibility of unconsolidated preforms would render thermoplastic composites significantly more attractive to high volume production markets.

3

HYBRID BICOMPONENT FIBRES

This thesis investigates hybrid bicomponent fibres – which consist of continuous reinforcement fibres individually sheathed in a thermoplastic polymer – as a new class of preform materials for thermoplastic composites. By reducing the scale of mingling between the reinforcement and matrix materials to the level of the fibre, as shown in Fig. 3.1, a full wet-out of the fibres is ensured while the unconsolidated nature of the material allows the fibres to shift and deform with respect to each other to ensure high drapeability.[30] This combination of ideally perfectly impregnated reinforcing fibres and high conformability cannot be found in currently available state-of-the-art intermediate materials.

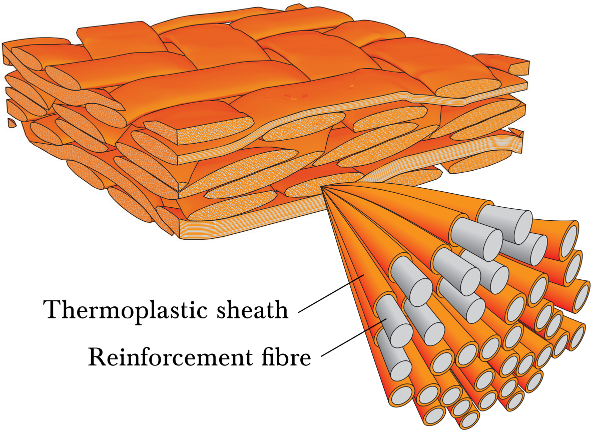

Figure 3.1: Schematic of a cut preform stack of textiles composed of bicomponent fibres.

3.1 On the idea of a perfect preform

How does a preform comprised of bicomponent fibres (BCF) fare in comparison with state of the art hybrid intermediate materials? This section addresses this question based on the idea of reduced flow lengths during the consolidation phase and uses commingled yarns as a benchmark. A simple geometrical study which models randomly distributed fibres in unconsolidated unidirectional preforms demonstrates the advantages of the hybrid bicomponent fibre preform architecture for consolidation. The models, examples of which are shown in Fig. 3.2, compare unit cells of a set of corresponding commingled yarns of different qualities with a unit cell of hybrid bicomponent fibres and show that the potential for dry areas is significantly reduced in the bicomponent fibre configuration. It should be noted that these representations of commingled yarns provide an optimistic mingling quality; commercially available products generally do not show such a high degree of mingling of the polymer filaments.[29]

Fig. 3.3 plots the radii of the largest measured dry areas r_d, normalized over the radius of the reinforcing fibre r_f, for all simulated unit cells. The distributions for each type of unit cell represent the results of a total

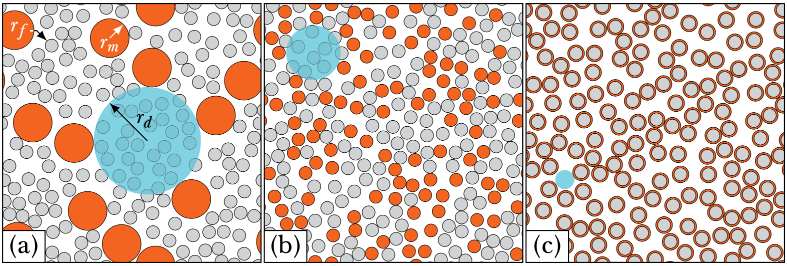

Figure 3.2: Unit cells of randomly distributed commingled yarn constituents with a relative matrix fibre diameter r_m/r_f of 3 (a) and 1 (b); and randomly distributed bicomponent fibres (c). Reinforcement fibres, thermoplastic fibres, and the largest circular dry area are depicted by grey, orange, and cyan, respectively. All unit cells are quadratic and have a normalized side length of $l/r_f = 20$, an unconsolidated void content Φ_0 of 50 % and a consolidated fibre volume fraction $v_{f,c}$ of 60 %.[23]

of 1000 randomly generated fibre distributions. The box plots in Fig. 3.3 show the second and third quartiles, divided by the median, and the whiskers show the minimum and maximum values of the distributions.

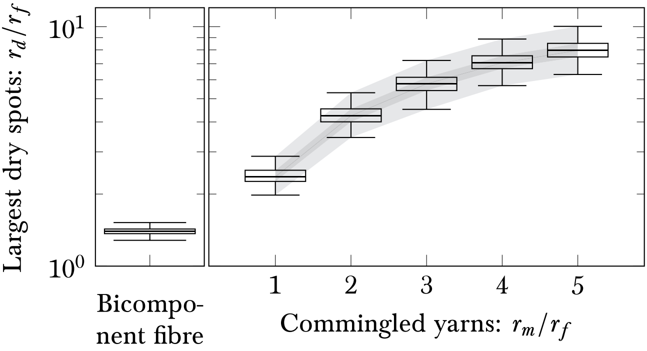

Figure 3.3: Distributions of largest circular dry areas from 1000 randomly generated unit cells for the case of bicomponent fibres and commingled yarns with variable relative matrix fibre diameter r_m/r_f. Examples of these unit cells are shown in Fig. 3.2.

The largest dry areas calculated from the hybrid bicomponent fibre models were found to be 47 % smaller in diameter than those calculated for even the most intimately mingled commingled yarns ($r_m/r_f = 1$), and 79 % smaller than those found in more realistic[*] representations of commingled yarns ($r_m/r_f = 3$), which contain bulkier polymer fibres.

The dry areas in the commingled yarn preforms contain bundles of reinforcement fibres which need to be filled with matrix during consolidation. The achievable cycle time is therefore highly dependent on the size of the largest dry area found in the processed preform. In contrast, precursor materials made from bicomponent fibres do not only show significantly smaller dry spots, but these are only air gaps which close under pressure. This highlights the fact that the use of hybrid bicomponent fibres avoids any impregnation flows altogether, meaning that Darcy's law does not apply; their consolidation merely requires a coalescence of the molten thermoplastic sheaths, similar to sintering, and an extraction or collapsing of remaining voids. On the basis of the argument that Darcian impregnation flows are the main limitation for high rate composite production using thermoplastics, bicomponent fibres can therefore be seen as a potential technological breakthrough in the reduction of cycle times over the entire value chain. Of course, this requires that this novel intermediate material itself can be manufactured in a fast and cost-efficient way which does not offset the advantage gained through the avoidance of an impregnation step.

3.2 Hypotheses on the processing of hybrid bicomponent fibres

The simple concept of reducing the scale of mingling in hybrid thermoplastic composite preforms down to the single fibres carries some implications with regards to their processing behaviour. Part of the research presented in this thesis aims to characterize the performance of bicomponent fibre preforms in high volume production schemes with a particular focus on rapid stamp forming. This includes proving or disproving each of the following hypotheses:

Hypothesis 1 *Preforms made from hybrid bicomponent fibres can be stamp formed with cycle times similar to those of pre-consolidated blanks.*

---

[*] Previous studies report values for r_m/r_f ranging from 2.9 to 3.5.[31,32]

With the obsoletion of impregnation flows, preforms based on bicomponent fibres have the potential to be processed and formed on time scales similar to those of pre-consolidated intermediate materials, whose processing bottle-necks are found not in the consolidation step, but rather in the heating and cooling stages. Applied pressure, though not necessary for impregnation, would still be needed for the removal of voids and to impart shape.

Hypothesis 2 *The void content of laminates stamp formed from hybrid bicomponent fibre preforms is greatly influenced by sintering mechanisms and the removal and/or collapse of air pockets.*

The effects of polymer sintering have already been reported to be significant consolidation mechanisms in commingled yarns.[33] In hybrid bicomponent fibre-based preforms, homogeneous sintering and welding mechanisms, which are governed by the interplay of surface energies and the formation of autohesion, are expected to dominate the process behaviour during consolidation. Simultaneously, the remaining air between the fibres is pushed out of the preform at the beginning of the consolidation process, followed by a transition to entrapment of air and a collapse of these remaining pockets. Void collapse has already been shown to be of importance in the design of stamp forming processes using pre-consolidated materials, due to de-consolidation during the heating phase.[34] It is expected that void entrapment and collapse is of even greater importance in the processing of bicomponent fibres, due to the highly increased presence of air everywhere in the preform.

3.3 State of the art in bicomponent fibres

Bicomponent fibres made up of different polymer materials are already well known in the textile industry and are manufactured by co-extrusion or spinning from the same spinneret.[35–40] Like-wise, processes for fabricating bicomponent fibres from two different types of glass have also been established.[41–43] However, the successful co-extrusion of hybrid polymer and glass bicomponent fibres is made unlikely by the large differences in melt temperatures between polymer and glass materials.

Still, the idea of reinforcing fibres individually clad with thermoplastic sheaths was interesting enough for Reifenhäuser GmbH & Co. (Germany) to apply for a patent in 2014, describing a method and semi-finished product for producing a fibre-reinforced moulded part.[30] This patent application describes the same concepts investigated here but does not offer any description on how such fibres are to be produced. While the concept of sheath-core bicomponent fibres as thermoplastic materials may appear simple enough, the technical understanding needed to fabricate these materials is not trivial. Some of the difficulties in producing bicomponent fibres with glass cores and thermoplastic sheaths are described in a 1997 patent by Owens Corning (USA). They invented a co-spinning technique for this purpose using a rotary process.[44] However, high degrees of warp were observed due to the difference in the coefficients of thermal expansion of glass and polymer. Fibres for advanced structural composite applications should, however, not be warped to maintain their high stiffness and strength in the consolidated, anisotropic laminate.

With no commercial product available and state of the art technology for the production of bicomponent fibres either relying on the pairing of similar materials or being subject to high degrees of warp, a novel method for manufacturing hybrid bicomponent fibres needed to be found to enable the experimental characterization of this novel type of thermoplastic composite preform. The remainder of this thesis focuses on the fabrication of hybrid bicomponent fibres (part II) and their processing performance in stamp forming (part III), reports on the results obtained from theoretical and experimental studies, and concludes with comments on how the state of the art in hybrid bicomponent fibre technology has been advanced through this work and what still remains to be done (part IV).

Part II

FABRICATION

4

MATERIAL AND PROCESS SELECTION

Selecting a suitable method to manufacture bicomponent fibres (BCF) for the purposes outlined in Part I starts with the requirements on the material itself. Developing a high-throughput and accessible manufacturing technology for high-performance lightweight structures requires the material to be strong, yet light, and thus the focus here lies on continuous and aligned fibre reinforcement. This chapter gives an overview of available materials and how they are formed into fibres, and moves on to comment on the suitability of different sheathing strategies for the fabrication of thermoplastic BCF. The successive chapters explain the chosen methods in more detail and report on experimental investigations into their suitability for BCF production, culminating in the realization of a pilot plant which continually produces a hybrid bicomponent monofilament (a single BCF).

4.1 Reinforcing fibre materials

The main parameters defining the mechanical performance which can be achieved by thermoplastic composite materials are the fibre strength and stiffness, the fibre content, the strength of the fibre-matrix interface, and the properties of the polymer matrix. The latter two depend on the choice of matrix material, which is often specific to the application for which the structure is built. A more general categorization can be made for the materials used to form reinforcing fibres, which are classified into organic and inorganic materials. The following sections provide a general overview of materials and methods used to form reinforcing fibres.

4.1.1 Organic fibres

Organic fibres can be further sub-categorized into natural and synthetic fibres. Natural fibres for composite applications are sourced from plant stems (e.g. flax) or leaves (e.g. sisal).[45] They own the second-largest share of the global composite fibre market in terms of volume, having contributed 9.5 % to 11.0 % from 2000 to 2018.[4] Other plants which are frequently used are jute and hemp. However, all of these fibres are extracted from the plant in the form of fibrous tissue or fibre bundles, which makes sheathing of the single fibrils for the creation of BCF difficult, if not impossible.

Synthetic organic fibres used as reinforcements for structural composites are exclusively made from polymers. Their manufacture generally starts with the preparation of a spinning solution followed by a fibre formation step which involves the precipitation of the polymer from the solvent, a drawing step where the filaments are stretched to a finer diameter, and concludes with the application of a surface finish and take-up on a bobbin.[45] Depending on the type of polymer, spinning and precipitation are often performed in methods dubbed “wet spinning” or “air gap spinning”, both of which involve the drawing of the fibres through a precipitation bath where the material solidifies by means of solvent exchange and precipitation. Some polymers can be “dry spun”, meaning that precipitation happens by simply spinning into a stream of hot air. In theory, numerous polymers can also be spun directly from melt, without previous addition of solvents. However in practice, this method is less used to produce reinforcing fibres.

Polymeric fibres are stretched following their formation to induce orientation of the macromolecules along the fibre direction, thereby rendering the fibre anisotropic for the sake of increasing Young’s modulus and strength in fibre direction. Prominent materials used in structural composites are aromatic polyamides (aramids), in particular para-aramid (Kevlar®) and sometimes meta-aramid (Nomex®), ultra-high-molecular-weight polyethylene (UHMWPE) (e.g. Dyneema® or Spectra®), or more ductile materials like polyamides (PA), polyethersulfone (PES), or polypropylene (PP). Newer developments involve fibres made from meltable liquid crystal polymers (LCP), most notably those made from aromatic polyester.[45]

The methods used to form polymeric fibres all involve a spinneret which contains separate nozzles, one for each fibre being spun. This means that a sheathing process could be implemented between the spinneret and the point where the single filaments are bundled. However, the latter point is generally placed before the drawing (stretching) step. This would mean that the sheath of the hypothetical BCF would be stretched as well, which is not a problem in itself, but the stresses applied to the fibres during this step might exceed the strength of the sheath or its interface. The same issue is present when conceiving a method of fabricating BCF based on co-extrusion, as it is already done for the creation of nanofibres or artificial turf.[35–37] However, neither application poses the same requirements on stiffness and strength as advanced structural composites. Table 4.1 provides the basic mechanical properties for a selection of organic fibres commonly used as structural reinforcements. It should be noted that the indicated levels of stiffness and strength of polymeric fibres are achieved only after the drawing step.

Table 4.1: Mechanical properties of selected organic fibres used in structural composites.[45–47]

	Density [g cm^{-3}]	Young's modulus [GPa]	Tensile strength [MPa]	Elongation at break [%]
		Natural fibres		
Flax	1.50	80…100	1100	2.0…3.0
Sisal	1.30…1.45	9.4…38	568…850	2.2
		Polymeric fibres		
Para-aramid	1.39…1.47	58…186	2760…3620	1.9…4.4
UHMWPE	0.97	87…170	2800…3100	2.7…3.5
PA	1.13…1.16	4.0…8.3	780…930	14.0…22.0
PES	1.10…1.39	10…15	820…1200	8.0…22.0
PP	0.90	0.5…5.0	455…670	8.0…10.0
LCP	1.41	100	2700	3.0

4.1.2 Inorganic fibres

Inorganic materials present an even larger selection of material types to be used as fibre reinforcements in polymer composites. They can offer various advantages over organic fibres and over high-performance polymeric fibres in particular: glass fibres are cheaper to produce and are made from abundantly available raw materials, be it naturally occurring sands or recycled scraps and waste glass; carbon fibres present the highest performance in terms of both absolute and specific stiffness and strength; and metal, ceramic, and other mineral fibres find applications with exploit their special properties or functions. Table 4.2 lists the mechanical properties of a selection of inorganic fibres used to reinforce structural composites. The following paragraphs give an overview of the characteristics and applications of each material class and summarize corresponding methods for fibre formation.

Glass fibres traditionally own the largest share of the composites market, both by volume and revenue: between 2000 and 2018, glass fibres made up 87.7 % to 90.2 % of the total volume of fibres on the market and shared 68 % of the value of fibres sold in 2018.[4] They consist of a glassy mixture of mineral oxides, with silica as the main compound, and are internally isotropic.[45,57] Glass fibres are attractive because of their high tensile strength combined with high chemical stability and low production cost. They are formed by melt spinning: the material is heated to a temperature at which its melt exhibits a low enough viscosity to flow through a spinning nozzle, while maintaining a high enough melt stability to be drawn to a thin filament. Large producers link the spinning stage directly with the preparation of the glass compound from the raw minerals and keep the entire plant running continuously until major refurbishments are required.[57] Smaller plants simply re-heat glass pellets, spherules, or powders. Straight fibres used for directional reinforcements are spun in the "direct roving process", which is presented in more detail in chapter 5. In contrast to the methods used to form polymeric fibres, melt spun glass fibres are not drawn to a thinner diameter after solidification and the streams of molten glass are not drawn through a bath. This means that melt spinning provides easy access to the single filaments for the implementation of a sheathing step between fibre formation and further processing, enabling a possible path for the realization of hybrid BCF production.

Carbon fibres are the chosen reinforcements for high-performance

Table 4.2: Mechanical properties of selected inorganic fibres used in structural composites.[45–56]

	Density [g cm^{-3}]	Young's modulus [GPa]	Tensile strength [MPa]	Elongation at break [%]
Glass fibres				
E-glass	2.52…2.60	72…77	3400…3700	3.3…4.8
AR-glass	2.70	76	2000	2.6
R-glass	2.50…2.53	83…87	4400…4750	4.1…5.4
S-glass	2.45…2.55	75…88	4300…4900	4.2…5.4
M-glass	2.89	87…115	4750…4900	4.0
Carbon fibres				
HT	1.74…1.80	200…250	2700…3750	1.20…1.60
IM	1.73…1.80	250…400	3400…5900	1.10…1.93
HM	1.76…1.96	300…500	1750…3200	0.35…1.00
HST	1.78…1.83	230…270	3900…7000	1.70…2.40
PAN-HMS	1.85	550	3600	0.65
PAN-UHM	2.00	560	1850	0.40
MPP-HM	2.15	900	3500	0.40
Metal fibres				
Steel	7.8…7.9	210	200…2500	1.0…2.0
Aluminium	2.8	72	460	-
Other inorganic fibres				
Al_2O_3	2.7…4.1	150…380	1700…2930	0.4…1.1
SiC	2.35…3.14	170…420	1500…3600	0.4…1.1
Basalt	2.75	89	2000…4840	3.15

structural applications in space, aviation, surgical tools, and sports and leisure. Their high stiffness and strength combined with a low density enables highest structural efficiency which cannot be achieved by other materials. This high performance stems from their inner structure: structural-grade carbon fibres are made up of at least 90 % graphite layers (crystalline sheets of pure carbon) which are oriented parallel to the fibre axis,[45] rendering the fibre itself anisotropic for the sake of high stiffness and strength along its orientation. This structure is realized during production using controlled pyrolysis of an organic precursor fibre containing a high carbon content and, preferably, a molecular structure which is already aligned in fibre direction. The most common precursor is polyacrylonitrile (PAN), a thermoplastic polymer. Some carbon fibres are still made from melt-spun mesophase pitch (MPP). Alignment of the molecules is realized via drawing (stretching) of the fibres. For the fabrication of carbon fibres, such precursor fibres are first stabilized through thermal oxidation, before moving into a carbonization stage. There, the carbon content of the fibre compound is maximized by thermally degrading the material and intentionally removing non-carbon elements. Here, most carbon atoms already rearrange into the allotrope graphite and depending on the chosen process parameters, the final structure of a high tensile (HT), an intermediate modulus (IM), or a high modulus (HM) fibre is achieved. To realize fibres exhibiting high modulus and strength (HMS) or ultra-high modulus (UHM), the thus carbonized fibre is then subjected to even higher temperatures, which further increases the graphite content. During this stage, PAN-based fibres can additionally be stretched to aid the conversion of disoriented crystallites into the aligned graphite structure and thus further increase the anisotropy of the fibre.[45] One further type are high strain and tenacity (HST) fibres, which are optimized for a high elongation at break and which usually also exhibit high strength (see Table 4.2). Following the thermal treatment, the surface of the fibres is chemically cleaned and prepared for further processing into a composite. As a drawback compared to other fibre formation processes, the production of carbon fibres has a comparatively low throughput and requires a high energy input to realize the pyrolytic process steps, making it costly. Also, the entire process chain from the precursor to the carbon fibre is performed on spread tows (bundles), meaning the single filaments are already in contact with each other. The only point of access to apply a sheath for the creation of a BCF is during or immediately following the formation of the precursor fibre. However, a thermoplastic polymer sheath intended to be processed as the composite matrix would not survive the thermal treatments of carbonization and graphitization. Whether or not this entire process chain can be performed on a monofilament is doubtful, given the high thermal and mechanical loads the material is subjected to. Using carbon fibres as the core for hybrid BCF production is therefore unlikely to be feasible, but not entirely impossible.

Metal fibres are rarely used for pure reinforcement purposes, but rather for their functional properties, e.g. to increase the composite's electrical conductivity or to enable internal Joule heating for welding. More sophisticated applications make use of wires made from shape memory alloys as actuation devices[58,59] or to repair damage.[60] Fibre formation methods for metals which create single filaments result in rather large diameters in the range of a few millimeters. Such wires are stable enough to be processed into BCF as monofilaments. Thinner metal fibres are often made by embedding conventionally drawn wires in a matrix metal with lower chemical stability, but higher ductility (e.g. copper) and drawn through a tapered die. The matrix is then chemically removed, leaving multifilaments with diameters ranging from 4 µm to 25 µm.[45] However, such bundles render it difficult to access the single fibres for the application of a thermoplastic sheath.

Other inorganic fibres which are frequently used to reinforce polymer composites are ceramic and mineral fibres, other than glasses. Notable examples are aluminium oxide, silicon carbide, and basalt. Whereas basalt fibres may be melt-spun quite similarly to glass fibres, there are various methods used to form ceramic fibres. Oxidic ceramics are processed in "dispersion spinning" and "solvent spinning", while non-oxidic silicon carbides can be melt-spun from polycarbosilane. Both processes result in a green fibre which is then flame-burned to convert into the final ceramic fibre.[45] As is the case for carbon fibres, a hypothetical sheathing stage could only be applied following this sintering step, requiring the entire process to work on the monofilament level.

Based on the outlined fibre formation methods, the individual advantages of the different materials, and their commonality in the polymer composites industry, glass fibres were selected as an initial material platform to assess the feasibility and viability of hybrid BCF production. First and foremost, melt spinning provides easy access to the single filaments, so a sheathing stage can be implemented between the spinning nozzles and the point where the fibres are bundles into a roving. An alternative material class which offers a broader choice of sheathing methods are polymeric fibres. Nevertheless, it was asserted that principles of BCF production which can be demonstrated in-line with glass melt spinning are likely easier to transfer to polymer spinning processes rather than vice-versa.

4.2 A brief overview of sheathing processes

Following the choice of glass as reinforcing material to be employed in BCF-derived composites within this study, a suitable strategy on the application of the thermoplastic polymer sheath during BCF production had to be found. The following paragraphs outline a number of general approaches and assert their potential advantages and disadvantages.

An obvious strategy to manufacture sheath-core bicomponent fibres is co-extrusion. As is mentioned in section 3.3, this method is successfully employed to fabricate fibres from two different polymers[35–40] or from two different glasses.[41–43] Successfully pairing any glass with any thermoplastic polymer, however, is rendered unlikely by the gap between the high melt temperatures of glass and the often lower degradation temperatures of most polymers. Nevertheless, Owens Corning's 1997 patent describes the principle of glass/polymer co-spinning using a rotary spinning head with an integrated cooling system.[44] Their approach yields highly warped fibres with a side-by-side material arrangement in the cross-section, which cannot be used for the purposes intended in this study. Still, this example highlights that co-extrusion or co-spinning is a possible path to manufacture hybrid glass/polymer BCF, however difficult it might be.

Hot melt coating as a categorical approach involves the implementation of an in-line coating stage following glass fibre formation. This offers the benefit of the glass having cooled significantly below degradation temperature of the polymer at the point where the sheath is applied. An intuitive consideration coming to mind is that the residual heat within the newly formed fibres might be used to melt and drag along polymer from a solid reservoir. However, because of the velocities at which glass fibres are spun and their fine diameter, they lose almost all heat within a short distance after exiting the nozzle.[57,61,62] Therefore, for this approach to work, the heat carried by the glass would need to be retained with most accurate control or additional heat would need to be introduced just prior to the fibres coming into contact with the polymer, without melting the entire polymer reservoir. Of course, another option would be to do just that: melt the polymer at a specifically chosen temperature and employ a liquid coating process. This allows a wide variety of methods to be considered, from dip- or roll-coating to curtain- or slit-blade-coating, or any combination thereof. However, it needs to be considered that the thermoplastic melts of technical polymers exist on a wide spectrum of viscosities, the lower end of which is around the order of $\sim 10\,\mathrm{Pa\,s}$, which could potentially be too high to apply the desired coatings in a controlled manner while maintaining the high fibre velocity required for glass melt spinning.

For many polymers, the issue of high viscosity can be overcome with the use of a suitable solvent or solvent mixture, while still employing a liquid coating method. Requirements on the used solvent are that it significantly lowers the fluid viscosity compared to the pure polymer melt, that it is sufficiently volatile to be quickly removed prior to bundling the fibres, and that it is neither flammable nor that its fumes form explosive mixtures with air. The latter restriction can only be considered to be overcome if the process equipment is sufficiently explosion-proof to guarantee worker safety and if the heat used to melt the glass can be sufficiently and safely decoupled from the coating and solvent treatment systems. However, if a given polymer/solvent combination meets these requirements, the processing windows offer by liquid coating approaches can be significantly enlarged.

Alternative coating methods like powder-coating[62] or overjacketing,[26,27] though commonly used on fibre rovings, do not provide the control needed to produce even coatings at the fibre level. Precision coating processes such as chemical vapour deposition and thermal spraying provide excellent control over the coating thickness but are considered far too slow to be economically viable for this application.

The arguments for and against the aforementioned sheathing processes to be used for the fabrication of BCF in-line with glass melt spinning do not allow for a clear conclusion as to which method offers the largest benefit. It is the purpose of this part of the study to shed light on some open questions regarding the feasibility of combining a selection of these processes in-line with glass melt spinning, in particular with the direct roving process. The following chapters therefore present the principles and theory of glass melt spinning in more detail, followed by treatments of various coating methods using both analytical and experimental approaches. The last chapter in part II then presents the design of an actual continuous in-line coating process and provides experimental proof of its function to manufacture glass/polymer BCF.

5

GLASS FIBRE SPINNING

To understand how glass can be spun into fibres, it is helpful to start with a more detailed definition of what glasses are: “A glass is an inorganic substance in a condition which is continuous with, and analogous to, the liquid state of that substance, but which, as a result of a reversible change in viscosity during cooling, has attained so high a degree of viscosity as to be for all practical purposes rigid.”[57,63] Therefore, even though the term “melting” is often used to describe an apparent change in a glass’s state of matter when subjected to high temperatures, glasses do in fact not exhibit a distinct melt temperature at which a sudden change in behaviour can be identified. With reference to glasses, the term “melt” is therefore generously used simply to describe a glass at such high temperatures where its viscosity is low enough for it to be processed as a liquid. Furthermore, the aforementioned definition of glasses already gives first insight into why they can easily be spun to thin fibres. At different temperatures, the arrangement of atoms within the compound does not change significantly, which is a simple explanation for the high stability that glass melts possess. The intramolecular forces remain of the same type as at room temperature, where they provide high strength and stiffness.

The basis of nearly all commercial glasses is silica, or silicon oxide (SiO_2). As silica is heated, it gradually softens, until it starts to decompose at temperatures crossing $\sim 2000\,°C$.[57] It is mostly sourced from the mineral quartz, a crystalline allotrope of silica. It is converted to a vitreous, or glassy, state simply by heating until it appears fluid and by subsequent cooling. Only prolonged tempering around ~ 1200 °C enables crystals to form. Engineering glasses based on silica as the basic network former are commonly modified with the addition of other oxide, whose function can be classified into three groups: other network formers, mostly boric oxide and alumina; network modifiers like calcium oxide or quicklime, baria, sodium oxide, or potassium oxide; and intermediate oxides, e.g. magnesia, beryllia, or titania, which can act both as network formers or modifiers depending on the overall composition of the glass and how it is made.[57] Historically, different glass compositions were primarily studied in order to alter the compound's electrical properties, mostly for insulation purposes. Furthermore, the composition affects the mechanical performance of a glass as well as its resistance against chemical and electrochemical (corrosion) attack. The bulk volume of glass being processed into fibres for structural use is composed of electrical glass (E-glass), with boric oxide and alumina as the main additives. Such glasses are generally referred to as borosilicates or alumina-borosilicates. Their benefit for use in structural applications is mostly their low cost, as E-glasses are historically the most-spun types of glass. If higher mechanical performance, chemical resistance, or specific electrical properties are required, other compositions are available (see Table 4.2 for examples).

5.1 The direct roving process

To form glass into straight continuous fibres, a continuous stream of either freshly refined glass melt or spherules, pellets, shards, or powder is led into a furnace. This furnace contains the bushing, a precious metal container with spinning nozzles on the bottom, which is usually made from a platinum-rhodium alloy and is heated using electrical current. The remainder of the furnace is made from refractory and stones and held together by a metal frame. Inside it, the temperature (1200 °C to 1500 °C)[54,64] and filling height of glass melt are maintained constant to guarantee a constant viscosity (50 Pa s to 100 Pa s)[57] and pressure at the nozzle inlets. The nozzles themselves are simply tubes extending from the bottom of the bushing and can exhibit constant, tapered, or staggered cross-sections to tailor the flow resistance of the nozzle over its length. Each nozzle forms a monofilament simply by the steady stream of glass flowing out, driven by gravitational acceleration.

In the direct roving process, illustrated in Fig. 5.1, the continuously spun fibres are guided downwards and bundled on the gathering shoe.The latter can be composed of a guide roll, an eyelet, or any similar geometry. Following the gathering shoe, the now bundled roving of glass fibres is collected on a collet using a traversing winder with automatic change-over to a second collet. Following the change-over, a worker can extract the full collet from the winder, remove the fibre cake from the collet and put the latter back on the winder, ready for the next batch.

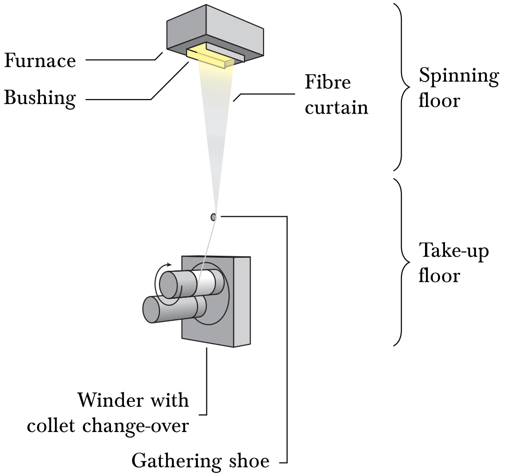

Figure 5.1:
Schematic illustration of the direct roving glass melt spinning process and its main stages.

In industrial settings, the fibres are additionally treated with a so-called sizing prior to being bundled. The sizing agent used to modify the surface of fibres intended to reinforce thermoplastic polymers is often an aqueous solution of silanes and other additives. This treatment is intended to improve the adhesion of the matrix polymer to the fibres in the final composite and to improve handling of the fibre roving throughout the entire value chain. Preforming methods like weaving, braiding, or stitching in particular exert considerable stresses combined with frictional loads on the rovings. Sizing lowers the risk of fibre breakage during these processes by acting as a lubricant. Sizing the fibre curtain during spinning can be done in various ways, e.g. through a “sizing shoe”, which is a wide chute covered with a soft material and carrying the sizing solution. The fibre curtain is drawn over the rounded end of this chute and picks up the solution. A more prominently used method is vertical roll-coating, during which the curtain is drawn over a rotating applicator roll carrying the solution, with a very low wrapping angle ($\lesssim 10°$). This method has also been coined “kiss-roll coating”, as the fibre is said to briefly “kiss” the roll. It is discussed in more detail in chapter 8, where the method is investigated for the purposes of creating BCF.

5.2 Theory of glass melt spinning

To better understand the requirements on a potential sheathing process to be implemented in the direct roving manufacture of glass fibres, the latter’s processing window regarding fibre velocity needs to be understood. The following paragraphs assert this processing window via a simple yet commonly accepted model for the volumetric flow of glass through the bushing. Due to the rapid cooling of the glass upon exiting the nozzle, the filaments are fully solidified by the time they are collected on the winder. The diameters of the glass fibres spun in this manner are determined by the volumetric flow rate of glass out of the nozzle and the line speed of the winder.

The volumetric flow rate Q_v through a tubular geometry, such as that of a glass spinning nozzle, can be modelled by the Hagen-Poiseuille law for laminar stationary flow, as shown in Eq. 5.1. The pressure difference causing the flow is given by the hydrostatic pressure p_i at the inlet of the nozzle and the atmospheric pressure p_o at its outlet.

$$Q_v = \frac{p_i - p_o}{R} = \frac{\rho_g g h_g}{R} \tag{5.1}$$

The hydrostatic pressure is dependent on the density ρ_g of the glass melt, the gravitational acceleration g, and the filling height h_g of the glass melt inside the bushing. R denotes the resistance to flow given by the nozzle. For a purely cylindrical geometry without tapers or counterbores, R is calculated according to Eq. 5.2[57] and depends on the glass melt viscosity η_g and the length L and inner diameter d of the tube, respectively.

$$R = \frac{32}{\pi}\eta_g \frac{L}{d^4} \tag{5.2}$$

By applying the principle of conservation of mass, the radius of the spun filament r_f can be determined by equating the volumetric flow rate through the nozzle and the volumetric take-up rate of the spun filament as shown in Eq. 5.3, where V denotes the line speed of the filament.

$$V r_f^2 = \frac{g}{32}\frac{\rho_g}{\eta_g}\frac{h_g d^4}{L} \tag{5.3}$$

Table 5.1 provides the process parameter ranges employed in industrial-scale processes to spin glass fibres with diameters ranging from 10 µm to 20 µm. The range of potential line speeds in glass spinning may be expanded, within limits, by altering the parameters in Table 5.1. Since changes in the chemistry of the glass are limited and the ranges in nozzle diameters and lengths are already considerable, the easiest parameter to manipulate is the filling height h_g, which may vary from 30 mm to 150 mm. Lower filling heights result in regular tearing of the glass melt stream because the residence time of the glass pellets within the bushing is too short to ensure a homogeneous temperature distribution and to eliminate air bubbles in the melt when using the re-melt approach. Higher filling heights are hard to achieve because it is difficult to homogeneously temper larger bushings. Respecting the rest of the parameter ranges listed in Table 5.1, and assuming a density of $2.5\,\mathrm{g\,cm^{-3}}$ for the glass melt, solving Eq. 5.3 yields a minimum and maximum line speed of $0.38\,\mathrm{m\,s^{-1}}$ and $1796\,\mathrm{m\,s^{-1}}$, respectively. Literature on the subject gives

Table 5.1: Typical ranges of parameters employed in industrial glass melt-spinning.

Glass melt viscosity η_g for successful melt-spinning* [57]	50 Pa s to 100 Pa s
Spinning temperature [54,64]	1200 °C to 1500 °C
Nozzle diameter d [57,64,65]	1 mm to 2.5 mm
Nozzle length L [57,64,65]	2 mm to 6 mm
Filling height h_g [61]	~ 90 mm
*Corresponding temperature for E-glass [66]	~ 1240 °C

a narrower range of line speeds from 8 m s^{-1} to 83 m s^{-1} [57,64] which are used in current industrial glass spinning processes. The cost-effective production of fibreglass for structural composites operates at line speeds between 40 m s^{-1} and 60 m s^{-1}.[54,57,65] In practice, the maximum line speed is limited to ~ 100 m s^{-1} due to effects which cause fibre breakage, e.g. vibrations from the take-up winder, minute cross-winds, or simply disturbances in the frictional forces the fibres are subjected to within the nozzle, at the gathering shoe, or the bobbin. Therefore, in order to be implemented directly into a viable glass spinning process, a sheathing system must be able to deposit coatings with the desired properties at line speeds between 0.38 m s^{-1} and 100 m s^{-1}, and preferably above 40 m s^{-1} to be as cost-effective as conventional fibreglass production.

6

SOLUTION DIP-COATING

This chapter treats the feasibility of implementing a solution-based dip-coating process in-line with glass fibre spinning, as schematized in Fig. 6.1, to produce hybrid bicomponent fibres with properties which would make them interesting for structural-grade glass fibre reinforced thermoplastic composites. Analytical models for glass fibre spinning and dip-coating suggest that a narrow processing window exists which would yield hybrid bicomponent fibres with dimensions suitable for use in structural composites. Experimental investigations confirmed that implementing a dip-coating process in-line with glass fibre spinning is possible, however this approach does not offer the uniformity of coating and high coating speeds required for the robust production of hybrid bicomponent fibres.

Structural composites typically use glass fibres with diameters between 10 μm and 20 μm, and have final fibre volume contents between 0.3 and 0.7. With these values in mind, analytical models are applied to identify conditions under which glass spinning and dip-coating can be implemented in series to yield hybrid bicomponent fibres with the desired range of properties. High-speed ($0.8\,\mathrm{m\,s^{-1}}$ to $1.15\,\mathrm{m\,s^{-1}}$) dip-coating experiments are used to validate the theoretical processing window, and the feasibility of producing hybrid bicomponent fibres suitable for thermoplastic composite preforms is demonstrated. This study presents results on the dip-coating of glass fibres in poly(ester-

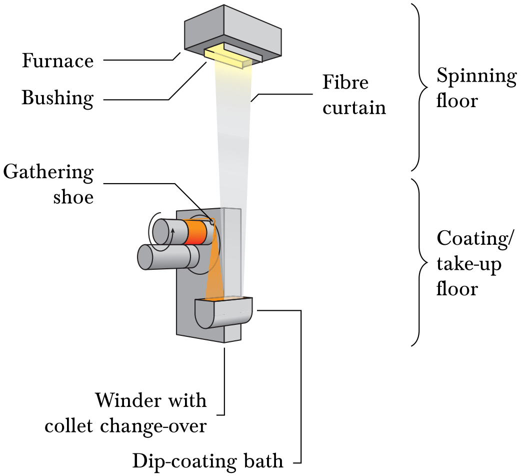
Furnace
Bushing
Fibre curtain
Spinning floor
Gathering shoe
Coating/ take-up floor
Winder with collet change-over
Dip-coating bath

Figure 6.1: Schematic of the glass melt spinning process with the proposed in-line dip-coating step.

amide)-trichloromethane solutions. The theory on dip-coating and the experimental methods developed in this study are applicable to any polymer solution that is stable, Newtonian, and able to dry quickly.

6.1 Properties of coating materials

Poly(ester-amide) (PEA), an aliphatic segmented block co-polymer with a semi-crystalline thermoplastic structure, was provided by Dow Europe GmbH. Dilute solutions of PEA in trichloromethane (ReagentPlus® 132950, Sigma-Aldrich) with volume fractions v_p ranging from 0 vol% to 15.13 vol% were prepared for characterization and dip-coating experiments. Higher concentrations were found the cross the limit of solubility at room temperature and were therefore not tested. The densities, viscosities, and surface tensions of the polymer solutions are required to model the dip-coating behaviour according to the theory presented in section 6.2 and are summarized in Fig. 6.2. Details about the characterization methods and resulting material data are provided in the following subsections.

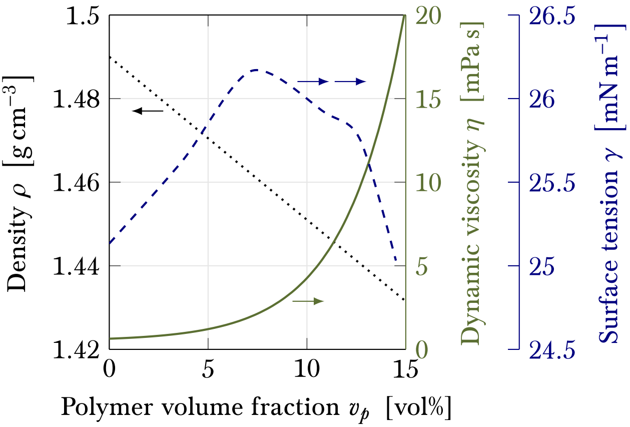

Figure 6.2:
Measured values for density (dotted line, black), dynamic viscosity at a shear rate of 100 s^{-1} (solid line, green), and surface tension (dashed line, blue) of the polymer solution versus polymer concentration.

6.1.1 Density

The densities ρ of the solutions were calculated assuming no change in volume, in accordance with the rule of mixtures shown in Eq. 6.1.

$$\rho = v_p \rho_p + (1 - v_p)\, \rho_s \tag{6.1}$$

In Eq. 6.1, ρ and ρ_i denote the density of the solution and the densities of the constituents, respectively, and v_p is the volume fraction of the polymer. The density ρ_p of the poly(ester-amide) is 1.10 g cm^{-3} and the density ρ_s of the trichloromethane is 1.49 g cm^{-3}.

6.1.2 Rheology

The rheological behaviour of the solutions containing various concentrations of PEA were characterized in an Anton Paar MCR 502 rotational rheometer at 25 °C using concentric cylinders with a double-wall couette geometry (DG 26.7). The volume fractions tested were 2.35 vol%, 4.68 vol%, 9.25 vol% and 13.71 vol% and from each concentration, two samples were loaded into the geometry and tested twice, resulting in four measurements per concentration. Oscillatory tests were performed to identify the complex rheology. Amplitude sweeps from 0.01 % to 100 % at a frequency of 10 rad s^{-1} showed constant values for all samples, respectively, indicating that the limit for linear viscoelasticity was not reached. Subsequent frequency sweeps ranging from 1 rad s^{-1} to 100 rad s^{-1} at an amplitude of 100 % revealed phase shift angles greater than 85°, indicating that the rheological behaviour is dominated by viscous drag and that elastic effects are negligible. Finally, flow curves were measured to determine the viscosities' shear rate dependence, scanning a range from 10 s^{-1} to 1000 s^{-1}. The obtained viscosity data is shown in Fig. 6.3. It is evident that the solutions generally show Newtonian behaviour in the range of shear rates tested, while the samples containing the lowest polymer concentration seem to exhibit a slight trend towards shear-thinning. The influence of polymer concentration on the solution's dynamic viscosity is illustrated in Fig. 6.4, where the viscosity data obtained at a shear rate of 100 s^{-1} is plotted. The data in Fig. 6.4 is fitted with an exponential curve as shown in Eq. 6.2, resulting in a

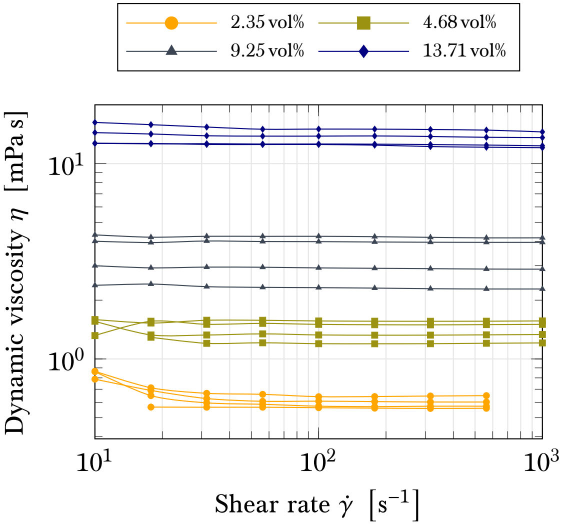

Figure 6.3: Flow curves measured from solutions of poly(ester-amide) in trichloromethane showing Newtonian behaviour with a slight trend towards shear-thinning.

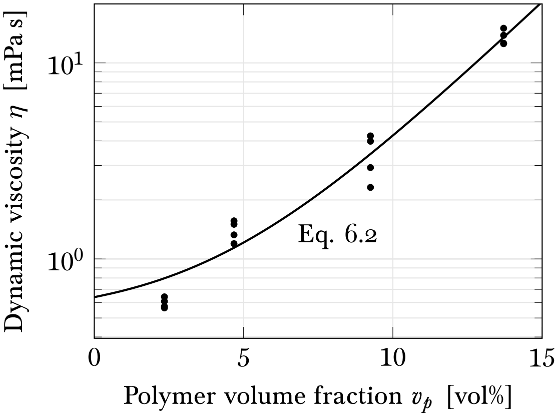

Figure 6.4:

Dynamic viscosity of the polymer solution measured at a shear rate of $100\,\mathrm{s}^{-1}$ versus polymer concentration and exponential curve fit thereof.

goodness of fit of $R^2 = 0.984$.

$$\eta = 1.33 \times 10^{-4}\,\mathrm{Pa\,s} \cdot \exp\left(33.4 \cdot v_p\right) + 5.06 \times 10^{-4}\,\mathrm{Pa\,s} \tag{6.2}$$

In Eq. 6.2, the polymer volume fraction v_p is unitless and the resulting viscosity η is given in Pa s.

6.1.3 Surface tension

The surface tension of the different solutions was characterized using the pendant drop method performed on a Krüss DSA100 drop shape analyser. An exemplary image of a pendant drop produced within this study is given in Fig. 6.5. The volume fractions tested were 0 vol%, 3.7 vol%, 7.2 vol%, 10.9 vol%, 12.7 vol% and 14.5 vol% and from each concentration, at least 30 droplets were produced with each droplet being imaged 31 times. The droplets were extruded through a steel cannula with a flat end and an outer diameter of 1.8 mm. The densities used for the fitting were calculated according to Eq. 6.1. Fig. 6.6 presents the obtained data, with the actual measurements represented as box plots and an added cubic Bézier spline interpolation of the median, quartile, and extreme values over the range of concentrations tested. The obtained measurements show only small changes in surface tension

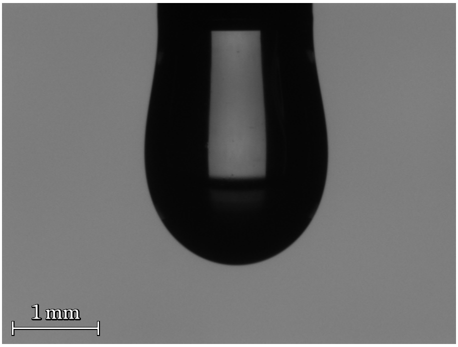

Figure 6.5:

Exemplary pendant drop image taken from a solution of 10.9 vol% poly(ester-amide) in trichloromethane.

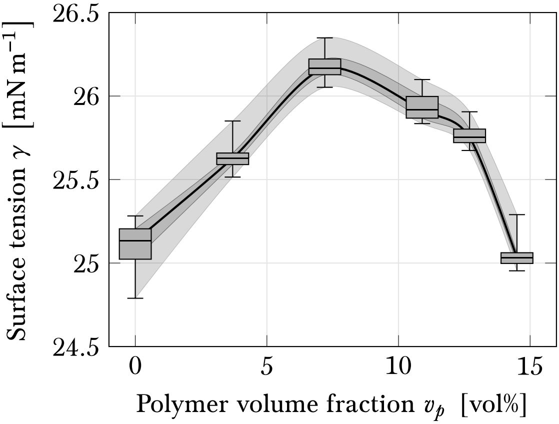

Figure 6.6:

Surface tension of the polymer solution versus polymer concentration and cubic Bézier spline interpolation thereof. The distributions at each measured concentration are represented by the median (line inside the box), the first and third quartiles (lower and upper ends of the box) and the minimum and maximum values (lower and upper whiskers).

with varying polymer concentration, ranging from 25.1 mN m for pure trichloromethane to a maximum of around 26.2 mN m at a polymer concentration of 7.2 vol%.

6.2 Theory of dip-coating

Dip-coating describes the process of coating an object by dipping it into a fluid bath and subsequently withdrawing it from that bath. Provided that the intermolecular forces between the fluid and the substrate encourage wetting and that the withdrawal velocity is sufficiently high, some of the fluid will be entrained by the object as it exits the bath. This liquid layer remains as a coating on the object's surface. The main governing forces which define the flow of the fluid are viscous drag and surface tension of the fluid. These forces work antagonistically against each other since viscous drag draws out adjacent fluid molecules from the bath and thereby disturbs the fluid surface which is held together by surface tension.[67] The relative importance of these two forces is commonly represented via the dimensionless capillary number Ca, as defined in Eq. 6.3, where η and γ represent the fluid's dynamic viscosity and surface tension, respectively, and V is the withdrawal speed of the substrate.

$$Ca \triangleq \frac{\eta V}{\gamma} \tag{6.3}$$

In the case of dip-coating, a very low capillary number ($Ca \lll 1$) means that the system is governed by surface tension and that not enough kinetic energy is introduced to significantly disturb the free surface of the fluid. Intermediate capillary numbers ($Ca \ll 1$) represent a state in which the free surface is disturbed by a moving part of the system and that this disturbance affects a wider region of fluid through the viscous drag. Capillary numbers on the order of unity or higher represent a state in which either the withdrawal velocity or the viscosity of the fluid introduce so much drag that the surface energy cannot hold back enough liquid to only form a thin film on the substrate; in this case, the coating thickness has reached a scale at which it may develop its own dynamics. An example of this is unstable flow akin to a Plateau-Rayleigh instability, which expresses itself in a time-dependent variation of the coating thickness.[68]

In the case of vertically withdrawn fibres, h_l can be calculated using the law found by Landau, Levich, and Derjaguin,[69,70] shown in Eq. 6.4.

$$h_{l,\mathrm{LLD}} = 1.34 r_f Ca^{\frac{2}{3}} \tag{6.4}$$

Note that Eq. 6.4 is valid only when the thickness of the coating is much smaller than the radius of the fibre. For thick coatings, such as those required for the proposed hybrid bicomponent fibres, a correction as derived by White and Tallmadge[71] is applied (Eq. 6.5).

$$h_{l,\mathrm{WT}} = \frac{1.34 r_f Ca^{\frac{2}{3}}}{1 - 1.34 Ca^{\frac{2}{3}}} \tag{6.5}$$

It is clear that this expression exhibits a singularity as the capillary number approaches a value of 0.645. This would correspond to a full entrainment of the quasi-infinite liquid bath and does not represent reality. The singularity is purely an artefact of the model's derivation.[67,71] Eq. 6.5 is reported to diverge from experimental data at capillary numbers greater than ~ 0.1. For capillary numbers > 0.1, the White and Tallmadge model generally underestimates the thickness of the entrained layer due to the influence of gravity and inertia.

In order to extend the applicability of the model to low viscosity fluids and high withdrawal speeds, De Ryck and Quéré included the effects of inertia in a revised dip-coating model.[72] The influence of inertia in comparison to capillary force may be assessed via the dimensionless Weber number We, as defined in Eq. 6.6, where ρ is the fluid's density and r_f is again the radius of the cylindrical substrate.

$$We \triangleq \frac{\rho V^2 r_f}{\gamma} \tag{6.6}$$

The Weber number can be used to estimate the coating thickness $h_{l,\mathrm{DRQ}}$ in the presence of inertial forces, as shown in Eq. 6.7.

$$h_{l,\mathrm{DRQ}} = \frac{1.34 r_f Ca^{\frac{2}{3}}}{1 - We} \tag{6.7}$$

This model also exhibits a singularity as the Weber number reaches unity and does not represent the reality within that region. In comparison to experimental data from different sources,[67] Eq. 6.7 provides a better fit than the model of White and Tallmadge (Eq. 6.5). Nevertheless, Eq. 6.7 still underestimates the coating thickness in cases where the capillary number exceeds unity, and overestimates it in cases where the capillary number is less than one but the Weber number approaches unity.[67] This is referred to as the viscoinertial regime, which is mostly found when using low viscosity fluids, such as water, alcohol, or most other solvents.

Quéré states that accurate calculations for thick coatings and high withdrawal velocities are difficult to achieve, even when using numerical methods.[67] Still, Eq. 6.5 and Eq. 6.7 may be used to estimate the relation between fiber velocity and coating thickness in terms of order of magnitude and with respect to the polymer solutions used. In the high-speed solution-based dip-coating process proposed here, both viscosity and inertial effects are expected to impact the coating thickness. Therefore, the model of De Ryck and Quéré is expected to better predict the results of the experiments.

6.2.1 Potential in-line processing window

The normalized liquid coating thicknesses h_l/r_f predicted by Eq. 6.5 and Eq. 6.7 are plotted as a function of the withdrawal velocity in Fig. 6.7 for different polymer concentrations and for a fibre diameter of 15 µm.

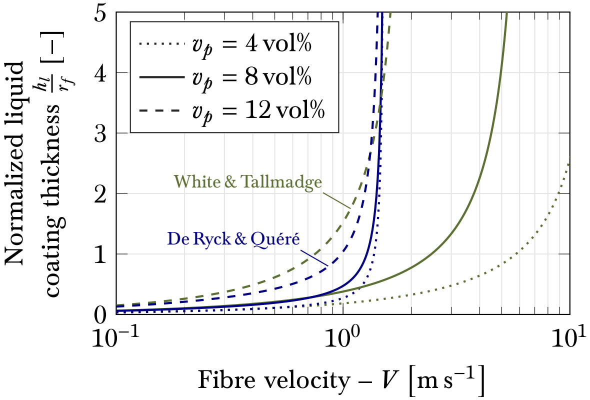

Figure 6.7: Predictions of the liquid coating thickness h_l according to Eq. 6.5 and Eq. 6.7 normalized over the fibre radius r_f plotted against the fibre withdrawal velocity V for different concentrations v_p of poly(ester-amide) in trichloromethane and for a glass fibre diameter of 15 µm.

The plot shows that the predictions given by the model of De Ryck and Quéré converge towards the same singularity. On the other hand, the capillary number depends also on the fluids viscosity, which is heavily influenced by even minor changes in the polymer concentration. This explains the shift between the singularities of the White and Tallmadge predictions made for the different concentrations.

Note that the models above estimate the liquid coating thickness h_l which includes the solvent. Therefore, to establish a relationship between this thickness and the final fibre volume fraction after the solvent has been completely evaporated, the polymer concentration in the solution has to be taken into account. Eq. 6.8 provides the formula for the fibre volume fraction v_f of the hybrid bicomponent fibres after the solvent has been removed, depending on the core fibre radius r_f, the volumetric polymer concentration of the coating solution v_p, and the immediate liquid coating thickness h_l.

$$v_f = \frac{r_f^2}{h_l^2 v_p + 2 h_l v_p r_f + r_f^2} \tag{6.8}$$

The velocity window at which fibres may be dip-coated is evaluated by inserting Eq. 6.5 or Eq. 6.7, respectively, into Eq. 6.8. This is done for different withdrawal speeds and for different polymer concentrations in the coating solution. Fig. 6.8 shows the resulting model predictions as contour lines of constant fibre volume fraction depending on the polymer concentration and the fibre velocity and assuming a core fibre radius r_f of 7.5 µm, that is a fibre diameter of 15 µm. Note that the results obtained using fibre radii between 5 µm and 10 µm are indistinguishable in this depiction. Fig. 6.8 further provides contour plots of the capillary and Weber numbers.

It is evident that in the given case, the model proposed by De Ryck and Quéré differs significantly from the one presented by White and Tallmadge. In part, the reason for this is that the coating thicknesses required to achieve final fibre volume fractions of 0.7 or lower are high enough to demand capillary numbers which are close to the limitations of the models to yield accurate predictions. This is evident for the White and Tallmadge prediction and especially for the De Ryck and Quéré prediction at low polymer concentrations, where the contour lines asymptotically approach the singularity introduced by the normalization in the respective model. Namely, those singularities are given by a capillary number $Ca = (1/1.34)^{3/2} \approx 0.645$ for the prediction of White and Tallmadge and by a Weber number $We = 1$ for the model by De Ryck

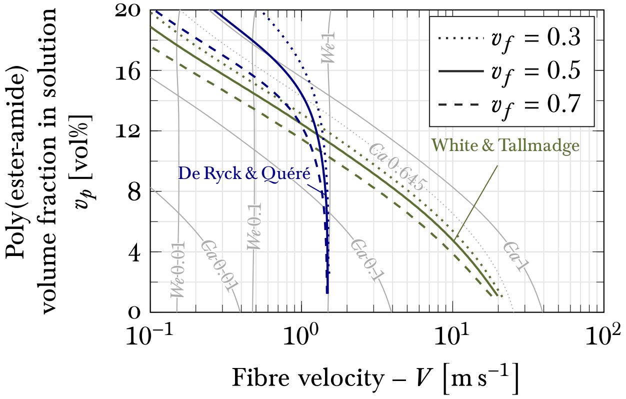

Figure 6.8: Predicted isolines of final fibre volume fraction of bicomponent fibres yielded from the solution dip-coating process plotted against the fibre velocity (abscissa) and the polymer concentration in the coating solution (ordinate). In addition, isolines for different values of *Ca* and *We* are shown in grey.

and Quéré. Furthermore, it is noticeable that De Ryck and Quéré's model predicts that higher velocities are needed at high polymer concentrations to achieve the same fibre volume content, but that this prediction crosses the one by White and Tallmadge as the Weber number approaches unity. This illustrates that within the depicted range of polymer volume fractions, lower concentrations provide also lower viscosities and this manifests itself in a transition into the viscoinertial regime, where the Weber number takes greater influence. This has a significant influence also on the prediction of the resulting fibre volume fraction's sensitivity to changes in withdrawal speed: generally, lower polymer concentrations tend to increase the sensitivity to relative changes in fibre velocity. However, this effect is much less pronounced in the prediction proposed by White and Tallmadge.

Neither theory provides a lower limit for the withdrawal speed. In reality, this limit is given by the maximum solubility of the polymer-solvent combination, which has not been reached for the materials and concentration ranges considered in this study. This is because the process window is defined as the range of fibre velocities in which hybrid bicomponent fibres with fibre volume fractions between 0.3 and 0.7 are produced, meaning that lower line speeds need to be compensated by higher solution viscosities, which in turn means using higher polymer concentrations.

The ranges of viable line-speeds for solution-based dip-coating and glass melt spinning are indicated in Fig. 6.9. It is clear that a solution-based dip-coating process cannot be implemented directly in-line with an industrial spinning plant which operates at speeds of 40 m s^{-1} to 60 m s^{-1}. However, it is possible to obtain a usable overlap by modifying the glass spinning parameters to allow for lower fibre velocities. The existence of this narrow processing window between velocities of 0.38 m s^{-1} to 20 m s^{-1} requires experimental validation.

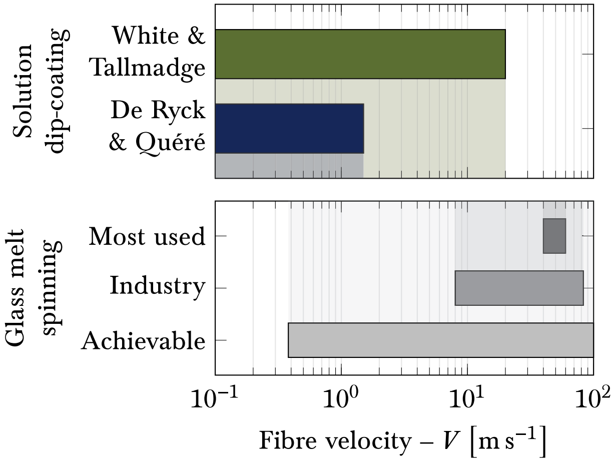

Figure 6.9: Comparison of predicted fibre velocities in the dip-coating process with those in glass melt spinning.

6.3 Experiments

6.3.1 Reinforcement fibres and coating process

Single E-glass filaments with lengths ranging from 2 m to 4 m and a mean diameter of 12 µm were manually separated from a roving containing

204 fibres. The roving was spun at the Institute for Polymer Research in Dresden, Germany, and sized with 1 wt% 3-aminopropyltriethoxy silane (APTES). Individual filaments were passed through a steel wire ring immersed in a test tube containing a solution of poly(ester-amide) (PEA) (Dow Europe)[73] in trichloromethane (ReagentPlus® 132950, Sigma-Aldrich) with a polymer concentration of 6.6 vol%. They were then withdrawn vertically at velocities ranging from 0.8 m s^{-1} to 1.15 m s^{-1} and wound onto a rotating axle with a diameter of 18 mm located at a distance of 414 mm or 1545 mm from the bath (Fig. 6.10). The withdrawal velocity was recorded via a rotary encoder at the axle.

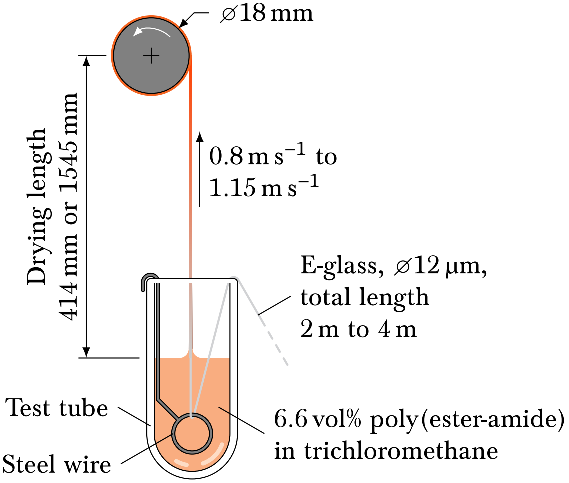
⌀18 mm
Drying length
414 mm or 1545 mm
0.8 m s^{-1} to
1.15 m s^{-1}
E-glass, ⌀12 µm,
total length
2 m to 4 m
Test tube
Steel wire
6.6 vol% poly(ester-amide)
in trichloromethane

Figure 6.10:

Schematic of the experimental setup for dip-coating of a glass monofilament with a polymer solution.

6.3.2 Scanning electron microscopy (SEM)

The coated fibre specimens were divided into samples for transverse and cross-sectional imaging. To obtain the cross-sectional images, the lengths of all fibres were first sputter-coated with 6 nm of platinum using a Safematic CCU-010 coater and then embedded vertically in epoxy. The epoxy was cured and the samples polished to obtained a smooth cross-sectional surface of the fibres. The platinum coating was used to provide better contrast between the polymer sheaths and the epoxy under the microscope. All samples were then imaged in a Zeiss LEO 1530 (Gemini column) scanning electron microscope.

6.3.3 Image processing

To determine the fibre volume fractions of the produced hybrid bicomponent fibres and the distribution of the matrix material on the glass fibres, the SEM images were processed by an image analysis routine implemented in MATLAB®, which extracted the mean glass core diameters of a set of bicomponent fibres from their cross-sectional micrographs (e.g. Fig. 6.13, p. 68) as well its distribution of total coated widths from the transverse fibre images (e.g. Fig. 6.12, p. 66). Finally, the algorithm derives a distribution of fibre volume fractions for each set of bicomponent fibres produced. A schematic overview of the routine is given in Fig. 6.11.

The basis of the analysis relies on image segmentation, which refers to the division of an image into regions of equal colour, intensity or texture to identify objects.[74] Therein each pixel with coordinates x and y is assigned an area A or B in the output image $F(x,y)$ by comparing the intensity value $f(x,y)$ in the input image to an afore-set threshold value T, as described in eq. 6.9.

$$F(x,y) = \begin{cases} A, & f(x,y) > T \\ B, & \text{else} \end{cases} \tag{6.9}$$

To determine the core diameters, ellipses are fitted to the perimeter of the glass cores' cross-sections in MATLAB®. Some images showed enough contrast to allow a semi-automatic determination of the diameter: first, edge detection was carried out using the Sobel method[75] to locate the core fibre perimeter.[74] By means of a series of MATLAB® built-in morphological operations, pixel connected regions which represented the fibre core are created. The main concept behind morphology is to adjust each pixel in the image according to its neighbouring pixels such that imperfections in the image are removed. To ensure that the area of the fibre core is enclosed within the edge, the boundaries are therefore dilated with a diamond-shaped structuring element. Thereafter, a flood filling operation with a user set seed location generates an area of equal intensity values overlapping with the area of the fibre core. The minor

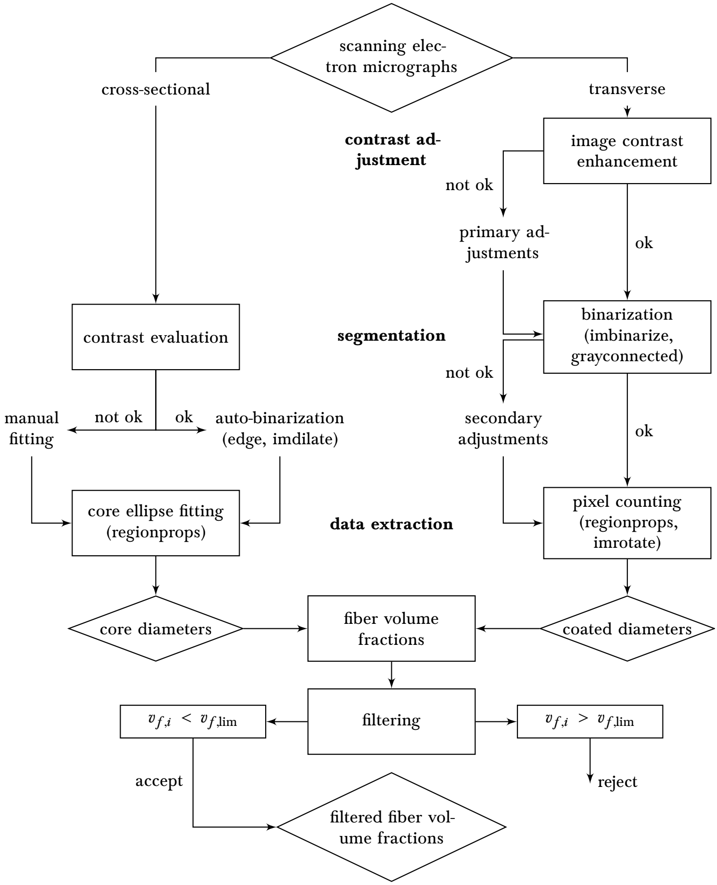
scanning electron micrographs
cross-sectional
transverse
contrast adjustment
image contrast enhancement
not ok
primary adjustments
ok
contrast evaluation
segmentation
binarization (imbinarize, grayconnected)
not ok
manual fitting
not ok
ok
auto-binarization (edge, imdilate)
secondary adjustments
ok
core ellipse fitting (regionprops)
data extraction
pixel counting (regionprops, imrotate)
core diameters
fiber volume fractions
coated diameters
filtering
$v_{f,i} < v_{f,\text{lim}}$
$v_{f,i} > v_{f,\text{lim}}$
accept
reject
filtered fiber volume fractions

Figure 6.11: Principle of the transverse image analysis with MATLAB® using segmentation and image rotation to determine the coated diameter along the length of the fibre. Through the addition of the core diameter the fibre volume fraction at each position along the length of the fibre is determined. Eventually comparing the seventieth percentile of the resulting fibre volume fraction distribution ($v_f^{0.7}$) to the defined limit $v_{f,\text{lim}}$ allows filtering of the data and determination of the resulting average fibre volume fraction at each individual set of coating parameters.

axis of this segmented area, representing the cross-sectional area of the core fibre, is then determined through measuring the properties of the connected region via the regionprops-routine in MATLAB®.[74] The minor axis of each fitted ellipse was taken as the corresponding glass fibre's diameter, as the major axis of the ellipse is subject to variations in the angle at which the specimens were cut. Naturally, it was not possible to ensure a perfectly perpendicular cut for each filament.

The extraction of the distribution of coated diameters was performed using a semi-automatic routine coded in MATLAB®. Firstly, intensity image values above a user defined threshold are filtered to adjust the micrograph's contrast. Thereafter, if the contrast is not deemed sufficient, fibre boundary regions of similar intensity values are manually connected before further processing. This is followed by segmenting the image into black and white areas using Otsu's method[76]. Due to the nature of the scanning electron micrograph, output of this binarization is a representation of the white fibre boundaries with a black core area. Due to the different nature of the micrographs, in transverse direction the best results for connecting the core region with the boundary and thus the least loss of detailed features were achieved by the MATLAB® built-in grayconnected-function. Remaining holes or imperfections in the morphology are then corrected through region filling. Eventually, each fibre segment is subsequently aligned horizontally to the Cartesian pixel frame according to the area angle determined via the regionprops-function in MATLAB®. Taking measure of the width of the coated fibre at different positions along its length is then simply a matter of counting the pixels with high intensity inside every column i of the two-dimensional array and mapping the pixel count onto the scale of the image to yield the width in meters.

Both the core fibre diameters and the sets of coated fibre widths for every specimen can be used to calculate the distribution of fibre volume fractions $v_{f,i}$ within the specimen by taking the square of the mean glass core diameter $\overline{d_c}$ normalized by the corresponding total coated thickness $d_{t,i}$ at each position i along the fibre, as shown in Eq. 6.10.

$$v_{f,i} = \left(\frac{\overline{d_c}}{d_{t,i}} \right)^2 \tag{6.10}$$

Due to the coating method used, each imaged specimen included the first part of the glass core which was attached to the winder before starting the process and therefore remained uncoated. Employing the aforementioned post-processing method on imaged segments of that initial part of the filament would result in fibre volume fractions close to unity and would therefore falsify the total distribution of yielded fibre volume fractions. It is however difficult to filter out these segments, because the exact core diameter of the imaged fibre is unknown and only the mean core diameter obtained from the cross-sectional micrographs can be used for comparison. It is therefore possible that even fibre volume fractions larger than unity result from Eq. 6.10, if an uncoated or only thinly coated segment with a core diameter smaller than the mean core diameter is measured. These cases cannot be differentiated using this method. Nevertheless, both thin and thick uncoated segments may be filtered from the total distribution by comparing the seventieth percentile of the fibre volume fraction distribution of a given image with a limit value. This limit value is defined in Eq. 6.11 as the thought fibre volume fraction resulting from the measurement of an uncoated fibre with a thickness which corresponds to the upper limit of the standard range of all core diameters.

$$v_{f,\mathrm{lim}} = \left(\frac{\overline{d_c}}{\overline{d_c} + \sigma\left(d_c\right)} \right)^2 \tag{6.11}$$

In Eq. 6.11, $\sigma\left(d_c\right)$ denotes the standard deviation of all core diameters d_c. If the seventieth percentile of an image's distribution of fibre volume fractions exceeds this limit, the image is rejected. Otherwise, the entire distribution of the image is taken into account. The choice of the seventieth percentile to be compared to the threshold is arbitrary. For the presented data, it was found by random checks that this value best represents a compromise between filtering out most segments which appear to be uncoated and the expense of filtering out only a small portion of coated segments with a thin core. Note that the filtered total distribution of one specimen may therefore still contain values of fibre volume fraction greater than unity, especially if there is a large variation of the total coated diameter in a single image.

6.3.4 Results and discussion

Some representative scanning electron micrographs of coated filaments produced using different withdrawal velocities and a solution of 6.6 vol%

poly(ester-amide) in trichloromethane are shown in Fig. 6.12. All fibres

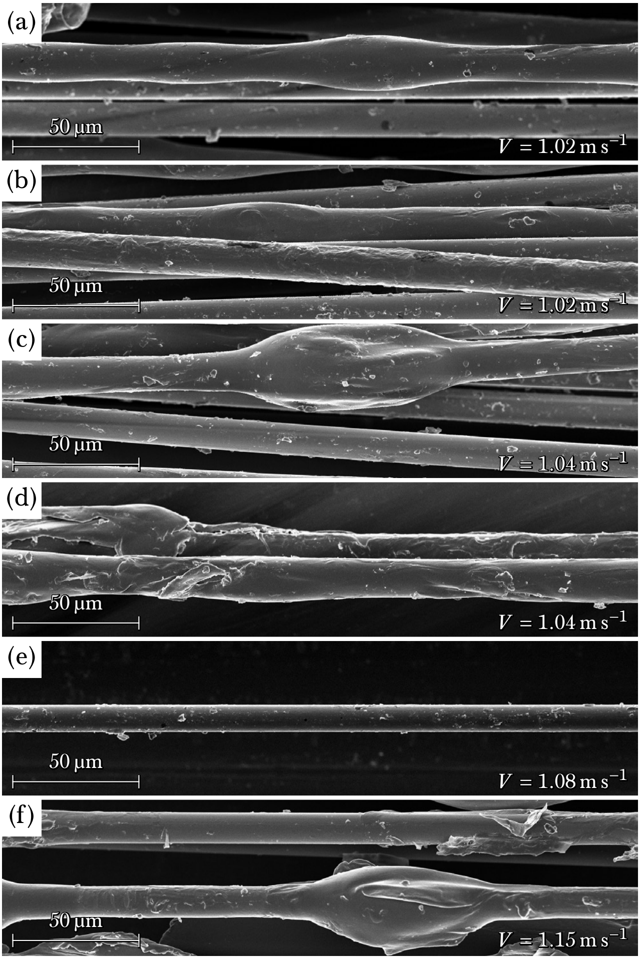
(a)
50 µm
V = 1.02 m s⁻¹
(b)
50 µm
V = 1.02 m s⁻¹
(c)
50 µm
V = 1.04 m s⁻¹
(d)
50 µm
V = 1.04 m s⁻¹
(e)
50 µm
V = 1.08 m s⁻¹
(f)
50 µm
V = 1.15 m s⁻¹

Figure 6.12: Scanning electron micrographs of glass/poly(ester-amide) bicomponent fibres showing the surface quality and thickness variation of the coatings along the fibre. All fibres were manufactured by withdrawing a glass monofilament from a bath containing 6.6 vol% poly(ester-amide) in trichloromethane at different speeds.

showed a relatively rough surface with different degrees of thickness variations. The specimens depicted in Fig. 6.12a and b show only small to medium sized undulations. The undulations captured in Fig. 6.12c, d, and f are more significant and exhibit geometries partly akin to dried droplets, while the fibre in Fig. 6.12e appears to have a uniform coating. The undulations are likely caused by Plateau-Rayleigh-type instabilities of the free surface flow during the coating process, which cause arbitrary ripples in the free surface to grow or shrink based on their periodicity along the fibre.[23,68] These instabilities result from the minimization of surface energies similar to the mechanisms that drive the formation of droplets in slow open jet flows, e.g. in a dripping faucet. It is hypothesized that the presence of the core filament and the rapid evaporation of the solvent in this system prevent the instabilities from forming droplets. The shrivelled appearance of the undulations is attributed to the drying process, as the outer surface of the coating solidifies first and the remaining solvent within diffuses through that layer, causing shrinkage underneath.[77] The presence and extent of the aforementioned undulations are not expected to be problematic for the further processing of bicomponent fibres into preforms or affect the final quality the consolidated components, because thermoforming methods will average out any uneven distribution of the matrix at these small scales.

For all tested fibres, the coatings produced by dip-coating entirely surround the glass filaments, leaving no dry spots on their surface, regardless of the undulations. Evidence of this is given by the cross-sectional images of the coated fibres. Fig. 6.13 provides a representative selection of such cross-sections. In addition to the thin layer of platinum which marks the interface between the coating and the surrounding epoxy, the coating material can be differentiated by its rougher texture after polishing. Most coatings seem to be in a roughly concentric arrangement, while a few cross-sections revealed assymmetric sheaths, as in Fig. 6.13b. Coatings with non-circular geometries, as shown in Fig. 6.13c and e most likely correspond to sections of the fibre where an undulation in the coating has shrivelled due to drying (Fig. 6.12f). The micrographs clearly show the interfaces between the circular glass core and the coatings, which shows that debonding occurs between the reinforcement and the matrix. This debonding is attributed to the mechanical stresses due to the swelling and subsequent shrinkage of the polymeric coating during the processing of the samples. Even though

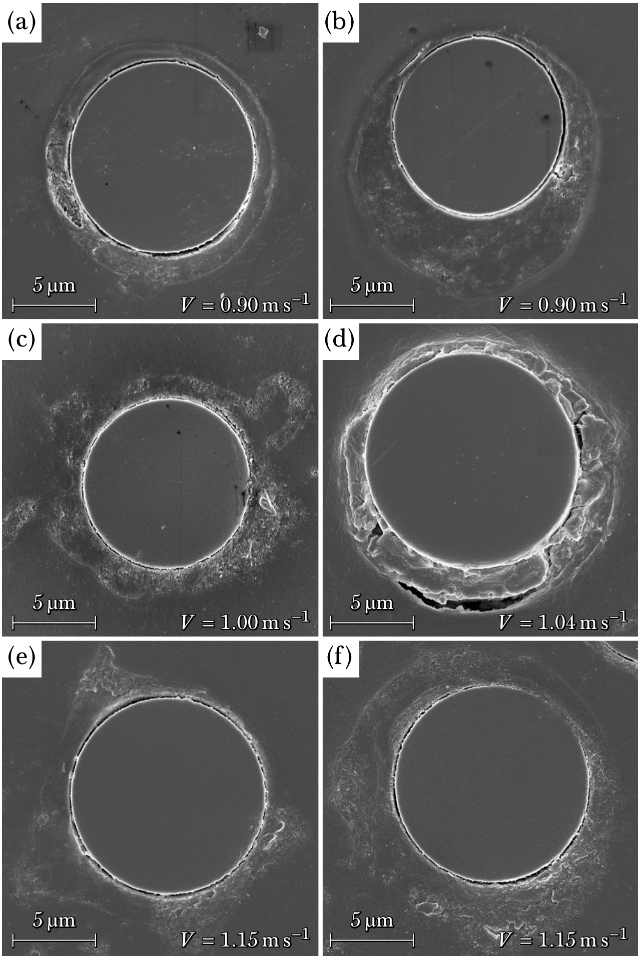
(a)
5 µm
$V = 0.90\,\mathrm{m\,s^{-1}}$
(b)
5 µm
$V = 0.90\,\mathrm{m\,s^{-1}}$
(c)
5 µm
$V = 1.00\,\mathrm{m\,s^{-1}}$
(d)
5 µm
$V = 1.04\,\mathrm{m\,s^{-1}}$
(e)
5 µm
$V = 1.15\,\mathrm{m\,s^{-1}}$
(f)
5 µm
$V = 1.15\,\mathrm{m\,s^{-1}}$

Figure 6.13:
Scanning electron micrographs of polished specimens of embedded glass/poly(ester-amide) bicomponent fibres showing the core-sheath arrangement of the two materials. All fibres were manufactured by withdrawing a glass monofilament from a bath containing 6.6 vol% poly(ester-amide) in trichloromethane at different speeds.

3-aminopropyltriethoxysilane was used as sizing on the glass filaments, this chemical may not be suitable for poly(ester-amide) or may have been dissolved away by the trichloromethane solvent.

The average thicknesses of the coatings were determined by measuring the widths of the coated fibres from transverse images like those shown in Fig. 6.12 and subtracting the widths of the glass cores. However, the process used by the material supplier to spin the glass filaments resulted in significant variations in fibre diameter between different filaments as well as along the roving's length which made accurate assessments of the coating thicknesses challenging. The variability of the glass fibre diameters can be seen in the cross-sectional images shown in Fig. 6.13. A quantitative analysis showed that glass fibre diameters ranging from 10.25 µm to 13.64 µm were measured across all samples giving a mean value of 12.16 µm and a standard deviation of 0.80 µm. Note that in the calculation of the coating thicknesses, a difference of 3 µm is highly significant. While the variability in fibre diameter over the roving was quite high, the variability was found to be significantly lower over short sections of a single filament such as the 2 m to 4 m lengths used in these experiments. For example, a 2 m long filament may vary in diameter from 11.98 µm to 12.36 µm and have a mean diameter of 12.20 µm and a standard deviation of 0.13 µm. For this reason, the average glass fibre diameter was individually measured and calculated for each specimen. For more detailed explanations on how the diameters of the glass fibres were measured, please refer to Appendix B.

Fig. 6.14 shows how the fiber volume fractions were calculated from SEM images (Fig. 6.14a) by showing a typical micrograph with its corresponding image data (Fig. 6.14b). The fibre shown here was withdrawn from the polymer solution at a velocity of $1.15\,\mathrm{m\,s^{-1}}$. The curve in Fig. 6.14c gives the total width of the coated fibre as a function of position. A histogram describing the probability distribution of fibre volume fractions is given in Fig. 6.14d. The particular section of dip-coated fibre shown here exhibits a bimodal distribution, meaning that the probability to find either a very thick coating or a very thin coating at any given position is high. This is expected for coatings which have regular undulations. For each coated specimen, between 18 and 45 fibre images were analysed to obtain a representative sample size. The distribution of fibre volume fractions calculated from the measurements of all images taken of this sample is shown in Fig. 6.15. The cumulative distribution indicates that a broad range of coating thicknesses are found

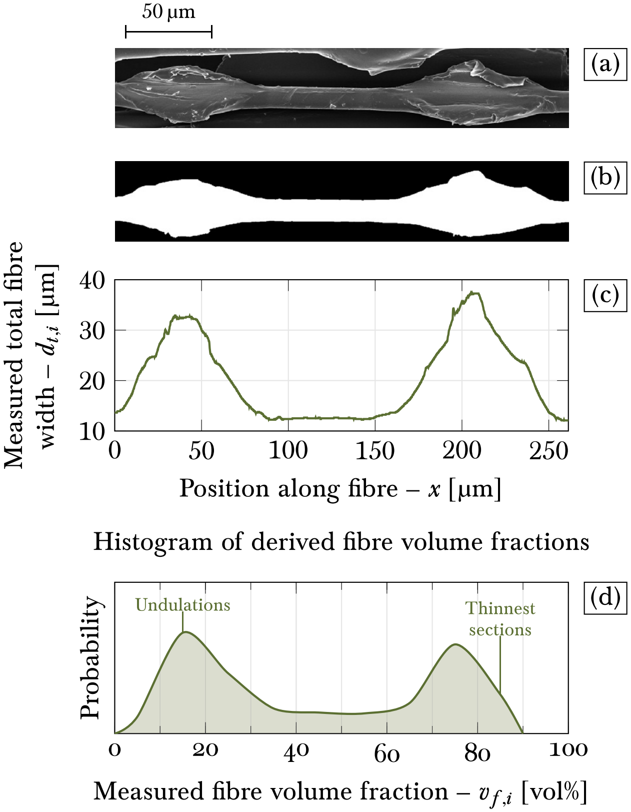

Figure 6.14: A representative scanning electron micrograph (a) with its processed binary image (b); the total fibre widths $d_{t,i}$ measured at position x along the fibre's length (c); and the distribution of fibre volume fractions $v_{f,i}$ calculated using this measurement and the mean core diameter of the entire sample (d) ($V = 1.15\,\mathrm{m\,s^{-1}}$).

along the length of the fibre, with a median fibre volume content of ~ 0.7.

The probability density functions of fibre volume fraction $v_{f,i}$ as a function of fibre velocity V are given in a violin plot in Fig. 6.16. The horizontal bars within the distributions represent the median values and

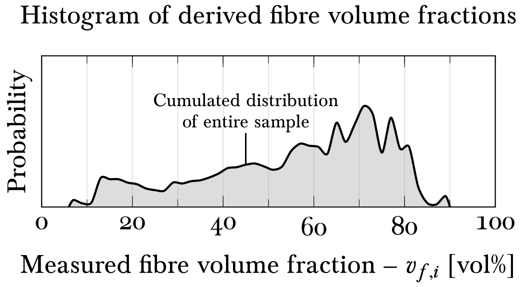

Figure 6.15: The distribution of fibre volume fractions $v_{f,i}$ derived from all images of the sample shown in Fig. 6.14 ($V = 1.15\,\mathrm{m\,s^{-1}}$).

the circular markers show the means. The shaded background indicates the range of desired fibre volume fractions which is considered in the theoretical study, with the dotted, solid, and dashed horizontal lines indicating fibre volume fractions of 30 %, 50 % and 70 %, respectively. Fig. 6.16 indicates that for the materials considered, dip-coating at withdrawal velocities greater than $1.04\,\mathrm{m\,s^{-1}}$ produces average coating thicknesses which yield fibre volume fractions in the range desired for structural composites. The shape of the probability density functions show that the coating is for the most part relatively thin along the length of the fibre but may be present in Fig. 6.16 show fibre volume fractions close to zero while others appear to be higher than unity. While the former is certainly possible, the latter is an artefact of the image analysis procedure used to derive these values. Because it is not possible to subtract the actual core diameter at every given point from the measured widths of the coated fibres, mean core diameters – which may be larger than the width of the coated fibre at a particular location – are used in the calculations. Extreme artefacts of this type are filtered out in the Fig. 6.16 are consistent with coatings that show undulations along the fibre length as discussed in Fig. 6.12 and 6.14.

Although the variation in coating thickness is high along the length of each bicomponent fibre, when these fibres are bundled in large numbers for use in a preform material, the variations are expected to even out statistically and are therefore not necessarily considered detrimental to the proposed preform architecture; the most important characteristic

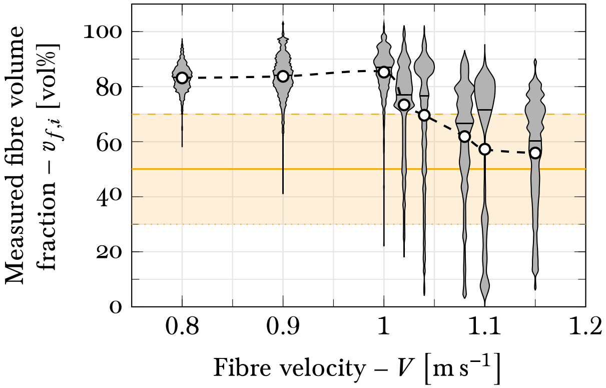

Figure 6.16: Probability density functions of measured final fibre volume fractions of bicomponent fibres withdrawn from a bath containing 6.6 vol% poly(ester-amide) in trichloromethane depending on the withdrawal velocity. The horizontal bars within the distributions show the median values and the markers connected by the dashed line represent the mean values. The shaded background highlights the range of desired fibre volume fractions.

for the hybrid bicomponent fibres is the average fibre volume content. Therefore, these experiments provide adequate proof that hybrid bicomponent fibres with fibre volume fractions which are suitable for the production of structural polymer composites can be manufactured via solution dip-coating.

6.4 Comparison of experimental and predicted results

The empirical results are compared to the theoretical models of De Ryck and Quéré and White and Tallmadge in Fig. 6.17. It is evident that the model of White & Tallmadge overestimates the fibre velocity window in which bicomponent fibres with a core volume fraction above 60 % can be produced by dip-coating given the selected material system. On the other hand, the prediction given by De Ryck & Quéré is on the same order of magnitude as the empirical results, overestimating the

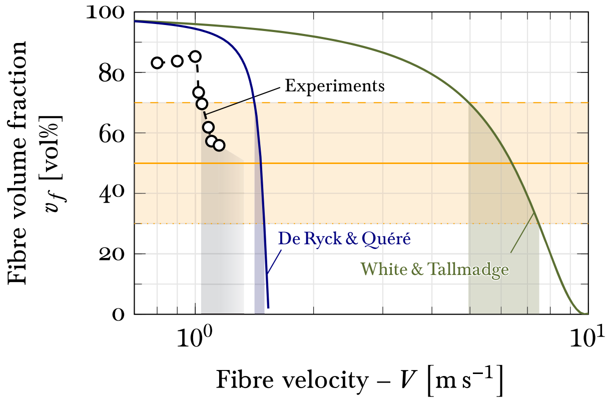

Figure 6.17: Comparison of the mean measured fibre volume fractions with the predictions given by the analytical models for a solution of 6.6 vol% poly(ester-amide) in trichloromethane. The shaded areas under the curves highlight the fibre velocity windows inside which each curve falls within the desired range of fibre volume fractions.

fibre velocity V with an offset between ~0.3 m s^{-1} and 0.4 m s^{-1}. This is a reasonably accurate prediction, considering the large spread in the empirical data and the fact that the analytical model does not account for flow instabilities.

It was not possible to obtain samples with mean fibre volume fractions below 0.5 using the current experimental setup. It can therefore be concluded that an overlap of the two processes is possible, with a range of fibre speeds between ~0.38 m s^{-1} and 1.15 m s^{-1}, limited on the lower end by the achievable speed at which glass fibres thinner than 20 µm can still be spun and on the upper end by the dip-coating process when considering solutions of poly(ester-amide) in trichloromethane.

6.5 Conclusion

For the first time, a theoretical study has shown that it is possible to fabricate hybrid bicomponent fibres by dip-coating newly spun glass fibres in-line with a polymeric solution. This finding is supported by empirical data of the dip-coating process, which validates the approximation of the coating thickness on the filaments given by the theory of De Ryck & Quéré.[67,72]

The experimental study has proven that it is possible to fabricate hybrid bicomponent fibres via dip-coating in a polymer solution and that coating thicknesses can be achieved which are useful for further processing of these fibres into composite structures. The samples produced exhibit irregular coating thicknesses at the microscale, which is however not considered problematic for further processing of preforms made from such bicomponent fibres.[23] In addition, the withdrawal velocities used for the experiments show an overlap with the fibre velocities of glass fibre spinning, proving that dip-coating can be used in-line with the glass fibre formation process for the purposes of efficiently fabricating bicomponent fibre rovings.

The theoretical study and experiments were conducted based on glass fibre diameters of 15 µm and 12 µm, respectively. However, hybrid bicomponent fibres based on smaller glass fibre diameters would lead to stronger composites. Therefore, further work should be invested in improving the coating process to work at higher velocities and a more in-depth study on the scalability of the presented fabrication method is required to ascertain the economic viability of bicomponent fibre fabrication. In particular, the coating of many filaments in parallel as part of a direct roving process and the use of alternative coating materials should be addressed.

By demonstrating the feasibility of hybrid bicomponent fibre production and identifying the challenges associated with the process used, this work advances the state-of-the-art for this novel form of thermoplastic preform and moves the novel preform architecture closer to reality.

7

DIP-COATING IN A NANOFILLED HOT MELT

This chapter investigates a potential alternative to solvents for the purposes of reducing the viscosity of the coating fluid. Nanoparticles, when used in minute concentrations, have been observed to reduce the viscosities of polymer melts in a manner that contradicts Einstein's equation for the viscosity of suspensions. This study investigates if and to what extent the effect of this viscosity-reducing phenomenon can be exploited in the processing of molten thermoplastic polymers and focuses on the application in dip-coating of glass fibres. Silica nanoparticles were dispersed in poly(ester-amide) using different solvent mixtures and the effects of the nanoparticle-fillers on the rheology of the polymer melts were investigated. Subsequently, the nanoparticle-filled melts were used in a dip-coating process to study how the non-Einsteinian decrease in viscosity could be used to modify the processing parameters of the melt-based process. Results indicate that reducing the viscosity of a polymer melt using nanoparticle-fillers has the potential to reduce processing time and costs in flow-dependent melt-based manufacturing processes.

7.1 Viscosity reduction through nanofilling

Low concentrations of nanoparticles have repeatedly been reported to decrease the viscosity of polymer melts in comparison to the neat polymer. Mackay et al. first reported viscosity reductions of up to 80 %

in linear polystyrene melt when blended with cross-linked polystyrene nanoparticles.[78–80] Jain et al. reproduced the effect in isotactic polpropylene filled with silica particles and reported decreases of up to 90 % in melt viscosity.[81] These experimental observations deviate from the intuitive hypothesis of Einstein's equation[82] (shown in Eq. 7.1), which suggests that the viscosity η of a slurry should only increase with filler concentration.[82–84]

$$\frac{\eta}{\eta_l} = 1 + k_E\varphi + \mathcal{O}\left(\varphi^2\right) \tag{7.1}$$

In Eq. 7.1, η_l denotes the pure liquid's viscosity, φ is the particle volume fraction, k_E is the Einstein coefficient, which is 2.5 for spherical particles, and $\mathcal{O}\left(\varphi^2\right)$ denotes terms of higher order. The graph in Fig. 7.1 illustrates the discrepancies between the effects of low concentrations of nanoparticles on the relative viscosities predicted by Einstein's equation and reported experimental values.[78–81] The experimentally observed decreases in viscosity have been attributed to excluded free volume around the nanoparticles[78,79] and selective adsorption of high molar mass polymer chains on the surface of the nanoparticles which lead to a reduction in entanglement density.[81,85] However, the exact mechanisms by which the effect occurs has yet to be proven.

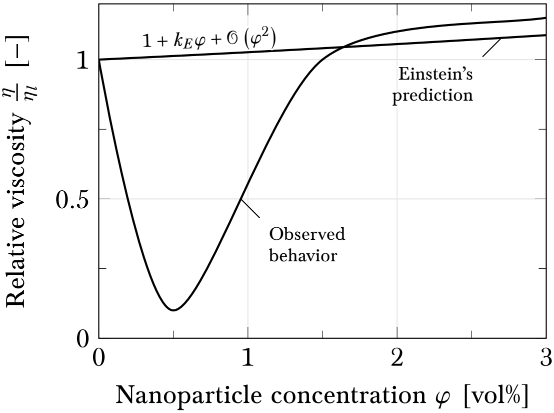

Figure 7.1: Qualitative comparison between the relative viscosity of a suspension as a function of nanoparticle concentration as predicted by Einstein's equation and as observed experimentally.

Although the nanoparticle-induced reductions in viscosity have been reported to be reproducible, the potential application of the phenomenon to manufacturing processes has not yet been investigated. It stands to reason that many manufacturing processes would benefit from reduced melt viscosities, especially those involving the flow of thermoplastic polymers such as injection moulding and liquid coating. Not only would lower viscosities reduce processing times, they may also reduce the pressures and temperature required for a process.[86] Thus, nanoparticle-induced viscosity reductions may offer potential cost and energy savings in thermoplastic polymer melt-based processes.

Here, a first investigation of the effects of nanoparticle-induced viscosity reductions in a melt-based process, namely that of dip-coating of a fibre in a thermoplastic melt is presented. Lowering the viscosity of the dip-coating would allow coatings of a given thickness to be processed at higher line speeds thereby facilitating high volume production. Demonstrating any advantages due to nanoparticle-fillers in dip-coating may lead to applications in other melt-based processes. Poly(ester-amide) (PEA), an aliphatic segmented block co-polymer with semi-crystalline thermoplastic behaviour,[73] was selected for these studies because of its relatively low melt viscosity and low melting temperature (< 130 °C). Silica nanoparticles were dispersed using solution casting to see if already the low melt viscosity of PEA could be further reduced. The PEA-silica nanoparticle compounds were then used in a dip-coating process to study their effects on thickness of the coated layers. Finally, a discussion on the potential of exploiting nanoparticle-induced viscosity reduction in dip-coating processes to reduce costs and increase throughput is presented.

7.2 Experiments

7.2.1 Sample preparation

Different concentrations of spherical, porous silica nanoparticles (99.5 %, 637246, Sigma-Aldrich) were suspended in ethanol (EtOH) (EMSURE® 100983, Merck Millipore) and sonicated at 37 kHz in an Elma Elmasonic S30H ultrasonic bath until homogeneous. 1-decanol ($C_{10}H_{22}O$) (≥ 98 %, 150584, Aldrich) and trichloromethane ($CHCl_3$) (≥ 99.8 %, ReagentPlus® 132950, Sigma-Aldrich) were successively added and sonicated until homogeneous. Afterwards, pellets of PEA (Dow Europe GmbH) were dissolved in the suspension at a concentration of $\sim 10\,\mathrm{wt\%}$ while swirling the mixture with a Scientific Industries Inc. Vortex-Genie 2 until homogeneous. The samples were then solution cast by heating the mixtures to 100 °C for 3 h under stirring on a Heidolph MR 3002 magnetic stirring hotplate. Finally, the samples were dried overnight at 60 °C and under vacuum in a SalvisLab Vacucenter VC20 vacuum drying oven to remove residual solvents.

Samples were cast using different ratios of solvents and with final particle concentrations in the polymer ranging from 0 wt% to 1.0 wt% in increments of 0.2 wt%.

7.2.2 Thermal analysis

The pure PEA pellets exhibit a peak melt temperature T_{pm} of 128.8 °C (Differential scanning calorimetry, DIN EN ISO 11357-3, N_2-atmosphere, $10\,\mathrm{K\,min^{-1}}$, Mettler-Toledo DSC 1) and an onset of degradation temperature T_A of 370 °C (Thermogravimetric analysis, DIN EN ISO 11358-1, O_2-atmosphere, $30\,\mathrm{K\,min^{-1}}$, Perkin Elmer Pyris 1).

7.2.3 Rheology

The flow behaviour of the melted specimens was characterized in N_2-atmosphere using an Anton-Paar MCR-302 rotational rheometer with a cone-plate geometry (30 mm, 4°). The measuring chamber was kept at 150 °C throughout all measurements. For each specimen, three flow curves spanning shear rates of $1\,\mathrm{s^{-1}}$ to $100\,\mathrm{s^{-1}}$ were obtained from each of three separate loadings of each sample.

7.2.4 Surface tension

The surface tensions of the pure and nanoparticle-filled polymer melts were measured using the pendant drop method on a Krüss DSA100 drop shape analyser in air and at a temperature of 150 °C. The samples were extruded from a heated cannula with a 2 mm wide cylindrical tip, which was suspended into a temperature-controlled chamber with glass windows for observation. The polymer melt was incrementally pushed downwards in the cannula, waiting for the formation of a stable droplet hanging from the tip in an equilibrium state. Three loadings per sample were characterized by imaging fifteen or more droplets.

7.2.5 Dip-coating

Single E-glass fibres of finite lengths ($< 3\,\mathrm{m}$) and a mean diameter of $12\,\mu\mathrm{m}$ were separated from a roving containing 204 filaments sized with 1 wt% 3-aminopropyltriethoxy silane (APTES). Individual filaments were successively passed through a bath of the sample compound heated to 150 °C and withdrawn vertically at constant velocities in the range of $0.25\,\mathrm{m\,s^{-1}}$ to $1\,\mathrm{m\,s^{-1}}$ by a winder at a distance of $\sim 0.12\,\mathrm{m}$ to the bath (Fig. 7.2).

7.2.6 Imaging

To qualitatively gauge the dispersion of nanoparticles in the solvent mixture, drops of different samples containing the same concentration of particles suspended in different solvent mixtures were cast onto sample holders and imaged in a Zeiss LEO 1530 (Gemini column) scanning electron microscope (SEM). The resulting micrographs were analysed in ImageJ to determine the size distribution of the particle agglomerates. Image segmentation was used to separate the aggregates from the background, then their shapes were identified using edge detection and finally the individual size of every aggregate was extracted as the mean diameter when measured over the centroid of its area and at all angles.

To obtain cross-sectional images of the coated monofilaments, some of them were sputtered with 10 nm of platinum in a Safematic CCU-010 coating unit, embedded in epoxy (Struers SpeciFix-20), and sanded and polished in a Struers Abramin lapping machine to reveal their cross-sections. The polished cross-sectional specimens were again sputtered with 10 nm of platinum to provide a conductive surface. Images of transverse fibres were obtained by laying the fibres flat on a SEM sample holder and coating them with 10 nm of platinum. The diameters of the coated fibres $D_{p,i}$ were obtained from the transverse micrographs. The diameters of the glass cores $D_{c,j}$ were measured by fitting ellipses to the cross-sectional micrographs.[*] Finally, the distributions of coating

---

[*] Note that the minor axis yields the diameter $D_{c,j}$, since the observed cross-section may not be perfectly perpendicular to the filament axis.

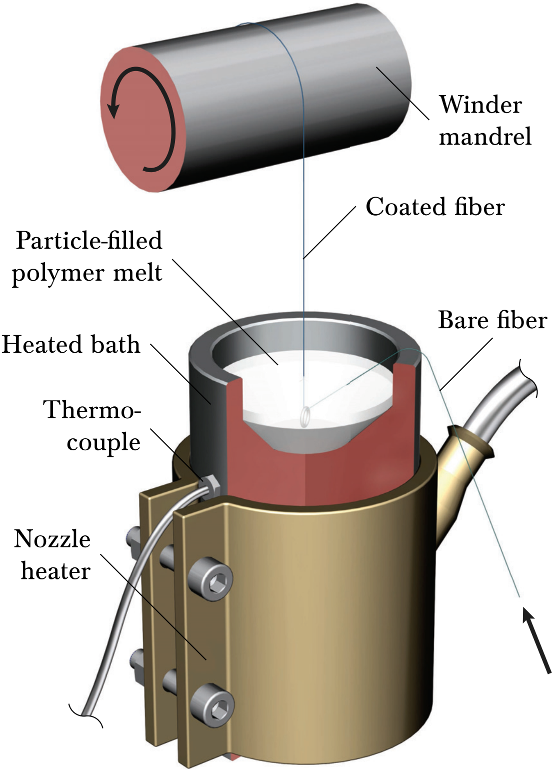
Winder mandrel
Coated fiber
Particle-filled polymer melt
Bare fiber
Heated bath
Thermo-couple
Nozzle heater

Figure 7.2: Illustration of the setup used to dip-coat glass monofilaments with a nanofilled thermoplastic polymer melt.

thicknesses h_i of each specimen were obtained by subtracting the mean core diameter of the specimen $\overline{D_c}$ from the respective total diameter $D_{p,i}$, as is shown in Eq. 7.2.

$$h_i = \frac{D_{p,i} - \overline{D_c}}{2} \tag{7.2}$$

The image processing method used to determine the coating thicknesses is equivalent to the one presented in section 6.3.3, p. 62.

7.3 Results and discussion

7.3.1 Observation of non-Einsteinian decrease in viscosity

The viscosity drop that can be induced by nanoparticles in a polymer melt has been observed to be dependent on the size, shape, concentration, surface energy, and dispersion quality of the particles,[81] and therefore it is important to characterize the silica nanoparticle dispersions used in these experiments. The silica nanoparticles exhibited an average primary particle size of ~ 24 nm and were sphere-like in shape as shown in Fig. 7.3a. However, these silica nanoparticles tended to agglomerate, particularly in nonpolar dispersing media – due to the likely formation of polar hydroxyl groups on the silica surface[87] – which made it difficult to obtain stable dispersions of silica nanoparticles in tricholoromethane, the preferred but nonpolar solvent for poly(esteramide) (PEA).

To increase the stability of the silica nanoparticle suspensions in the nonpolar trichloromethane, ethanol (EtOH) and 1-decanol ($C_{10}H_{22}O$) were added in varying amounts to increase the polarity of the solution and act as a surfactant, respectively. The different solvent mixtures tested are summarized in Table 7.1. Although the use of these solvent mixtures did not entirely prevent the formation of agglomerates as shown in Fig. 7.3b, the dispersibility of the nanoparticles was visibly improved.

Table 7.1: Compositions of dispersing media tested to produce silica suspensions.

Sample №	EtOH	$C_{10}H_{22}O$	$CHCl_3$
1	-	-	100 vol%
2	50 vol%	-	50 vol%
3	-	10 vol%	90 vol%
4	50 vol%	5 vol%	45 vol%

The effect that the different compositions of dispersing media had on the agglomeration size distribution of the silica nanoparticles after drop-casting is illustrated in Fig. 7.4. The distributions show that the mixtures had a significant effect on the dispersibility of the nanoparticles: replacing 50 % of the nonpolar trichloromethane with ethanol allowed

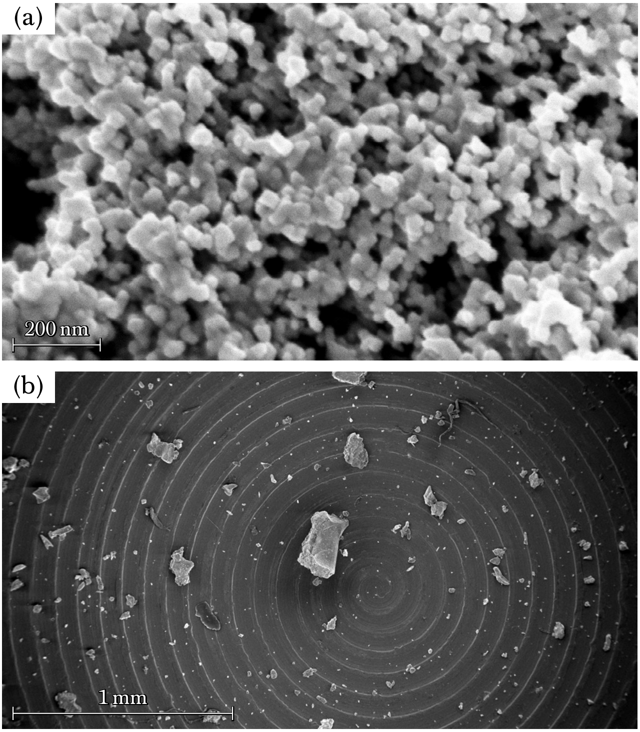

Figure 7.3: Scanning electron micrographs of a) silica nanoparticles showing primary particle sizes of ~ 24 nm; and b) aggregates of silica nanoparticles after suspension in a solvent mixture of 50 vol% EtOH and 50 vol% $CHCl_3$ and drop-casting onto a machined sample holder.

the silica to form a dispersion, while the addition of 1-decanol as a surfactant clearly improves the dispersion of the particles, resulting in smaller agglomerates as indicated by the higher frequency of particles at the lower end of the agglomerate size scale. Combining ethanol and 1-deconal with the trichloromethane resulted in the smallest average agglomerate size.

The rheology of different particle-filled PEA materials were measured to investigate if, and to what extent, viscosity reductions could be observed in the materials produced using different dispersing media

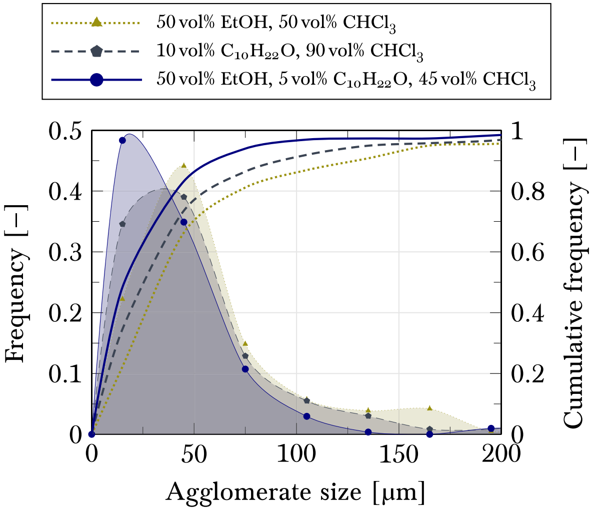

Figure 7.4: Distribution curves of aggregate sizes of drop-cast silica nanoparticles previously dispersed in △) 50 vol% EtOH and 50 vol% $CHCl_3$; ⬠) 10 vol% $C_{10}H_{22}O$ and 90 vol% $CHCl_3$; and ○) 50 vol% EtOH, 5 vol% $C_{10}H_{22}O$, and 45 vol% $CHCl_3$.

mixtures and at different particle loadings. Representative flow curves obtained from the samples of filled and unfilled PEA polymer melts are provided in Fig. 7.5. The flow curves were all fitted with the power law as given in Eq. 7.3, where η denotes the dynamic viscosity, K is the consistency index, $\dot{\gamma}$ is the shear rate, and n the power law exponent. For Newtonian fluids, $n = 1$ and thus η is independent of $\dot{\gamma}$. All the samples measured under rotational rheometry expressed Newtonian behaviour with a slight trend towards shear-thinning, i.e. $n \approx 0.99$.

$$\eta = K\dot{\gamma}^{n-1} \tag{7.3}$$

The consistency index K, which provides the dynamic viscosity at a shear rate of $1\,s^{-1}$, was used to compare the different samples. The fitted K values were normalized to the average K_l value calculated for the pure polymer processed using the same solvent mixture. The average K_l values measured are provided in Table 7.2. The variation between these

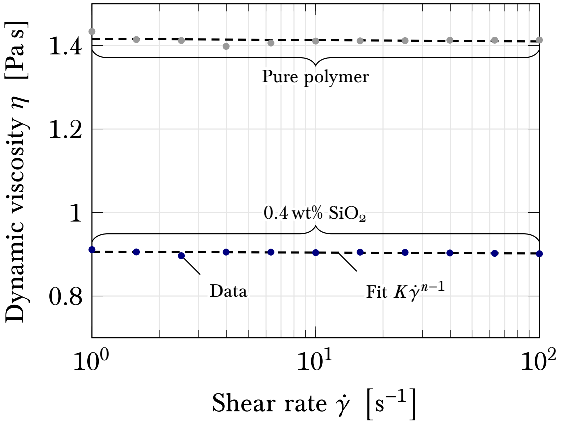

Figure 7.5: Representative measured flow curves of samples created using 50 vol% EtOH, 5 vol% $C_{10}H_{22}O$, and 45 vol% $CHCl_3$, for an unfilled sample and for a sample filled with 0.4 wt% SiO_2 nanoparticles, with their corresponding power law fits.

Table 7.2: Average consistency indices of the pure (unfilled) polymer K_l after processing with the different dispersing media mixtures.

Composition of dispersing media	K_l (avg.)
100 vol% $CHCl_3$	2.88 Pa s^n
10 vol% $C_{10}H_{22}O$, 90 vol% $CHCl_3$	0.94 Pa s^n
50 vol% EtOH, 5 vol% $C_{10}H_{22}O$, 45 vol% $CHCl_3$	1.40 Pa s^n

values is attributed to the varied use of 1-decanol, some of which seems to have remained in the polymer after solvent evaporation and subsequently influenced the rheometrical measurements. It is for this reason that the consistency indices were normalized with respect to the average value of the unfilled polymer processed in the same dispersing media mixture. Fig. 7.6 shows the effect of nanoparticle concentration φ_{SiO_2} on the relative viscosity of the PEA melt as quantified by the normalized consistency index for three different dispersing media compositions. The thick lines and shaded areas denote interpolations of the mean values and standard deviations at each concentration level. The black line indicates the theoretical increase in viscosity as predicted by Einstein's equation for the viscosity of suspensions as applied using a second order polynomial with the coefficients found by Guth and Simha[84] as shown in Eq. 7.4.

$$\frac{\eta}{\eta_l} = 1 + 2.5\varphi + 14.1\varphi^2 \tag{7.4}$$

Nanoparticle-induced viscosity reductions were observed in both samples which contained the surfactant 1-decanol in the solvent mixture, whereas the specimens produced solely with trichloromethane exhibited an increase in viscosity much greater than that predicted by the Einstein equation. The latter behaviour is commonly reported in systems that contain aggregated particles[88] and confirms our observations that the silica particles did not disperse well in trichloromethane. The large scatter of the samples containing 1-decanol but no ethanol suggests

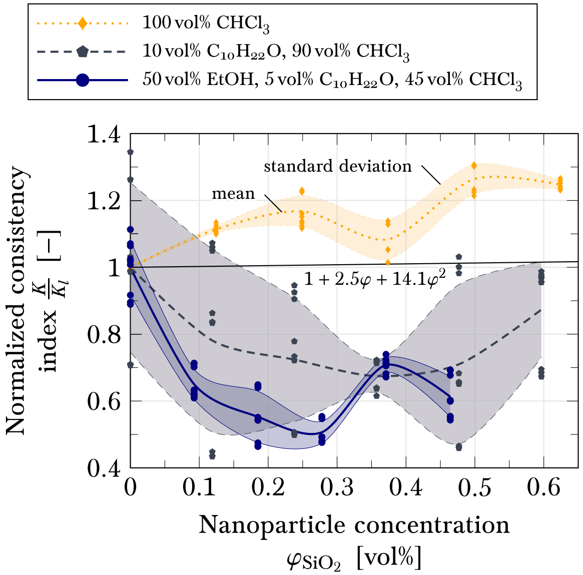

Figure 7.6: Normalized consistency indices of nanofilled poly(ester-amide) melt versus particle concentration for samples prepared using different ratios of solvents and surfactant. For each sample, normalization is done against the pure polymer, respectively. The black line represents the prediction by Einstein's equation for spherical particles.

that the solution was not entirely stable or homogeneous. The largest viscosity reduction effect was measured to be around 49 % (cubic Bézier interpolation) and was produced using a solvent and surfactant mixture of 50 vol% ethanol, 5 vol% 1-decanol and 45 vol% trichloromethane and a nanoparticle volume fraction φ_{SiO_2} between 0.19 vol% and 0.28 vol% (corresponding to a weight fraction between 0.4 wt% and 0.6 wt%).

In comparison to viscosity reductions reported in previous studies,[78–81] the maximum viscosity reduction of 49 % obtained here is moderate, but was achieved using a straightforward and easy-to-use approach. It is expected that methods like the in-situ synthesis of the particles as used by Jain et al.[85] or an optimization of particle size with respect to the molecular weight of the polymer would yield a greater effect. Nevertheless, a reduction of viscosity by a factor of two is sufficient to investigate its influence on the coating process.

7.3.2 Dip-coating of fibres

While nanoparticle-induced viscosity reductions are desired effects of adding the fillers to the thermoplastic melt, the particles may interact with the free surface of the polymer and inadvertently modify the effective surface energy of the polymer melt. Any effects that nanoparticles have on the surface tension of the polymer melt would influence the capillary number of the system as described in Eq. 6.4. Many studies have been dedicated to characterizing the behaviour of particles at fluid-fluid interfaces.[89,90] Most relevant to the work here are those that have demonstrated that under energetically favourable conditions particles may adsorb irreversibly to an interface.[91,92] However, these studies tend to use high concentrations of particles ($\gg$ 10 vol%) which jam together to stabilize an interface. Low concentrations of particles ($<$ 1 vol%) have not been reported to significantly influence the effective surface tensions under pendant drop measurements. The surface tension measurements done on pure and 0.23 vol% $\mathrm{SiO_2}$ in PEA, as plotted in Fig. 7.7, are consistent with these earlier findings. No measurable difference between the surface tension of the pure PEA melt and that of the melt containing a low concentration of silica was found (Cohen's $d = 0.019$). Thus, according to Eq. 6.4, the viscosity of the melted sample is the only material parameter in the dip-coating process that is expected to be significantly influenced by the incorporation of the dispersed nanoparticles. Thus, according to Eq. 6.4, thermoplastic melts containing dispersed nanopar-

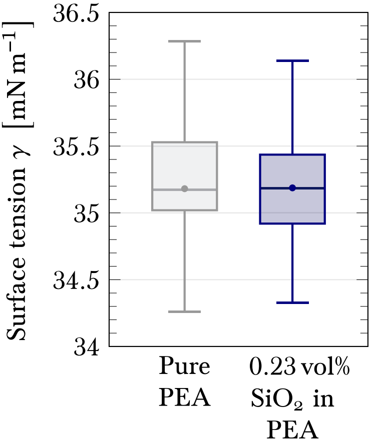

Figure 7.7: Comparison of surface tension measurements for the pure polymer and a nanoparticle concentration of 0.23 vol%.

ticles in concentrations conducive to induced viscosity reduction would yield thinner coatings than pure thermoplastic melts under the same processing conditions of withdrawal speed and fibre radius. Similarly, the reverse implication can be argued; nanoparticle-induced viscosity reductions can be exploited to increase the throughput of dip-coated fibres possessing coatings of a fixed thickness.

To quantify the effects of the nanoparticle-induced viscosity reduction on the dip-coating process, glass monofilaments were drawn through melts of pure PEA and through PEA melts containing suspensions of 0.23 vol% SiO_2. The micrographs in Fig. 7.8 show the bare glass fibres used alongside some of the results of the dip-coating process. The undulating structure of the coatings is attributed to the interplay between Plateau-Rayleigh-type instabilities in the column of polymer melt withdrawn vertically by the moving fibre substrate[68] and the solidification of the polymer as it cools down.

While the presence of low concentrations of nanoparticles do not alter the surface tension of the polymer, it seemed to have an noticeable effect on the expression of the Plateau-Rayleigh-type instabilities of the coatings. In comparison to the coatings made using the pure polymer shown in Fig. 7.8b, coatings made from the nanoparticle-filled PEA melt

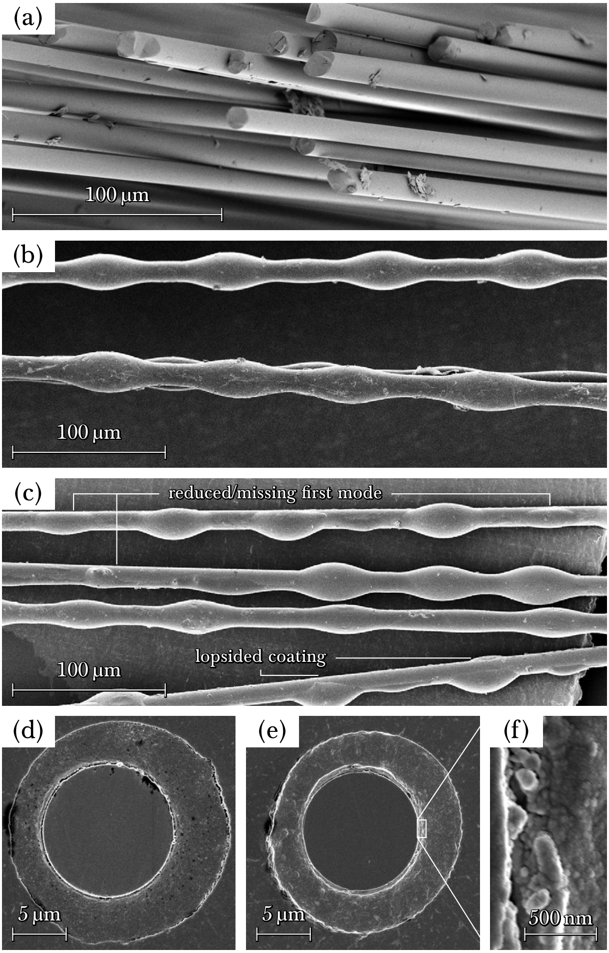
(a)
100 µm
(b)
100 µm
(c)
reduced/missing first mode
lopsided coating
100 µm
(d)
5 µm
(e)
5 µm
(f)
500 nm

Figure 7.8:

Micrographs of a) bare and b–f) dip-coated glass fibres. Images show transversal views of the dip-coated fibres made using b) pure PEA and c) 0.23 vol% SiO_2 in PEA at 0.5 mm s^{-1}, as well as cross-sectional views of dip-coated fibres made using d) pure PEA and e, f) 0.23 vol% SiO_2 in PEA at 1 mm s^{-1}. f) High magnification image showing the rough topology of the coating containing crystalline phases of PEA.

tended to exhibit more irregular spacing and variations in amplitude as shown in Fig. 7.8c. Examples of these irregularities which include smaller or missing nodules and lopsided coatings are indicated and labelled in Fig. 7.8c. These irregularities may be caused by the presence of agglomerates at the surface, which may locally hinder or slow down the development of the dominant modes or provide nucleating surfaces for the crystalline regions of PEA to preferentially deposit on as suggested by Fig. 7.8f.

Notwithstanding the effects of the Plateau-Rayleigh instabilities and the undulated structure of the coatings, the amount of material deposited in the dip-coating of the fibres using the pure and particle-containing melts could be compared by extracting the mean film thicknesses from the micrographs. The measured distributions are plotted against the velocity at which the fibres were withdrawn from the polymer melt in Fig. 7.9. The mean values are marked by filled circles and the lines within the boxes represent the median. The shaded boxes indicate the first to third quartiles. The lower and upper whiskers represent the minimum and maximum values within 1.5 times the interquartile-distance from the boxes, respectively. The large scatter of the data stems mainly from the previously described undulating coating thicknesses. However, there is still an identifiable trend of thinner coatings for the nanofilled polymer, as shown in the plot and by the calculated effect sizes d listed in Table 7.3.

Table 7.3: Mean coating thicknesses $\bar{h}$, corresponding standard deviations s and effect sizes d for the influence of nanofilling on the coating thickness in dip-coating.

V	$\bar{h}\,(s^*)$ [µm]		d^{**}
$[\mathrm{mm\,s^{-1}}]$	Pure PEA	0.23 vol% SiO_2	[–]
0.25	1.37 (1.75)	0.71 (0.61)	−0.50
0.50	3.10 (0.65)	1.30 (1.07)	−2.03
0.75	3.68 (1.34)	2.22 (1.96)	−0.87
1.00	3.97 (2.62)	3.11 (3.20)	−0.29

$^*s$ denotes the standard deviation.

$^{**}d$ denotes the effect size according to Cohen's d.

The theoretical coating thicknesses as predicted by the Landau,

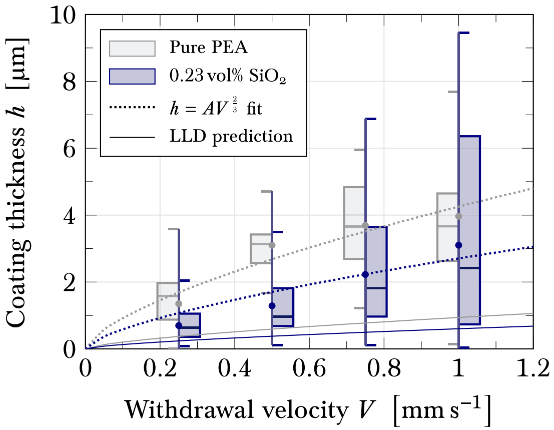

Figure 7.9: Measured coating thicknesses h versus withdrawal velocity V for the pure polymer and a nanoparticle concentration of 0.23 vol% compared to the predictions of the Landau, Levich, and Derjaguin model. Dashed lines represent power law fits as in Eq. 7.5.

Levich, and Derjaguin model as previously given in Eq. 6.4 are also plotted in Fig. 7.9 as a function of withdrawal velocity for the pure PEA melt and the 0.23 vol% SiO_2 in PEA melt based on the measured experimental data for ρ, η, and γ. However, the experimentally measured mean coating thicknesses were found to be greater than those predicted by the model by a factor of ~ 4.5. This large discrepancy may be attributed to the fact that the Landau, Levich, and Derjaguin model does not take into account the effects of Plateau-Rayleigh instabilities, the presence of a dispersed phase, the effects of crystallization and solidification, or the behavior of residual soluble surfactants.[93] Nonetheless, the experimental results could be fitted with a power law relationship, similar to that of the Landau, Levich, and Derjaguin model, of the form given in Eq. 7.5, where A is a fitting parameter.

$$h = \mathrm{A}V^{\frac{2}{3}} \tag{7.5}$$

The calculated fitting parameters A are given in Table 7.4, together with the measured mean dynamic viscosity η at a strain rate of $1\,\mathrm{s}^{-1}$ (as given by the consistency index K) and mean surface tensions γ for the pure polymer melt and for the one filled with 0.23 vol% silica nanoparticles.

Table 7.4: Summary of measured data for dip-coating of fibres from the pure and the sparsely nanofilled polymer melt.

	Pure PEA	0.23 vol% SiO_2
A $\left[m^{1/3}\,s^{2/3}\right]$	4.254×10^{-4}	2.705×10^{-4}
η^* [Pa s]	1.405	0.722
γ $\left[mN\,m^{-1}\right]$	35.181	35.187

*mean value at a strain rate $\dot{\gamma}$ of $1\,s^{-1}$.

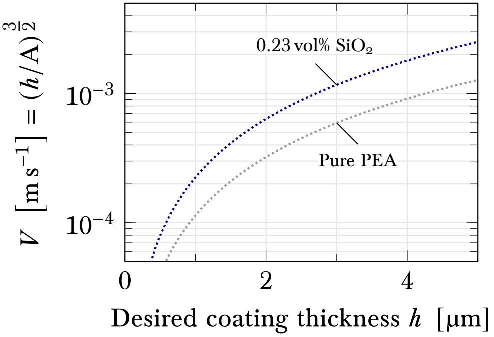

Figure 7.10: Comparison of withdrawal velocities required to yield a desired coating thickness for the pure and the sparsely nanofilled polymer melt.

The implications of nanoparticle-induced viscosity reductions to dip-coating processes are evident when the axes of Fig. 7.9 are exchanged so that the suggested withdrawal rate V is plotted as a function of the desired coating thickness h as shown in Fig. 7.10. For example, in the nanofilled systems studied here, a desired coating thickness of 2 µm can be produced at a speed of $6.4 \times 10^{-4}\,m\,s^{-1}$ instead of at a speed by $3.2 \times 10^{-4}\,m\,s^{-1}$, representing a increase by a factor of 2 by simply exploiting the viscosity reducing effects of nanoparticles in the polymer melts. In industrial processes, this potential to increase throughput may represent substantial energy savings and increases in profitability.

7.4 Conclusion

It is demonstrated that the nanoparticle-induced viscosity reductions observed when small concentrations of particles are dispersed in a thermoplastic polymer can be exploited to modify and improve the parameters of melt-based processes, for example to increase speed and throughput. The presented study focuses on the dip-coating of fibres and shows that the dispersed particles have no significant effect on the surface tension of the melt, essentially allowing the melt viscosity of the particle-laden polymer to be tuned independently from other fluid properties by varying the filler concentration. Similarly, the mechanical properties of the polymer in its solid form can be assumed to remain unaffected by the sparse concentration of particles. The results of these dip-coating studies are promising evidence that nanoparticle-induced viscosity reductions may also be exploited in other melt-based flow processes such as injection moulding where lower viscosities would be beneficial. Further investigation is required to address the scalability and robustness of improved particle dispersion techniques, such as the one reported by Jain et al.,[81,85] and to ascertain the potential benefits for coating and moulding processes involving polymer melts at an industrial scale.

7.4.1 Potential for the fabrication of bicomponent fibres

While the benefits of viscosity reduction outlined above can potentially be exploited for a variety of general processes, the level of reduction achieved both within the present study (factor of two) and in other reports (factor of ten)[81] do not compare with the range provided by solvents. The solution dip-coating study presented in chapter 6 has shown that much lower values of viscosity are required to coat glass fibres in-line during melt spinning. However, sparsely nanofilled thermoplastic melts could still provide an extended processing window for the production of bicomponent fibres (BCF) based on slower fibre production processes. A prime example is the fabrication of carbon fibre. If it were proven that graphitization and carbonization are feasible with geometrically separate monofilaments rather than spread rovings, a hot-melt dip-coating stage could be attached to the process chain.

Not only would this method yield BCF with a core that is stiffer and stronger, yet lighter than glass, but it would open BCF production to a wider range of polymers due to the fact that the requirements on their solubility vanish.

Within the remainder of this work, melt-based coating is not followed any longer, but it is concluded that nanofilled melts could be of benefit for future developments in BCF fabrication. The following chapters keep glass melt spinning as the base method and continue to investigate solution-based coating as a pilot process.

8

SOLUTION KISS-ROLL COATING

As shown in chapter 6, experiments with solution dip-coating have yielded fibre volume fractions as low as 56 % with a complete wet-out. However, the theoretical study concluded that due to the large dependence of the deposited coating thickness on the fibre velocity, there is only a very limited range of processing speeds for this coating process in-line with the formation of thin glass fibres with a diameter in the range of 10 µm to 20 µm. Lower velocities would yield thicker core filaments and higher velocities would result in thicker coatings, meaning fibre volume fractions too low for structural applications. It is therefore essential to find a method of fabricating hybrid bicomponent fibres which is more flexible in its processing window while maintaining a robust output if this preform technology is to aid the progression of lightweight fibre-reinforced polymer components into higher volume markets.

This chapter proposes an improvement on the dip-coating method which still follows the in-line implementation into the glass fibre spinning process by running the newly spun glass filament over a rotating roll which is partially immersed in a polymeric solution bath. Because the filament is only in contact with the roll over a short distance, this method is also called kiss-roll coating (Fig. 8.1).

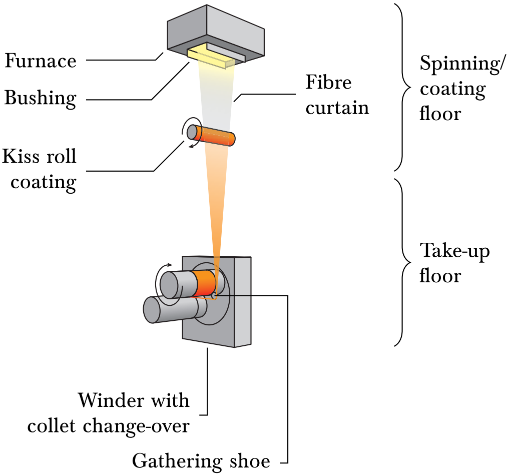

Figure 8.1: Schematic of the glass melt spinning process with the proposed in-line kiss-roll coating step.

8.1 The kiss-roll method

In principle, kiss-roll coating is the same set-up often used to apply sizing compositions to glass fibres;[57] however, in this case the purpose of said coating is not the improvement of the fibre-matrix adhesion – merely requiring a thin layer the size of a few molecules – but to deposit a controlled amount of thermoplastic material onto the fibre which is sufficient to make up the composite matrix after consolidation of the preform. Thin coatings can easily be realized at high velocity by using liquids with low viscosity and/or high surface tension.[67] Whereas, applying thick liquid coatings in a controlled manner and at high velocity is challenging, because it is inherently subject to flow instabilities.[68] However, in comparison to dip-coating, the proposed kiss-roll method introduces additional degrees of freedom to tune the deposition of the liquid onto the fibre, such as the rotational velocity of the roll or it's radius.

The goal of this study is to ascertain the suitability of kiss-roll coating with a polymer solution for in-line use with glass melt-spinning to fabricate hybrid bicomponent fibres and to characterise the sensitivity of the resulting fibre volume fraction to the fibre velocity. To that end, an experimental parameter study is presented which investigates the coating behaviour over multiple parameter levels of the process using a modular kiss-roll coating setup. The results of this parameter study inspire the design of a coating stage which is implemented into a monofilament glass spinning machine and used to extend the experimental investigation by observing the coating behaviour over a larger range of fibre velocities. We expect that the use of a kiss-roll enables a coating process in which the amount of fluid which is deposited on the glass filament can be controllably limited by the supply of fluid on the roll. We further hypothesize that the relative velocity between the fibre and the entrained film on the roll determines whether the coating thickness on the fibre is dominated by its own capillarity (the roll carries a sufficiently thick film at a sufficient speed) or by the limiting action of the roll (the roll carries a thin film at a low speed compared to the fibre velocity).

8.2 Parameter study

8.2.1 Materials and coating setup

Single glass filaments of finite lengths ($< 3\,\mathrm{m}$) and with a mean diameter of $12\,\mu\mathrm{m}$ were seperated by hand from an E-glass roving containing 204 fibres sized with 1 wt% 3-aminopropyltriethoxy silane (APTES). For each experiment, multiple individual filaments were drawn downwards vertically by a winder, touched a kiss-roll at a height of 850 mm above the winding axle, and dried at room temperature before touching the winder (Fig. 8.2). The fibre velocity V was varied for each experiment to yield samples with different coating thicknesses corresponding to fibre volume fractions v_f of the resulting bicomponent fibres ranging from 0.5 to 0.7. The kiss-roll was partially immersed in a dilute solution of poly(ester-amide) (PEA)[23,73] (Dow Europe GmbH) in trichloromethane (ReagentPlus® 132950, Sigma-Aldrich) at a constant supplementary angle of contact θ_c of 150° (see Fig. 8.4). The same materials were used in chapter 6, which describes in detail the characterization of the coating solutions. Apart from an opening to allow access for coating, the kiss-roll and bath were surrounded by a housing intended to trap evaporating solvent and keep the polymer concentration in the solution relatively stable for the duration of the experiment.

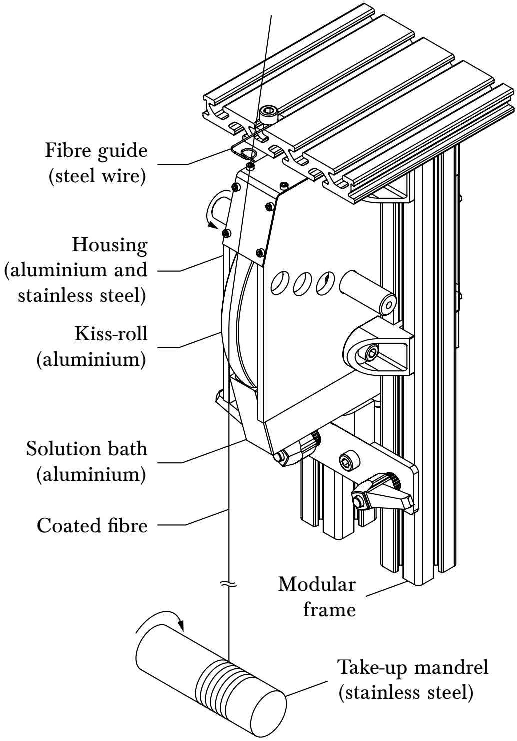
Fibre guide
(steel wire)
Housing
(aluminium and
stainless steel)
Kiss-roll
(aluminium)
Solution bath
(aluminium)
Coated fibre
Modular
frame
Take-up mandrel
(stainless steel)

Figure 8.2:
Isometric illustration of the setup used to conduct the coating experiments of the parameter study. The housing contains multiple openings to be used with kiss-rolls of various diameters. During an experiment, the unused bores are closed with polyethylene stoppers to reduce solvent evaporation. The bath containing the coating solution can be lowered for filling and the modular frame is adjustable to enable proper alignment of all parts when using kiss-rolls with different radii.

8.2.2 Design of experiment

To investigate the influence of major process parameters, the polymer concentration v_p in the coating solution, the peripheral roll speed U, and the kiss-roll radius R were varied according to a face-centred central composite design of experiment (Fig. 8.3). The incoming and outgoing

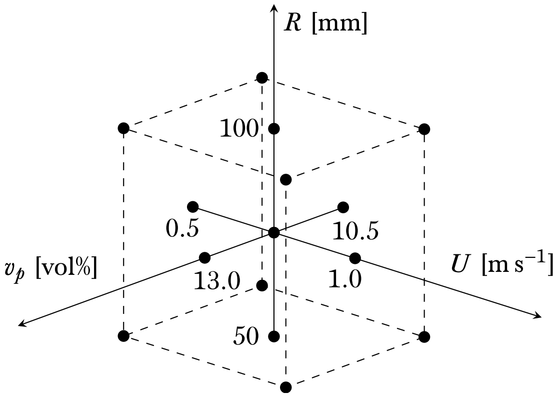

Figure 8.3: Scatter plot of the tested parameter combinations according to the face-centred central composite design. The low and high parameter levels are evenly spaced from the centre point and are indicated next to the face-centred points.

angles of the fibre with respect to the vertical direction were kept constant, meaning that the contact length between the fibre and the kiss-roll scaled linearly with the roll radius R. The experiments were run in random order to minimize the influence of time-dependent external disturbances. The chosen values of the varied parameters at the three levels of the study are listed in Table 8.1 together with the properties of the coating solution at the chosen levels of polymer concentration v_p.

8.2.3 Imaging

The coated fibres were imaged both transverse to their axes and in cross-sections in a Zeiss LEO 1530 (Gemini column) scanning electron microscope (SEM). The cross-sections were used to determine the mean diameters $\overline{d_c}$ of the glass cores. The transverse images were post-processed to measure the distribution of the coated diameters $d_{t,i}$ at each position i along the length of the fibres. The obtained values were combined to calculate the specimen's fibre volume fraction distribution $v_{f,i}$ according to Eq. 6.10, p. 64. The image processing method used to determine the yielded fibre volume fractions is equivalent to the one presented in section 6.3.3, p. 62.

Table 8.1: The parameter levels used for the experimental study. These levels were tested for in a face-centred central composite design scheme as shown in Fig. 8.3. The lower half of the table lists the fluid properties at each level of polymer concentration v_p in the coating solution.

	Low	Centre	High
U [$\mathrm{m\,s^{-1}}$]	0.50	0.75	1.00
R [mm]	50	75	100
v_p [vol%]	10.5	11.8	13.0
$\rho\vert_{v_p}$ [$\mathrm{kg\,m^{-3}}$]	1450	1445	1440
$\eta\vert_{v_p}$ [mPa s]	4.7	6.9	10.4
$\gamma\vert_{v_p}$ [$\mathrm{mN\,m^{-1}}$]	26.0	25.9	25.7

8.2.4 Modelling the fluid film on the kiss-roll

We expect that for the purpose of creating a thick coating on the fibre, the liquid film entrained by the roll must be thicker than the fibre at the position where it is in contact with the roll. This should enable the fibre to be fully immersed into the liquid and aid the deposition of a polymer sheath which fully surrounds the filament. To check if this condition is met in the experiments, the theoretical thickness of the fluid film on the kiss-roll is calculated using the analytical model of Tharmalingam and Wilkinson[94,95], which describes the fluid withdrawal onto a rotating roll.

This section abbreviates the theory used to model the fluid film thickness on the kiss-roll. Essentially, the thickness h of a fluid layer entrained on the surface of an object which is vertically withdrawn from a quasi-infinite bath is proportional to the object's characteristic dimension l times the capillary number Ca to the power of two thirds (Eq. 8.1).[67] The capillary number in turn is defined as the fluid's dynamic viscosity η divided by its surface tension γ times the withdrawal velocity V (Eq. 6.3, p. 55).

$$h \propto l\,Ca^{\frac{2}{3}} \tag{8.1}$$

This proportionality is lost for the case of thick coatings and for processing conditions under which these can be obtained, due to the influences of geometry, inertia, and flow instabilities.[67,68,71,72] Still, the capillarity of the flow is of crucial importance also in the case of kiss-roll coating, as is reflected in the following model proposed by Tharmalingam and Wilkinson.[94,95] They argue that in the case of thin films compared to the radius of the roll, the flux of fluid entrained on the surface of a rotating roll partially immersed in a quasi-infinite bath approximately equals the flux of fluid entrained by a flat plate withdrawn at an angle from a quasi-infinite bath. Eq. 8.2 describes this flux by relating a dimensionless film thickness To to the capillary number Ca and the obtuse angle θ_c at which the substrate leaves the bath.

$$\frac{To}{\left(1 - To^2\right)^{\frac{2}{3}}} \approx 0.944\, Ca^{\frac{1}{6}} \left(\frac{\sin(\theta_c)}{1 - \cos(\theta_c)}\right) \tag{8.2}$$

In the case of a roll, θ_c is the supplementary angle of contact between the roll and the undisturbed surface of the bath away from the roll, as it is defined in Fig. 8.4. The definition of the dimensionless film thickness To, given in Eq. 8.3, shows dependences on the density ρ of the fluid, its dynamic viscosity η, the gravitational acceleration g, the angle of contact θ_c, and the peripheral roll velocity U.

$$To \triangleq h_0 \left(\frac{\rho g \sin(\theta_c)}{\eta U}\right)^{\frac{1}{2}} \tag{8.3}$$

In Eq. 8.3, h_0 denotes the limiting constant film thickness, which is the film thickness far away from the bath in the case of a flat plate. This can be extended to the case of a roll by considering that while the volumetric flow remains constant, the flux changes along the circumference of the roll due to the influence of gravity, resulting in a variation of the film thickness. Equalizing the flux at the point where the surface of the roll leaves the bath with the flux for the case of a flat plate enables the calculation of the exact film thickness h at any position θ_i on the roll using Eq. 8.4.

$$h|_{\theta_i=0} \triangleq \hat{h} = h - \frac{\rho g h^3 \sin(\theta_i)}{3\eta U} = h_0 - h_0^3 \frac{\rho g \sin(\theta_c)}{3\eta U} \tag{8.4}$$

In Eq. 8.4, $\hat{h}$ represents the film thickness at the apex of the roll, which is defined as the origin of the angle of inspection, i.e. $\theta_i = 0$.

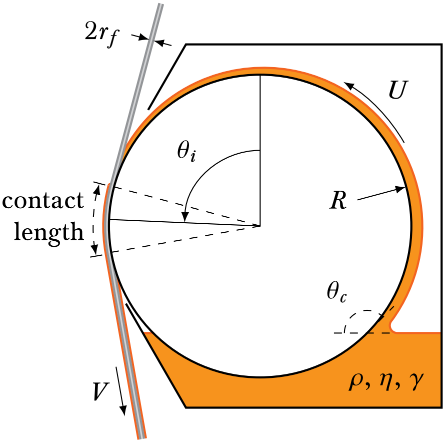

Figure 8.4: Schematic illustration of the material and process parameters involved in kiss-roll coating of fibres. A fibre with radius r_f is drawn at a linear velocity V over a roll with radius R which rotates with a peripheral velocity U and is partially immersed at an angle of contact θ_c in a bath of a fluid with density ρ, dynamic viscosity η, and surface tension γ. The fluid film thickness of interest h is positioned at the midpoint of the length of contact between the fibre and the roll, which is marked by the angle of inspection θ_i.

8.3 Results and discussion

8.3.1 Predicted fluid film thickness on roll

It was hypothesized that the realization of a thick coating which fully surrounds the glass fibre requires a solution film thickness on the kiss-roll which is larger than the diameter of the fibre, such that it can be fully immersed into the liquid. For the chosen parameters, the liquid film thicknesses on the roll predicted using the model of Tharmalingam and Wilkinson (Eq. 8.2–8.4) show that this condition was easily met while coating the glass monofilaments with a mean diameter of 12 µm (Fig. 8.5).

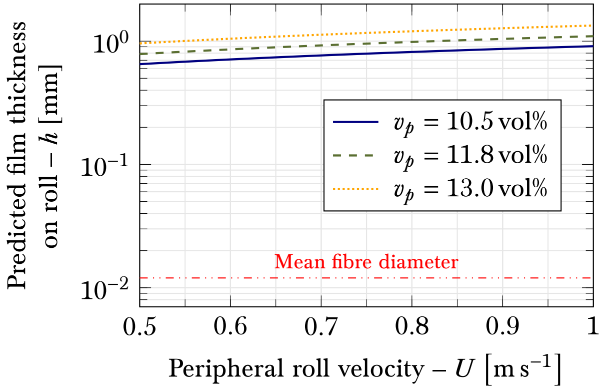

Figure 8.5: Liquid film thickness on the roll h as predicted by Eq. 8.2–8.4 plotted against the peripheral roll velocity U for the different polymer concentrations v_p used in the parameter study and compared with the mean diameter of the processed glass fibres. Supplementary angle of contact θ_c is 150° and angle of inspection θ_i is 90°. Note that the model assumes a large radius of the roll which allows it to be neglected.

8.3.2 Results of the parameter study

The qualitative results of the parameter study can be observed in the scanning electron micrographs, a representative selection of which is shown in Fig. 8.6. All samples shown in Fig. 8.6 were coated with a solution of 10.5 vol% poly(ester-amide) in trichloromethane on a kiss-roll with a radius of 50 mm and running at a peripheral velocity of $1\,\mathrm{m\,s^{-1}}$. The fibre velocity of each sample is indicated in the corresponding subfigure. While these specimens were selected from the same point in the parameter study, the qualitative results shown in the micrographs could be observed across all samples. It can be seen that fibres drawn over the roll at low velocity (Fig. 8.6a–c) show coatings of almost constant width, while higher fibre velocities (Fig. 8.6e) cause undulations in the deposited film thickness, which can become excessive to the extent where droplet formations around the glass core seem to be favoured (Fig. 8.6d). Note that this effect occurs only above a certain threshold fibre velocity, which may be different depending on the selection of the remaining parameters, but that the amplitude of these undulating

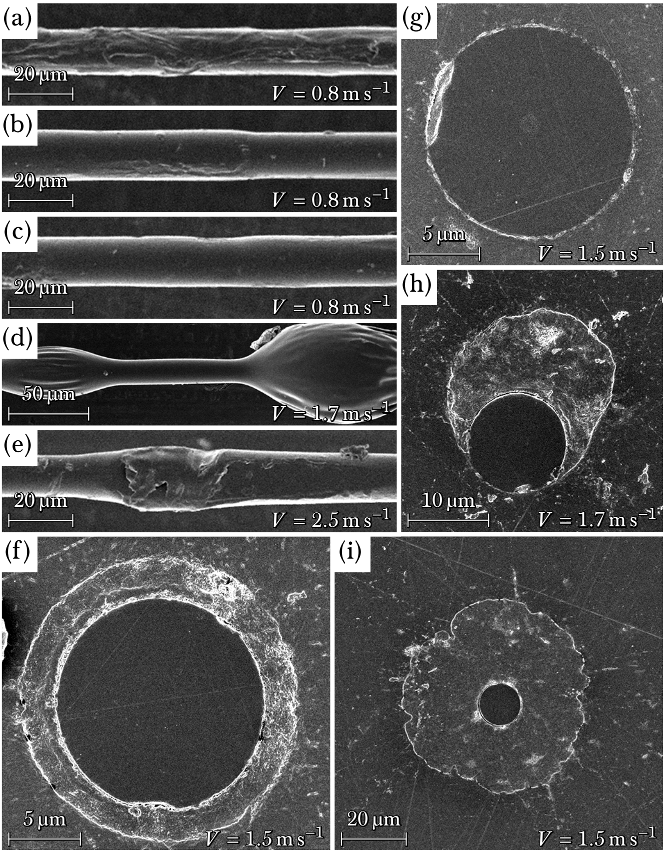
(a)
20 µm
V = 0.8 m s^{-1}
(b)
20 µm
V = 0.8 m s^{-1}
(c)
20 µm
V = 0.8 m s^{-1}
(d)
50 µm
V = 1.7 m s^{-1}
(e)
20 µm
V = 2.5 m s^{-1}
(f)
5 µm
V = 1.5 m s^{-1}
(g)
5 µm
V = 1.5 m s^{-1}
(h)
10 µm
V = 1.7 m s^{-1}
(i)
20 µm
V = 1.5 m s^{-1}

Figure 8.6:

Scanning electron micrographs of glass fibres kiss-roll coated with a solution of 10.5 vol% poly(ester-amide) in trichloromethane at a peripheral roll velocity U of 1 m s^{-1}, a roll radius R of 50 mm and a fibre velocity V of 0.8 m s^{-1} (a–c); 1.7 m s^{-1} (d, h); 2.5 m s^{-1} (e); and 1.5 m s^{-1} (f,g,i).

coatings does not necessarily scale with the fibre velocity (compare Fig. 8.6d and e). This variation in coating thickness can also be observed in cross-sectional images of the same fibre (Fig. 8.6f, g, i) and is attributed to Plateau-Rayleigh-like instabilities in the flow of the coating solution along the glass fibre.[23,68] Most coatings observed were concentric to the glass core, while some cross-sections revealed an asymmetric material deposition (Fig. 8.6h). These effects are not considered to be of major importance for further processing of preforms made from such hybrid bicomponent fibres, provided that the mean coating thickness remain constant at the mesoscale and considering that these coatings will always be re-melted for consolidation and forming into a composite part.[23]

The cross-sectional micrographs were analysed to measure the mean diameter of each sample's glass core and the micrographs with the transversely observed fibres were measured for their coated width at every cross-section along the filament. The resulting data was combined to yield a distribution of measured fibre volume fractions $v_{f,i}$ for each sample. Fig. 8.7 plots the mean values $\overline{v_f}$ of these distributions against the fibre velocity V for all fifteen parameter combinations investigated. The error bars show the standard deviation of each distribution and the solid lines represent a linear regression of the mean values, indicating the sensitivity of the fibre volume fraction towards changes in the fibre velocity for each set of parameters.

To gain a better overview over the behaviour of the coating process and to assess the influence of the different parameters on the achievable fibre velocity, the data obtained at each point in the investigated parameter space was analysed for the fibre velocity at which a mean fibre volume fraction of 0.7 was obtained. This value was chosen because it lies within the range covered in most plots shown in Fig. 8.7 and therefore represents a fibre volume fraction which can be realized using all parameter combinations which were tested. The intersections of the linear regression lines with a mean fibre volume fraction of 0.7 yielded the fibre velocity V required to realize a coating with this fibre volume fraction. These fibre velocities were then fitted as a function of the parameter space using a multiple regression as shown in Eq. 8.5, where c_i denote the fitting parameters for the regression.

$$\begin{aligned}\left(V|_{\overline{v_f}=0.7}\right)_i \approx\ & c_0 + c_1 v_{p,i} + c_2 U_i + c_3 R_i \\ & + c_{1,2} v_{p,i} U_i + c_{1,3} v_{p,i} R_i + c_{2,3} U_i R_i \\ & + c_{1,2,3} v_{p,i} U_i R_i\end{aligned} \tag{8.5}$$

The resulting function is plotted against the three coating parameters as a set of isosurfaces in Fig. 8.8. It is evident that for the goal of achieving the greatest possible fibre velocity V without altering the

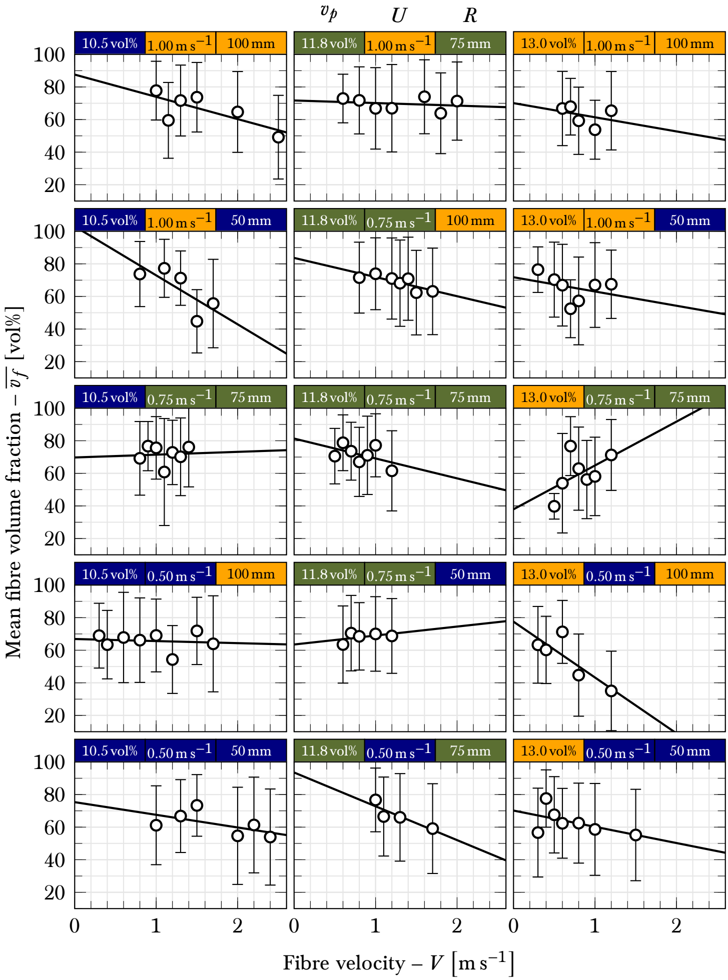

Figure 8.7: Mean values $\overline{v_f}$ of the measured fibre volume fraction distributions $v_{f,i}$ of each coated sample plotted against the fibre velocity V for each parameter combination tested within the central composite design study. The error bars show the standard deviation of each distribution and the solid lines represent a linear regression of the mean values.

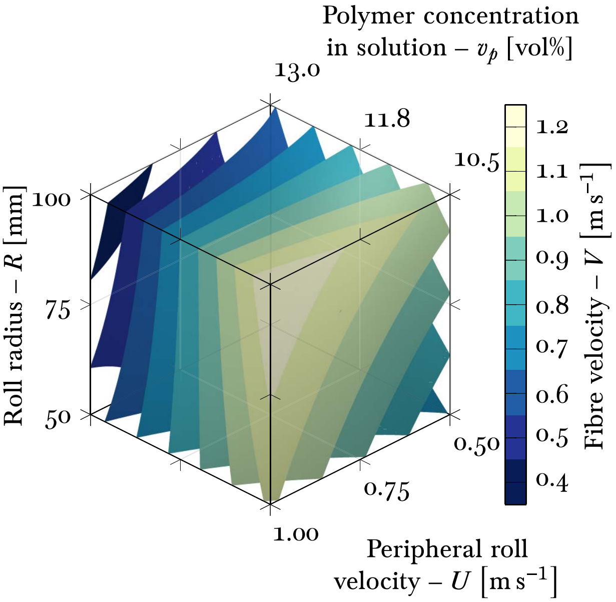

Figure 8.8: Isosurfaces of fibre velocity required to yield a coating corresponding to a fibre volume fraction of 0.7 as obtained from the multiple regression against the polymer concentration v_p, the peripheral roll velocity U, the roll radius R, and linear combinations thereof.

amount of deposited polymer on the fibre, Fig. 8.8 suggests that the polymer concentration in solution v_p be minimized and that the radius R and peripheral velocity U of the kiss-roll be maximized. At the same time, it shows that the achievable fibre velocity is most sensitive to the polymer concentration, suggesting that restrictions in the design of a coating stage in terms of size and power can be compensated for using a more dilute solution. Note that these conclusions are subject to the linearisation around the parameter space chosen for the presented study.

Comparing the slopes of the linear regression lines in Fig. 8.7, it becomes clear that the produced fibre volume fraction can be rather sensitive to changes in the fibre velocity itself, but that this sensitivity (the slope of the curve) changes across the parameter space. Same as the fibre velocity required to yield a wanted fibre volume fraction, the slope of these curves $\mathrm{d}\overline{v_f}/\mathrm{d}V$ was fitted using a multiple regression. The resulting function is plotted in Fig. 8.9. Based on this linearisation, it

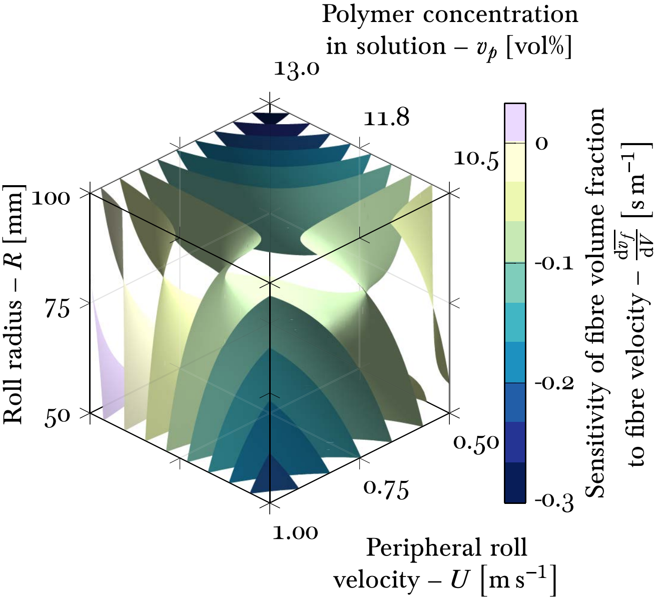

Figure 8.9: Isosurfaces of the yielded fibre volume fraction's sensitivity to changes in fibre velocity as obtained from the multiple regression against the polymer concentration v_p, the peripheral roll velocity U, the roll radius R, and linear combinations thereof.

can be concluded that the combination of process parameters resulting in the highest possible fibre velocity shows an intermediate sensitivity of the fibre volume fraction to the fibre velocity itself. However, already relatively small changes in the polymer concentration or the peripheral roll velocity can affect this sensitivity. It is therefore important to ensure sufficient control over these parameters to obtain a robust coating process.

8.4 Conclusion

Glass filaments kiss-roll coated with poly(ester-amide) at a fibre speed of $14\,\mathrm{m\,s^{-1}}$ yielded hybrid bicomponent fibres with a fibre volume fraction close to the range of 50 % to 70 %, thus proving that this coating method can be integrated in-line with glass melt spinning. The observed results of a face-centred central composite design of experiment indicate that the highest fibre speed V for the fabrication of hybrid bicomponent fibres of a given fibre volume fraction is achieved mainly through a minimization of the polymer concentration v_p. Note though that in the used setup, there is a limitation to the highest achievable fibre speed induced by the available distance between the coating application and the first contact point of the coated fibre with either the take-up bobbin or with other filaments at a gathering shoe earlier on. A higher fibre speed could thus mean that the surface of the coating does not dry before reaching the next contact point. The obtained results suggest that a maximization of peripheral roll speed U and roll radius R would further benefit a higher material throughput, although further investigation is needed to support this claim. It is still evident though that the peripheral roll speed could be used as a control input for the in-line coating process.

The promising results obtained from the study presented in this chapter led to the design of a pilot plant for the production of glass/thermoplastic polymer bicomponent fibres which combines glass melt spinning with an actual in-line kiss-roll coating unit. The function of that plant and further empirical data observed at higher fibre velocities are presented in the following chapter.

9

IN-LINE COATING PILOT PLANT

This chapter addresses the challenge of manufacturing hybrid bicomponent fibres in a continuous and efficient way. The output of the parameter study presented in chapter 8 inspired the design of a coating stage which is implemented in-line with a custom-built continuous glass monofilament spinning machine (Fig. 9.1). This pilot plant is used to obtain experimental data at higher fibre velocities and in a real environment. The presented results prove that hybrid bicomponent fibres can be manufactured via polymeric solution kiss-roll coating in-line with glass melt spinning. They further suggest that this method can be tailored towards a high-throughput industrial production of this novel type of hybrid preform.

The design of the spinning plant follows the common method of the direct roving process,[57,61] with the exception that only a single monofilament is spun. The top assembly of the machine contains a bushing made from a platinum-rhodium alloy which is embedded in refractory and stone. It is resistance-heated using a step-down transformer, which is connected via flexible copper laminates and water-cooled copper clamps. The transformer itself is water-cooled as well. The bushing contains a single spinning nozzle on the bottom and a sieve located about mid-height above the nozzle. The sieve functions as a buffer to keep solid chunks of glass from flowing into the nozzle, since the bushing is used to re-melt glass spherules or pellets. A vibrating feeder is included to

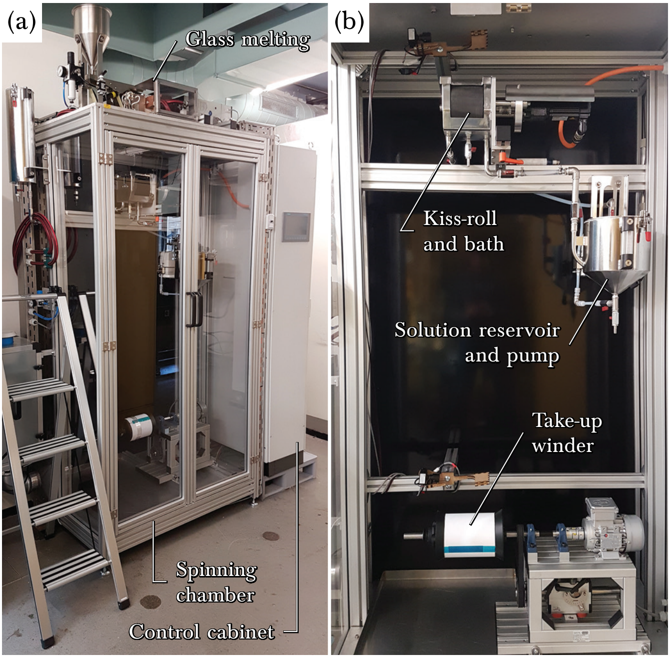

Figure 9.1: The setup used for the coating trials in-line with the glass monofilament spinning machine: the glass melting assembly lies on top of a spinning chamber equipped with a filtered exhaust to capture the solvent vapour (a); the continuously spun monofilament is run over a kiss-roll for coating and taken up by a traversing winder at the bottom of the chamber (b).

maintain a constant filling level inside the bushing. The stream of molten glass is drawn downwards by a winding axle mounted on a traversing mechanism (Uhing® rolling ring drive) and collected on a cardboard collet covered with polytetrafluoroethylene (PTFE) film. In between the nozzle and the winder, a kiss-roll coating unit applies the polymeric sheath to the monofilament. The rotating roll is partially immersed in a bath with constant filling level which is supplied with a continuous flow of polymer solution from a reservoir tank via a membrane pump. The bath contains an outflow which transports excess solution back to the reservoir. This creates a continuous circulation of the solution, which serves for a more homogeneous mixing. The entire assembly below the bushing is contained within a fume chamber which protects workers and the laboratory environment from potentially harmful solvent vapour. It is fitted with an exhaust which continuously extracts the vapour-laden air inside the chamber and pushes it through an activated carbon filter (CarbonActive EC inline filter unit HL, $500\,\mathrm{m}^3\,\mathrm{h}^{-1}$).

The machine was designed for the purpose of implementing a modular coating setup and to allow changes and retrofitting in light of further developments throughout the research process and beyond the presented work. The entire setup shown in Fig. 9.1 (exclusing the fume exhaust) was designed and built at Woltz Glasfasertechnologie GmbH in Wertheim, Germany, and commissioned at the Laboratory of Composite Materials and Adaptive Structures at ETH Zürich. The remaining sections of this chapter report the results of a high velocity in-line coating study and describe the general process used to produce bicomponent fibre sample for the remainder of this thesis.

9.1 In-line coating study

9.1.1 Spinning and in-line coating

Aluminium-borosilicate glass beads (Sigmund Lindner SiLibeads Type SL) were re-melted in the spinning machine's resistance-heated bushing and extruded downwards by gravitational flow. The spun fibre was picked up and collected on a rotating and traversing cardboard collet covered with a PTFE film and with a diameter of 135 mm. The drawing velocity used ranged from $0.48\,\mathrm{m\,s}^{-1}$ to $8.1\,\mathrm{m\,s}^{-1}$. Note that in this case, a higher fibre velocity also resulted in a thinner fibre, because the flow of glass through the spinning nozzle was kept constant, namely at a rate of $\sim 11\,\mathrm{mL\,h}^{-1}$ (volume after solidification). Between the spinning nozzle and the winder, the fibre was run over a kiss-roll with a radius of 65 mm which was partially immersed in a solution of either 10 vol% or 11.5 vol% polycarbonate (Covestro Makrolon® 3108) in trichloromethane (319988, Sigma-Aldrich) at a supplementary angle of contact θ_c of 141°. The roll rotated at a constant peripheral velocity of $0.611\,\mathrm{m\,s}^{-1}$ when coating with the solution containing 10 vol% polymer and at $0.305\,\mathrm{m\,s}^{-1}$ when coating with the 11.5 vol% solution. A total volume of 2.2 L of coating solution was put into a reservoir tank and a membrane pump was used to circulate the fluid through the coating bath. This was done to retain a homogeneous solution and minimize changes in polymer concentration caused by excessive solvent evaporation at the kiss-roll. Each fibre velocity setting was kept for at least 1 min to yield a large enough sample for analysis before simultaneously changing the velocity and traversing to an empty region on the collet.

9.1.2 Thermogravimetric analysis (TGA)

The composition of the coated samples was determined using thermogravimetric analysis (TGA) in a Perkin Elmer Pyris 1. One loading per sample with a weight between 10 mg and 20 mg was put into a tared platinum crucible and heated from room temperature to 640 °C at a rate of $10\,\mathrm{K\,min^{-1}}$ to thermally decompose the polymer. The ratio of the final sample weight and the original weight was taken as the fibre weight fraction and converted into the fibre volume fraction using densities of $1.20\,\mathrm{g\,cm^{-2}}$ for the polycarbonate[96] and $2.59\,\mathrm{g\,cm^{-2}}$ for the glass[97].

9.1.3 Results and discussion

The resulting fibre volume fractions are plotted against the capillary number Ca_V of the fibre (defined in Eq. 9.2) at the corresponding fibre velocity V in Fig. 9.2. The plot shows that for both polymer concentrations, an increase in fibre velocity from the values investigated in the parameter study first leads to an increased coating thickness (corresponding to a lower fibre volume fraction in the dry bicomponent fibre), until the velocity reaches a critical value. This behaviour is followed by a transition to a gradual decrease in coating thickness. The data also suggests that the extreme point of this curve lies at a lower fibre volume fraction when coating with a higher concentration of polymer in the solution.

It was hypothesized that a relative increase of the fibre velocity with respect to the peripheral roll velocity would lead to a limiting effect on the coating thickness: so long as the fibre is drawn at a low velocity through a comparatively thick film on the roll, the amount of liquid withdrawn by the fibre is governed by classical dip-coating phenomena. In these conditions, the normalized liquid coating thickness h_l/r_f more or less follows a power-law with respect to the capillary number at the

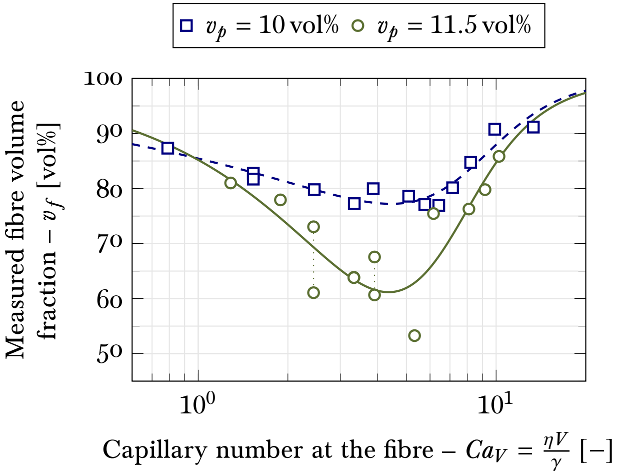

Figure 9.2: Measured fibre volume fractions v_f of the coated fibres plotted against the capillary number Ca_V at the corresponding fibre velocity V for coating with a polymer concentration in solution v_p of 10 vol% (blue squares) and 11.5 vol% (green circles). The trend lines for both datasets are calculated following Eq. 9.4 and Eq. 9.5.

fibre Ca_V (Eq. 9.1).

$$\frac{h_l}{r_f} \approx \mathrm{A} Ca_V^{\mathrm{B}} \quad \text{for } \frac{Ca_V}{Ca_U} \ll 1 \tag{9.1}$$

$$Ca_V \triangleq \frac{\eta V}{\gamma} \tag{9.2}$$

$$Ca_U \triangleq \frac{\eta U}{\gamma} \tag{9.3}$$

However, as the capillary number at the fibre increases, more viscous drag is created which causes more fluid to be entrained on the surface of the fibre. Eventually, this drag becomes too large for the amount of liquid supplied by the kiss-roll and the coating thickness cannot increase any more. Increasing the fibre velocity even further means that the limited amount of fluid delivered per unit time is being spread over a longer distance on the fibre, resulting in a decrease of coating thickness. Assuming that this phenomenon is mainly determined by the ratio of the capillary number at the fibre and at the roll, governing the amount of liquid the fibre “would like” to withdraw and the amount supplied by the roll, respectively, and that the influence of this ratio grows progressively, we can derive a crude law for the behaviour of the coating thickness when going through this transition (Eq. 9.4).

$$\frac{h_l}{r_f} \approx \frac{\mathrm{A}\,Ca_V^{\mathrm{B}}}{1+\mathrm{C}\left(\frac{Ca_V}{Ca_U}\right)^{\mathrm{D}}} \tag{9.4}$$

$$\frac{1}{v_f} = 1 + v_p\left[\left(1+\frac{h_l}{r_f}\right)^2 - 1\right] \tag{9.5}$$

In Eq. 9.4, A, B, C, and D are used as fitting parameters. Together with Eq. 9.5, fitting this law to the experimental data results in the trend lines shown in Fig. 9.2. Looking at the scatter of the experimental data around these trend lines, it is evident that with increasing polymer concentration it is not only possible to obtain lower fibre volume fractions at the valley of the curve, but the overall level of scatter also increases. The latter is highlighted by the repeated experiments with a polymer concentration of 11.5 vol% at capillary numbers Ca_V between 2 and 4. The reason for the difference in the depths of the valley for varying polymer concentrations is not obvious, as a change in the polymer solution has the same relative effect on the capillarity of the flows at the roll and at the fibre. Further investigations on this matter require a broader set of experimental data or an extended parameter study based on numerical modelling. Nevertheless, the data obtained within this study proves that the kiss-roll can be used as a limiting mechanism for the entrainment of a fluid layer on the fibre. The observed behaviour includes a smooth transition from a coating behaviour dominated by the capillarity of the flow at the fibre into a region where the supply of fluid provided by the roll determines the amount of fluid entrained by the fibre. In combination with the appropriate choice of fluid properties and process parameters, this mechanism may be exploited to apply a controlled amount of polymer at higher fibre velocities by designing the process such that its point of operation lies on the right side of the valley in Fig. 9.2.

9.1.4 Conclusion

The presented study gives first experimental proof that the fabrication of hybrid bicomponent fibres is possible by applying a polymeric solution to a continuously spun glass fibre using a kiss-roll in-line with the melt spinning process. The presented approach already enabled the fabrication of samples with fibre volume fractions suitable for the production of high-performance structural composites at fibre velocities around $5\,\mathrm{m\,s^{-1}}$.

Furthermore, the coating behaviour which was observed at high fibre velocities in the in-line experiments shows that the kiss-roll acts as a controllable limiting mechanism for the deposition of polymer on the fibre. This can be exploited for the benefit of designing a high-throughput production process: choosing a high polymer concentration and operating the process in the regime where the supply of fluid on the roll limits the amount deposited on the fibre allows for the maximization of the fibre velocity. A high fibre velocity is desired because it allows the production of a thin and therefore strong fibre at a higher throughput.

This study proves that in-line kiss-roll coating works for the fabrication of a hybrid bicomponent monofilament. It is expected that the method can be easily scaled up by processing many fibres in parallel, as it is usually done in glass melt spinning. However, this might give rise to undesirable interactions between the fibres on the roll. Particular attention needs to be given that the coatings of the individual filaments do not coalesce and future work on this method should focus on investigating this aspect. Nevertheless, the demonstration of continuously producing a hybrid bicomponent monofilament provides opportunities for further investigation of this novel preform material and advances the development of high-volume value chains based on bicomponent fibres.

Part III

PROCESSING

10

CONSOLIDATION IN THEORY

This third part of the thesis is intended to give an insight into the functionality of hybrid bicomponent fibres (BCF) as advanced preform materials for high-volume composites production using stamp forming. Stamp forming involves heating the preform to a desired temperature above the liquidus point in a suitable oven, transferring the hot material into a press which subsequently closes to impart the mould's shape onto the material and to cool it at the same time, followed by opening the press and demoulding the stamped component after it is cooled below solidus temperature. During this process, the material undergoes a number of thermomechanical phenomena, which potentially affect the outcome of the process and the quality of the fabricated part. This chapter presents a theoretical discussion of potential influences these phenomena might have on the laminate quality of stamp formed BCF before moving on to the experimental studies.

10.1 Deformation of the molten sheaths

The basic benefit attributed to the concept of hybrid bicomponent fibres is that they avoid any impregnation flows over the entire value chain; their consolidation merely requires a coalescence of the molten thermoplastic sheaths and an extraction or collapsing of remaining voids. The effects of polymer sintering have already been reported to be significant consolidation mechanisms in commingled yarns.[33] In BCF-based preforms, homogeneous sintering and welding mechanisms, which are governed by the interplay of surface energies and the formation of autohesion, are expected to be critical to ensure high consolidation quality of the matrix in the final laminate.

When imagining the cross-section of a preform containing a unidirectional arrangement of BCF and under the admittedly reductive assumption of quadratic tightest packing of these fibres, a unit cell approach can be used to illustrate the initial deformations which molten polymer sheaths undergo. Liquefying these sheaths during heating leads to their coalescence and the formation of a continuous polymer network, driven by the surface tension of the polymer melt. This can be demonstrated using a simple transient two-phase fluid dynamics simulation, in which the sheaths are in contact at the initial configuration. The fibre cores are modelled as rigid and stationary bodies, the polymer sheaths are assigned the properties of the melt phase at the desired temperature prior to stamping, and the free volume between the sheaths are assigned the properties of air. Accounting for surface tension between the two fluid phases, namely the polymer melt and air, means that the just described configuration is not in equilibrium. A transient simulation with this arrangement as the initial condition will therefore seek to deform the interface between the two phases such that surface energies are minimized. This energy is spent by moving the two fluids and ultimately dissipates through viscous friction. Because of the fluid viscosities, this process takes a certain amount of time. It is the purpose of this theoretical study to account for the order of magnitude of this time required to coalesce the sheaths.

10.1.1 Modelling approach

To that end, a two-dimensional unit cell model assuming quadratic tightest packing of the BCF prior to heating was implemented and solved in COMSOL Multiphysics® using a phase field approach. While a random packing is more realistic, the reduction to a smaller unit cell saved some computational efforts and assuming quadratic packing has been shown to provide a good approximation of the maximum volume fraction occupied by unidirectional fibres as achieved in practice.[98] A core fibre radius of 12.5 μm and a surface tension of the polymer melt of $27.6\,\mathrm{mN\,m^{-1}}$ (Covestro Makrolon® 3108 polycarbonate melt, pendant drop method at 300 °C on a Krüss DSA100 drop shape analyser) were chosen. The properties of air were selected from COMSOL's material library. The properties of the polycarbonate melt were taken from the datasheet[96], with a dynamic viscosity of 782.5 Pa s at a temperature of 300 °C and a shear rate of $1\,\mathrm{s}^{-1}$ extracted from a Cross-WLF model provided by Covestro. Shear thinning was neglected to save computational effort and it is asserted that the viscosity at the chosen shear rate represents a conservative value for the purposes of determining the time required for the sheaths to fully deform.

10.1.2 Results

The distribution of the melt and air phases after reaching equilibrium conditions are shown in Fig. 10.1. The three plots assume different fibre volume fractions v_f of the BCF. The glass fibre cores are shown in grey, the initial melt-air interface is drawn as a dotted line, and the distribution of polymer melt and air after reaching equilibrium are shown in orange and white, respectively. The plots show that for a quadratic tightest packing, the sheaths coalesce at all four contact points and tend to form a circular air pocket. This is expected due to surface tension being the sole driver for deformation of the melt-air interface in this case. At the

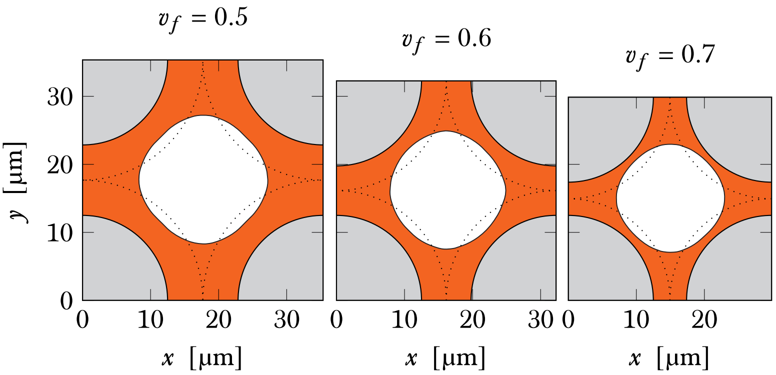

Figure 10.1: Simulation results for the coalescence of molten polymer sheaths (shown in orange) driven by surface tension for the case of quadratic tightest packing prior to heating and for different fibre volume fractions v_f of the BCF. The fibre cores are shown in grey and the initial boundaries of the sheaths prior to melting are drawn as dotted lines.

simulated temperature and corresponding melt viscosity, reaching this equilibrium condition took less than 10 ms for all values of v_f. Based on the results of this simple model, it is asserted that deformations of the sheaths driven by surface tension occur practically instantaneously while heating a BCF preform to the desired temperature prior to stamping. This means that the re-distribution of the polymer melt during stamping is not hindered by the interplay of surface tension and melt viscosity.

10.1.3 Comments on void formation and stability

The results further suggest that the coalescing of the sheath during melting might result in entrapped air pockets, particularly when accounting for the fact that the individual filaments are rarely perfectly aligned in parallel. However, it is expected that collapsing these voids is not a critical issue when consolidating the material in a hydraulic press. The stability of voids carrying entrapped air is governed by, again, the surface tension of the matrix fluid and by the vapour pressure of the possibly humid air entrapped in the void.[98,99] When processing the material in very humid environments, the water-uptake of the polymer matrix can result in vapour-laden voids which exert up to and slightly above $\sim 400\,\mathrm{kPa}$,[98] depending on the material. The stability of spherical voids of various sizes and carrying a given vapour pressure can be assessed using Eq. 10.1, which gives the relationship for stable voids with a total internal pressure $p_{v,s}$ and diameter d_v in the environment of a fluid matrix with the surface tension γ_m and carrying the pressure p_m.[98]

$$p_{v,s} = p_m + \frac{6\gamma_m}{d_v} \tag{10.1}$$

Fig. 10.2 plots stable void pressures against the void diameter for a variety of matrix pressures. Voids with a total internal pressure and diameter situated below the line in Fig. 10.2 dissolve and collapse, voids situated on the line remain stable, and voids situated above the line grow. In the case of consolidation methods based on vacuum bags alone or in low-pressure autoclave processes, it is evident that void growth can be an issue and needs to be addressed. In contrast, hydraulic presses can commonly exert consolidation pressures on the order of 0.1 MPa to 10 MPa. Considering that during closing of the press, most of the applied force is initially carried by the matrix, the magnitude of the matrix pressure dominates over both the surface tension and the

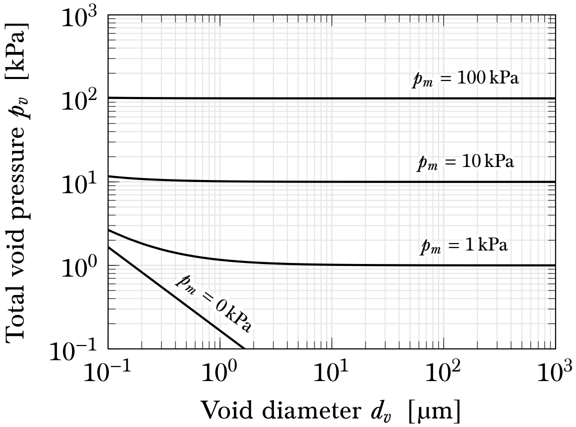

Figure 10.2: Void stability map according to Eq. 10.1 for a matrix with surface tension $\gamma_m = 27.6\,\mathrm{mN\,m^{-1}}$. At a given matrix pressure p_m, voids with total internal pressures and diameters below the line dissolve and collapse. Adapted and extended from Gutowski.[98]

commonly achieved levels of void pressure, which, in theory, leads to a collapse of all voids. The only realistic scenario which would allow voids to remain is if during closing of the press, too much force is immediately carried by the reinforcing fibres. It is asserted that while this can happen, it is less likely to occur in BCF preforms, because of the more homogeneous distribution of fibres and matrix polymer. As long as every fibre is completely covered by its sheath, they are not in direct contact which each other and thus any initial load applied to the preform has to be transferred through the matrix. Still, experimental proof is required to support these comments, as for example the results of the stamp forming study presented in chapter 12.

10.2 Autohesion of the matrix interfaces

With the assertion that the deformation of the sheaths and the corresponding mechanisms of void formation and collapse are not time-critical for the consolidation of BCF preforms, the next aspect to be considered is the mechanical integrity of the laminate. A crucial part of this is the integrity of the matrix itself. Even in light of the sufficient consolidation pressure exerted by hydraulic presses, considering that BCF preforms start out with a significant amount of air distributed throughout the entire geometry means that a lot of gaps within the matrix have to be closed during stamping. But collapsing all voids does not necessarily mean that the matrix has reached its full strength. A thermoplastic polymer's ability to transfer mechanical stresses in bulk stems not just from the strength of its covalent bonds within one macromolecule, but also from the entanglement of these polymer chains and their intermolecular forces. This entanglement occurs in the molten state, in which the molecules carry sufficient energy to overcome intermolecular interactions and are able to move past and around each other. These random movements are also termed as "reptation" in reference to the motion of snakes in confined spaces. Movements require time and therefore closing a gap in the matrix during consolidation requires the macromolecules to "reptate" across the newly formed contact area and entangle in order to achieve bulk polymer properties.

In thermoplastic polymer technology, the process of reptation across molten interfaces until achieving bulk strength is referred to as autohesion and constitutes the governing mechanism in thermoplastic welding methods (next to general thermodynamics). The movement of the molecules can be described using reptation theory, which models a single chain of an amorphous polymer as constrained in a tube of the length L which represents the steric effects applied by the other chains in close proximity. It is postulated that the chain can only move within the confines of the tube, driven by Brownian motion. The time it takes for the chain to fully exit the tube is defined as the reptation time t_r.[100,101] Because reptation is driven by Brownian motion, the reptation time changes with temperature T. This change is often described by an Arrhenius relationship like the one given in Eq. 10.2, where A and B are used as fitting parameters.

$$t_r = \mathrm{B} \cdot \exp\left(\frac{\mathrm{A}}{T}\right) \tag{10.2}$$

Under isothermal conditions and a perfectly intimate contact of the two adherends, the time required for autohesion to achieve full strength is by definition the reptation time t_r.[101] When bringing the adherends in contact at sufficiently high temperature during the stamp forming process, it can therefore be assumed that full autohesion is achieved for

$t_r \ll t_h$, where t_h is the holding time inside the press and assuming that the press is opened shortly after full solidification.

For example, McIlroy & Olmsted report a reptation time of 0.033 s at 250 °C for a polycarbonate with a molecular weight M_w of 60 kg mol^{-1} and a glass transition temperature T_g of 140 °C.[102] Knowing the glass transition temperature of Covestro's Makrolon® 3108, which is used in the experiments in chapter 12, to be 149 °C[96] allows for an approximated guess of its reptation time at the same temperature. The relationship of glass transition and molecular weight in polycarbonates roughly follows Eq. 10.3.[103]

$$T_g\,[\mathrm{K}] = T_{g,\infty}\,[\mathrm{K}] - \frac{\mathrm{C}}{M_w} \tag{10.3}$$

In Eq. 10.3, $T_{g,\infty}$ denotes the limiting glass transition temperature for infinite molecular weight and C is a constant to be used as fitting parameter. For polycarbonates, Dobkowski reports a $T_{g,\infty}$ of 435.8 K. Solving Eq. 10.3 for C using McIlroy & Olmsted's data leads to $\mathrm{C} = 1359\,\mathrm{kg\,K\,mol^{-1}}$ and therefore a molecular weight of $\sim 100\,\mathrm{kg\,mol^{-1}}$ for Makrolon® 3108. Knowing that the reptation time scales with $t_r \propto M_w^{3.4}$,[104] the reptation time of Makrolon® 3108 at a temperature of 250 °C can finally be approximated to a value of $t_r = 0.018\,\mathrm{s}$. This means that as long as the temperature of the processed material equals or exceeds these 250 °C for at least 0.018 s after collapsing all voids, autohesion can be considered fully complete everywhere in the laminate. Seeing as holding times t_h during stamp forming are commonly on the scale of a few tens of seconds, autohesion should theoretically not pose a practical issue.

10.3 Cooling inside the press

As soon as the heated preform is removed from the oven, it starts to cool and eventually solidifies. During transfer from the oven to the press, heat is lost primarily to the surrounding air through both natural and forced convection. Upon closing of the mould, conductive heat transfer forces an asymptotic reduction of temperature in the material, approaching the temperature of the mould itself. Ideally, the press is opened as soon as the last region in the material has solidified to guarantee a low cycle time. To predict the required holding time of the material inside the press, t_h, it is useful to approximate the cooling behaviour of the experimental setup used. In chapter 12, these predictions are used to choose appropriate levels for the holding time used in experimental studies and the reader is referenced to section 12.1.1 in particular for more information on the press setup used.

To simplify the model, the convective heat loss during material transfer from the oven to the press is neglected and it is assumed that the conductive heat transfer starts once the press is fully closed. While these assumptions grossly over-simplify the thermodynamic problem at hand, it is asserted that the resulting approximative prediction of the holding time t_h is sufficiently accurate to inform the choice of an experimental parameter range. Under the aforementioned assumptions, the problem can be reduced to one-dimensional heat transfer in through-thickness direction and results in the second-order partial differential equation given in Eq. 10.4.

$$\rho_c c_{p,c} \frac{\partial T}{\partial t} - \nabla \left(\lambda_c \nabla T \right) = 0 \quad \wedge \quad \nabla = \frac{\partial}{\partial x} \tag{10.4}$$

The setup used in chapter 12 is symmetrical and includes two platens made from polyether ether ketone (PEEK) as flat moulds mounted on larger, heated steel platens in the hydraulic press. It is assumed that while the large steel platens, the temperature of which is controlled by the press, remain isothermal, the PEEK moulds heat up during stamping. The model domain therefore includes half the laminate thickness $0.5 \cdot h_c$, originating at $x = 0$, and the thickness of one PEEK platen h_p. The boundary conditions at both ends are given in Eq. 10.5 and 10.6, where T_p is the controlled press temperature of the steel platens.

$$\nabla T \left(x = 0 \right) = 0 \tag{10.5}$$

$$T \left(x = 0.5 \cdot h_c + h_p \right) = T_p \tag{10.6}$$

The initial conditions are given in Eq. 10.7 and 10.8, where T_0 is the initial temperature of the composite sample to which it is heated in the oven.

$$T \left(t = 0, 0 \le x \le 0.5 \cdot h_c \right) = T_0 \tag{10.7}$$

$$T \left(t = 0, 0.5 \cdot h_c < x \le 0.5 \cdot h_c + h_p \right) = T_p \tag{10.8}$$

The composite's density ρ_c, specific heat capacity $c_{p,c}$, and thermal conductivity λ_c were calculated following Eq. 10.9–10.11, as adapted from Gutowski,[98,99] respectively, and using the data of both matrix and fibre materials from their respective data sheets.[96,97]

$$\rho_c = v_f \rho_f + \left(1 - v_f\right) \rho_m \tag{10.9}$$

$$c_{p,c} = \frac{1}{\rho_c} \left(v_f \rho_f c_{p,f} + \left(1 - v_f\right) \rho_m c_{p,m}\right) \tag{10.10}$$

$$\lambda_c = \left(1 - v_f\right) \lambda_m + \frac{\sqrt{v_f} \lambda_m}{1 - \sqrt{v_f} \left(1 - \frac{\lambda_m}{\lambda_f}\right)} \tag{10.11}$$

The density, specific heat capacity, and thermal conductivity of the PEEK platens used were $\rho_p = 1364 - 0.205 \cdot T$ [K] $\mathrm{kg\,m^{-3}}$, $c_{p,p} = 3.70 \cdot T$ [K] $\mathrm{J\,kg^{-1}\,K}$, and $\lambda_p = 0.284\,\mathrm{W\,m^{-1}\,K}$, respectively.

The problem was solved in COMSOL Multiphysics® and the resulting prediction for the required holding time t_h is simply the simulation time at which the maximum temperature in the composite, always occurring at $x = 0$, crosses $T_g = 149\,°\mathrm{C}$. Table 10.1 lists the resulting predictions for different combinations of initial temperature and press temperature used in chapter 12.

Table 10.1: Predictions of the required holding time t_h for different settings of initial temperature T_0 and press temperature T_p, and for a fibre volume fraction v_f of 0.68.

T_0	T_p	t_h
280 °C	120 °C	4.7 s
300 °C	120 °C	6.0 s
280 °C	145 °C	10.0 s
300 °C	145 °C	13.1 s

Before presenting the stamp forming experiments themselves, however, chapter 11 reports on two preparatory trials investigating the achievable part quality under ideal conditions using variothermal compression moulding and highlighting the matrix deformation and re-distribution in the unconsolidated preform during heating.

11

ACHIEVABLE CONSOLIDATION QUALITY AND PREFORM VOID CONTENT

The two preparatory experiments presented in this chapter are intended to provide further insight into the consolidation behaviour of hybrid bicomponent fibre preforms before moving to the stamp forming process. A compression moulding trial under ideal conditions for consolidation highlights the achievable optical quality to which BCF laminates can be consolidated. A polished cross-section of a pre-heated but unconsolidated BCF preform illustrates the high amount of air inside the material before moving to the press stage in stamp forming and how the molten matrix re-distributes prior to consolidation.

11.1 Sample preparation

Aluminium-borosilicate glass beads (Sigmund Lindner SiLibeads Type SL) were melted in a Joule heated platinum-rhodium bushing, drawn from its single spinning nozzle, and wound onto a collet with a diameter of 135 mm mounted on a traversing winder situated 1.77 m below the nozzle. At a distance of 0.37 m below the nozzle, the continuously spun monofilament was drawn over a kiss-roll with a radius of 65 mm and coated with a solution of 11.5 vol% polycarbonate (Covestro Makrolon® 3108) in trichloromethane (319988, Sigma-Aldrich), resulting in a bicomponent fibre cake such as the one shown in Fig. 11.1. The roll rotated at a constant peripheral velocity of $0.305\,\mathrm{m\,s^{-1}}$ and the fibre velocity was

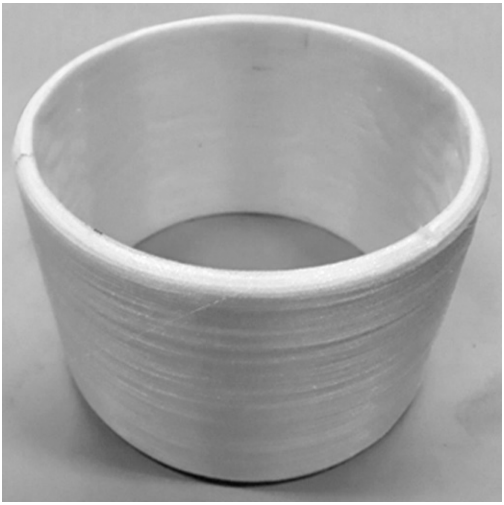

Figure 11.1:

Cake of polycarbonate-clad glass monofilament as obtained from the spinning process. Its inner diameter is 135 mm and its height is 80 mm.

varied over a range of $4\,\mathrm{m\,s^{-1}}$ to $7\,\mathrm{m\,s^{-1}}$ to counteract changes in the amount of coating deposited on the fibres, which were caused by the evaporation of solvent from the system.

The compositions of the obtained fibres were determined using thermogravimetric analysis (TGA) in a Perkin Elmer Pyris 1. One loading per sample with a weight between 10 mg and 20 mg was placed in a tared alumina crucible and heated to 640 °C to thermally decompose the polymer. The ratio of the final sample weight and the original weight was taken as the fibre weight fraction and converted into the fibre volume fraction using densities of $1.20\,\mathrm{g\,cm^{-2}}$ for the polycarbonate[96] and $2.59\,\mathrm{g\,cm^{-2}}$ for the glass[97].

The thus fabricated and characterized BCF samples were used for all experimental investigations presented in this and the following chapter. One sample was used for each of the following two subsections, while the remaining samples were processed with stamp forming experiments as reported in chapter 12.

11.2 Compression moulding

As a first test, a unidirectional preform of glass/polycarbonate bicomponent fibres with a glass volume fraction of 0.32 was sandwiched between two release films and inserted into a closed quadratic mould with an edge length of 58 mm. With the mould still open, the assembly was placed into a hydraulic hot press (Fontijne TP 400) and evacuated to an absolute pressure of $\sim$ 50 mbar. The press was then heated to 300 °C, closed to a compaction force of 30 kN, and subsequently left to cool while maintaining the compaction force. Upon reaching room temperature, the vacuum was released, the press opened and the material was demoulded.

Fig. 11.2 shows the state of the material prior to and right after the compression moulding process. It is worth to point out the optical quality of this consolidated sample. Due to the entire heat cycle happening in vacuum, potential discolourations due to thermal degradation were completely avoided and the transparency of the resulting specimen points towards a completely void-free laminate. The slight opacity is mainly attributed to light scattering caused by the difference in indices of refraction of the fibre and matrix materials. This result illustrates that at least with a low fibre volume content and under ideal conditions, BCF-based materials can be consolidated to a high aesthetic quality.

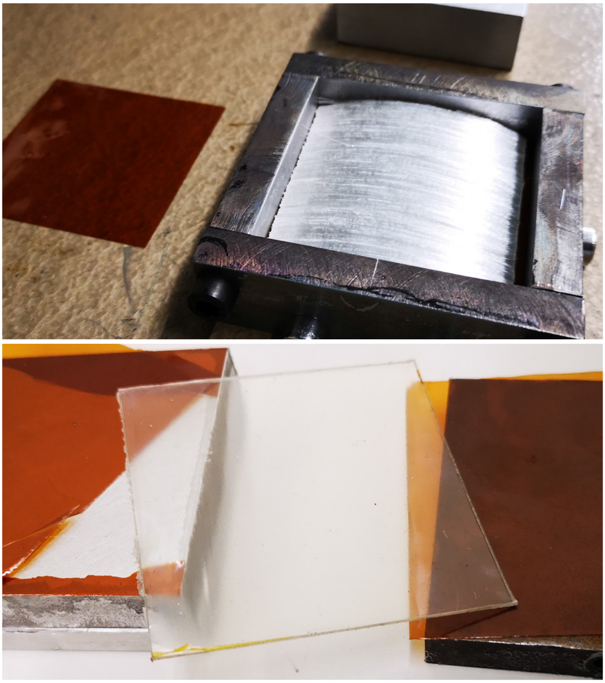

Figure 11.2:
Glass/polycarbonate bicomponent fibre preform inserted into rectangular mould with release film on the left and mould lid in the background (top); and the same sample in consolidated state, freshly demoulded (bottom).

11.3 Microstructure after heating

To assess the microstructure of the preform after heating and before the consolidation step in stamp forming and to illustrate the actual re-distribution of the matrix polymer during heating, a unidirectional preform of glass/polycarbonate bicomponent fibres containing a mean glass volume fraction of 0.15 was heated to 300 °C and left for cooling without applying any consolidation pressure. The material was taped onto a metal frame at both ends of the fibres so that the majority of the sample would not make contact with other surfaces in the oven.

The resulting sample was mounted in epoxy (Struers SpeciFix), cut and polished in transverse direction relative to the fibres, and imaged with a digital optical microscope (Keyence VHX-6000, VH-ZST lens). Fig. 11.3 shows one of the resulting micrographs. The picture encompasses the entire thickness of the specimen, with the glass fibres shown as small spots with a slightly lighter grey value. The large black spots are enclosed voids which were not filled with epoxy during embedding of the material.

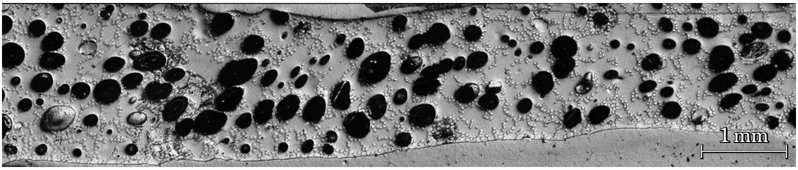

Figure 11.3: Polished cross-section of a unidirectional glass/polycarbonate bicomponent fibre preform with a mean glass volume fraction of 0.15 after subjection to a temperature of 300 °C and subsequent cooling without applying external pressure.

It is clear that after the heating step but prior to consolidation, a large quantity of air is still distributed within the preform. It also seems that a considerable amount thereof is enclosed within the matrix, forming the air pockets discussed in section 10.1. It is remarkable that for this preform containing a large amount of matrix, the coalescence of the sheaths extends over the scale of a few filaments and forms larger accumulations of fibres, which apparently do not contain any voids between the filaments.

In comparison to the theoretical discussion presented in chapter 10, it can therefore be concluded that the molten matrix re-distributes over longer distances than assumed. It is asserted that this happens due to the fact that upon melting of the sheaths, the fibres themselves are likely to move and re-arrange themselves because of minute loads induced by the mounting of the sample, by gravity, and by the flow of the matrix. After all, the movements of both matrix melt and fibres are interdependent. It seems that their interactions benefit the formation of fewer but larger voids, probably mainly driven by the surface tension of the melt. This would potentially be an issue for low-pressure consolidation methods without vacuum assistance, but as discussed in section 10.1.3, the levels of consolidation pressure available in press processes exceed the issues of void size. The following chapter expands on this discussion by providing experimental proof of the consolidation quality achieved in stamp forming of bicomponent fibre preforms.

12

STAMP FORMING EXPERIMENTS

This chapter presents an experimental investigation into the use of glass/polycarbonate bicomponent fibres for stamp forming, following the motivation presented in part I of this thesis. A two-level full factorial parameter study is presented which varies the initial preform temperature, the press temperature, and the hold time inside the press, and analyses the influence of these changes on the void content in the resulting unidirectional laminate. Furthermore, trials with alternating cross-ply layups were conducted to assess whether a change in fibre orientation would influence the local laminate quality. The results prove that flexible preforms made from hybrid bicomponent fibres can be consolidated with rapid stamp forming without the need for pre-consolidation, achieving void contents below 0.7 % and cycle times as low as 12 s.

12.1 Materials and methods

All samples of glass/polycarbonate bicomponent fibres processed within this study were spun, coated, and measured for their glass volume fraction following the method presented in section 11.1.

12.1.1 Stamp forming of the samples

The bicomponent fibre specimens were cut and arranged into unidirectional strips of 40 mm width, ~ 100 mm length, and a thickness corresponding to 1 mm after consolidation. During the stamp-forming experiments, the samples were taped onto a steel frame and placed in a heating chamber (Binder FED 56) for 20 min to ensure a homogeneous initial temperature. For the parameter study, a unidirectional arrangement with a total thickness of 1 mm after consolidation was maintained. For the cross-ply trials, layups with total layer numbers of 4, 5 and 6 and alternating orientation $[0°, 90°, 0°, \ldots]$ were used. After heating, the chamber door was opened and the sample and frame were transferred to a hydraulic hot press (Fontijne TP 400), which was closed immediately after the transfer. This transfer was monitored via audio recordings to determine the exact duration from the opening of the heating chamber until the full closure of the press (Table 12.1). The press tool (Fig. 12.1) suspended the sample above the lower platen until the press reached a clearance of 19 mm, at which point the upper platen pushed the material towards the lower one. Both platens are 24 mm thick and made from polyether ether ketone (PEEK). The press was closed at a rate of $16\,\mathrm{mm\,s^{-1}}$ and consolidated the material with a force of 30 kN distributed over a surface of 40 mm by 50 mm, limited by the width of the specimen and the platens, respectively. Following a previously set holding time t_h, informed by the solution to the heat transfer problem described in section 10.3, the press was opened and the consolidated sample was retrieved. For the parameter study, the initial temperature, the temperature of the press, and the holding time inside the press were varied according to the design of experiment described in Table 12.1. To process the cross-ply layups, an initial temperature of 280 °C and a press temperature of 145 °C were used. The holding time was varied such that the thickest sample had just solidified in reference to the predictions of the thermal simulation (see section 10.3). Thinner cross-ply samples were subjected to intentionally shorter holding times in the press (shown in Table 12.2) to assess whether premature demoulding has a significant effect on laminate quality.

12.1.2 Imaging

The consolidated specimens were cut transversely to the fibre direction, mounted in epoxy (Struers SpeciFix), polished, and sputter-coated with 3 nm of platinum (Safematic CCU-010). The prepared samples were imaged in a Zeiss LEO 1530 (Gemini column) scanning electron microscope. For the parameter study, two separate cross-sections of each stamp formed sample were imaged at five positions distributed along

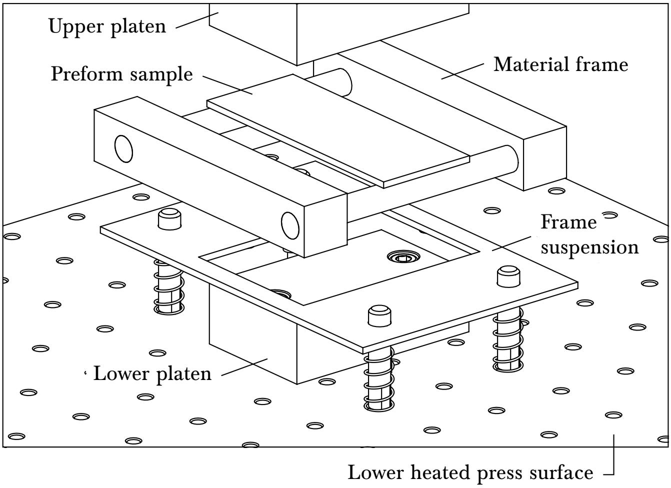

Figure 12.1: Trimetric view of the tooling setup used in the stamp forming experiments in its open configuration. The preform sample is taped onto the material frame, which is laid onto the suspension after transferring the sample from the heating chamber to the press. (Here, the frame is shown in floating position above the suspension.) The two platens which consolidate the preform upon closing of the press are heated by conduction from the heated press surfaces, which are kept at a constant temperature T_p during the experiment. The upper press surface is not shown here.

their width. The void content of the samples was measured via binarization and segmentation of the obtained micrographs. The threshold for binarization was chosen individually per image and segmentation was performed by hand, such that areas corresponding to voids in the matrix, cracks in the matrix, and microcracks between the fibres and the matrix were counted. For the analysis of the cross-ply sample micrographs, only the layers with fibre orientation perpendicular to the imaged plane were analysed.

12.2 Results and discussion

12.2.1 Results of the parameter study

The cross-sectional micrographs of the consolidated plates generally show a high consolidation quality. A representative selection of the images, shown in Fig. 12.2, illustrates the observed features. In Fig. 12.2, the micrograph of sample I shows no visible flaws. Samples II(a) and IV show microcracking at the interface between fibres and matrix. It is asserted that this was not caused by the entrapment of air, but is rather a result of the combined local stress state induced by the thermal cycle and the press which exceeded the interfacial strength at some point after

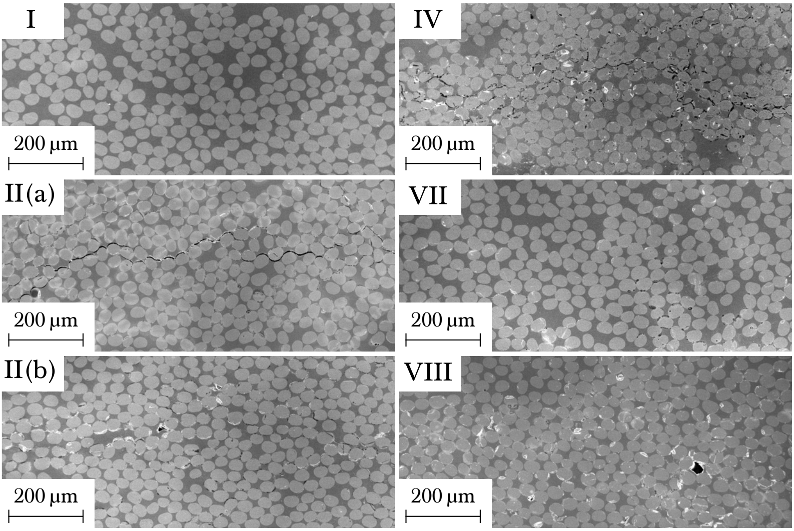

Figure 12.2: Representative scanning electron micrographs of polished specimens revealing the laminate quality of the stamp formed samples. Samples II(a) and IV show microcracking, while sample VII shows only minimal flaws. Voids resulting from entrapped air and/or a jammed fibre arrangement can be seen in samples II(b) and VIII. Sample I exhibits no visible flaws in this micrograph.

solidification. Nevertheless, these microcracks are clearly a flaw in the mechanical integrity of the laminate and were therefore also counted as contributors to the measured void content. Sample VII exhibits only minimal flaws in the shown micrograph. Finally, the micrographs shown for samples II(b) and VIII provide examples of voids which seem to have been caused by the entrapment of air. However, only a few voids of this type have been found in the complete set of micrographs, while the majority of voids are attributed to microcracks at the fibre-matrix interface.

The measured void contents Φ for each sample as obtained from the image analysis are given in Table 12.1, next to the corresponding parameters during stamp forming and the fibre volume fractions v_f of the preform measured via thermogravimetric analysis. All preforms used in this study exhibited a similar fibre volume fraction of 0.68 to 0.69 prior to stamp forming and their behaviour during processing was therefore unaffected by changes in relative amounts of constituent materials. During the experiments, the preforms were subjected to transfer times t_t in the range of 7 s to 10 s, with an average time of ~ 9 s. These differences are expected to have led to slight variations in the preform temperatures at the times the press was closed. However, the heat transfer during transport is governed by losses to air, which is

Table 12.1: Stamp-formed samples with their corresponding settings for initial temperature T_0, press temperature T_p, and holding time inside the press t_h, as well as their measured transfer time t_t, fibre volume fraction v_f, and void content Φ.

Sample	T_0	T_p	t_h	t_t	v_f	Φ
I	300 °C	120 °C	12 s	9 s	0.69	0.04 %
II	300 °C	120 °C	5 s	9 s	0.68	0.32 %
III	280 °C	120 °C	5 s	10 s	0.68	0.17 %
IV	280 °C	120 °C	12 s	9 s	0.68	0.10 %
V	280 °C	145 °C	5 s	9 s	0.68	0.18 %
VI	280 °C	145 °C	12 s	10 s	0.68	0.07 %
VII	300 °C	145 °C	12 s	8 s	0.69	0.03 %
VIII	300 °C	145 °C	5 s	7 s	0.68	0.20 %
Avg.	-	-	-	9 s	0.68	0.14 %

significantly slower than the conductive heat transfer inside the closed press. These variations are therefore not seen as critical.

The main effects of the stamp forming parameters on the consolidation quality of the final laminates are shown in Fig. 12.3. The solid dots show the actual void content measurements plotted against the corresponding parameter level, while the connected circles show the mean void contents of the subsets processed at the same levels of each parameter, respectively. The trends of the mean values point to a decrease in void content when increasing the press temperature T_p and when prolonging the hold time inside the press t_h. It is also evident that for the chosen parameter levels, a prolonged hold time always has a significant influence on the void content, while changes in either the press temperature or the initial preform temperature T_0 have a smaller effect. The dominance of the influence of t_h over the influence of T_0 is further illustrated by the fact that all measurements lying above the average values plotted for both levels of T_0 were processed at the lower level of t_h, and all measurements lying below the average values for T_0 were processed at the higher level of t_h.

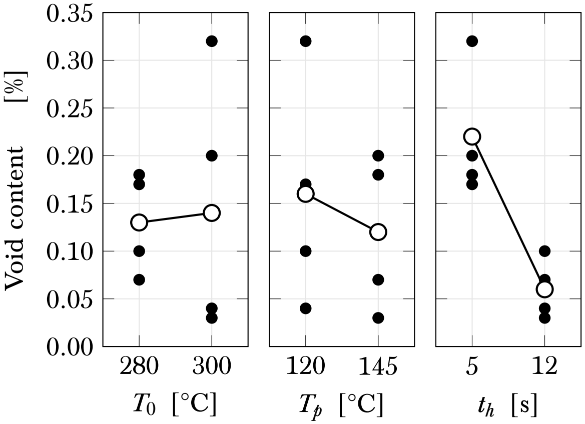

Figure 12.3: Main effects plot of the measured void content Φ for variations of the initial temperature T_0 (left); the press temperature T_p (center); and the holding time inside the press t_h (right). The lines indicate the variation of the mean values, while the solid dots represent the actual data.

Seeing as most observed voids are actually microcracks, it makes sense that a lower void content is achieved if the material in the press is cooled at a lower rate and over a longer period of time. A higher press temperature automatically causes a lower cooling rate, which allows more time for the matrix material to rearrange itself in its fluid state and for stresses induced by thermal shrinkage to relax even during solidification. However, even prolonging the hold time at the same temperature settings seems to lower the void content. This effect is attributed to the fact that if the press is opened too early, thermally induced stresses might not yet have sufficiently relaxed and the matrix, being warmer at the time the press is opened, might not yet have reached its full strength. This combination of higher residual stresses and lower strength at the moment of demoulding is a possible explanation for a higher occurrence of cracking, but would require further investigation to be proven.

Finally, the measured void contents of all samples are very low, namely less than half a percent. Even sample VIII, which was processed with a cycle time of 12 s, only contains 0.2 % voids. It is expected that in an automated process, this cycle time could be cut even more by increasing the material transfer speed. These results highlight the hypothesized ease of consolidating preforms made from hybrid bicomponent fibres and give proof that this novel type of flexible, hybrid intermediate material can be directly converted into a structural component via rapid stamp forming, without the need for pre-consolidation.

12.2.2 Results of the cross-ply trials

A representative selection of micrographs taken from the stamp formed cross-ply layups is given in Fig. 12.4, which shows one micrograph per sample pressed. All three images show significant amounts of broken fibres in the 90° layers. The fact that these faults seem to be located at the ends of fibres which crossed the imaged plane and that part of these fibres is missing points to the conclusion that these blemishes were introduced during grinding and polishing of the embedded specimens. It is therefore assumed that there was no fibre breakage of this extent present after the stamp forming step. Still, this observation raises the question about the level of adhesive strength between fibre and matrix. It seems that in this case, the polycarbonate used does not yield strong interactions with the aluminium-borosilicate fibres without the implementation of a

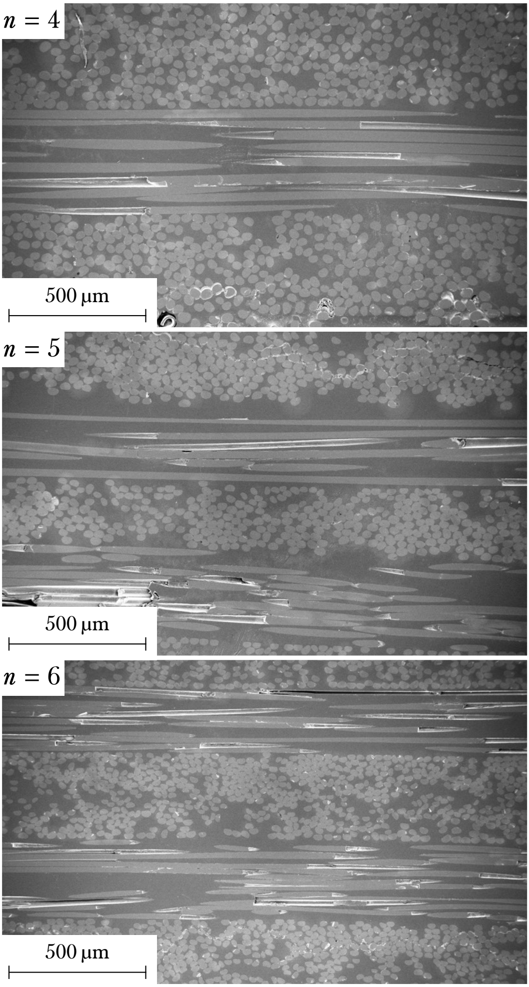

Figure 12.4:

Representative scanning electron micrographs of polished specimens revealing the laminate quality of the stamp formed cross-ply layups. The bulk of the void content is present as microcracks in the outer layers, e.g. in the bottom layers of samples $n = 4$ and $n = 6$ or in the top layer of sample $n = 5$.

sizing compound at the interface, even though proof of this assessment requires more specific investigation.

The presence of the aforementioned blemishes hinders a fair assessment of the void content within the 90° layers based on the available micrographs. The void content Φ was therefore measured in the 0° layers only, by dividing the total area of identified voids by the total area of only these layers. The latter was measured as the envelope of all fibres shown within that same layer, giving a conservative measure for the measured void content. The numerical results are presented in Table 12.2, together with the necessary holding time inside the press as predicted by the simulation, $t_{h,\mathrm{sim}}$, the actual holding time inside the press used in the trials, t_h, the measured fibre volume fraction v_f, and the measured thickness after consolidation h. The comparison between the holding times inside the press as predicted by the simulation and the actual time used in the experiments suggests that a premature opening of the press leads to a higher void content. While at first this might suggest that the cause for higher void content in this case are de-consolidation mechanisms in the not yet solidified sections of the laminate, the micrographs do not show sufficient voids in the middle regions of the laminate to support this claim. The majority of voids are located in the outer layers and are present in the form of microcracks. This circumstance provides further evidence in support of the points raised in the discussion of the parameter study results: longer hold times might allow for more relaxation of residual stresses induced by the press and by thermal shrinkage. Furthermore, the lower temperatures reached after longer hold times might result in slightly higher matrix strength at the time the press is opened, possibly making the difference between residual

Table 12.2: Stamp-formed cross-ply samples with their corresponding number of layers n, predicted necessary holding time inside the press $t_{h,\mathrm{sim}}$, the actual holding time inside the press t_h, and their measured fibre volume fraction v_f, thickness after consolidation h, and void content Φ.

n	Layup	$t_{h,\mathrm{sim}}$	t_h	v_f	h	Φ
4	[0°, 90°, 0°, 90°]	23 s	15 s	0.52	1.55 mm	0.46 %
5	[0°, 90°, 0°, 90°, 0°]	33 s	30 s	0.60	1.80 mm	0.68 %
6	[0°, 90°, 0°, 90°, 0°, 90°]	39 s	40 s	0.52	1.94 mm	0.25 %

stresses leading to microcracks or not. Again, while this mechanism is presented here as a possible explanation, actual proof requires further investigation with a deeper focus on this issue.

Finally, the laminate qualities of the cross-ply layups does not differ significantly from the ones observed in the parameter study. Any faults in the microstructure are found to be localized in the outer layers and intentional premature opening of the press (in reference to the thermal simulation) does not increase the void content to worrisome levels, with the largest observed value being 0.68 % in the sample with 5 layers. This demonstrates that, as expected, the quality of stamp formed hybrid bicomponent fibre preforms is not significantly affected by changes in layer orientation or overall layup thickness, when accounting for increased cooling time in the latter case.

12.3 Conclusion

The presented experimental study demonstrates the high suitability of hybrid bicomponent fibres as preform materials for rapid part manufacturing processes. The results provide evidence that the entrapment of air in the laminate is an issue of minor significance and that voids found in the stamp formed laminates primarily present themselves in the form of microcracks at the fibre-matrix interface. The parameter study shows that such cracks can be avoided by realizing a sufficiently low cooling rate and a long holding time inside the press. The quality of all laminates realized within the presented work is assessed as very high, seeing as all samples exhibit void contents lower than 0.7 %. Processing laminates with a consolidated thickness of 1 mm, cycle times ranging from 12 s to 22 s were achieved. Thicker laminates with cross-ply layups required longer holding times in the press to solidify sufficiently, but did not show significant effects on void content in comparison to unidirectional samples. It is expected that the total cycle time can be further reduced in an automated production environment, where higher material transfer speeds can be realized. Further reductions are possible by extended empirical trials which aim at the minimization of the holding time inside the press without exceeding a predetermined void content in the realized laminate.

Part IV

CONCLUSION

13

CONCLUDING REMARKS

The research presented in this thesis highlights the advantages of preform hybridization early in the value chain of fibre-reinforced thermoplastic polymer composites. The proposed concept encompasses the fabrication and stamp forming of intermediate materials containing hybrid bicomponent fibres, which combine individual reinforcing filaments with thermoplastic polymer claddings. Rovings of such fibres do not only provide a perfect distribution of both constituent materials already at the preforming stages, but they altogether circumvent any Darcian impregnation flows throughout the entire processing chain. It is therefore clear that the conversion of this novel type of preform into a consolidated laminate outperforms any thermoplastic melt impregnation method, be it in part production or during the fabrication of a pre-impregnated intermediate material.

The experimental studies reported in this thesis focus on both the fabrication of such bicomponent fibres for use in advanced fibre-reinforced polymer composite structures and on their processing for laminate production using the rapid stamp forming method. The following sections highlight key findings and conclusions drawn from these investigations.

13.1 Hybrid bicomponent fibre fabrication

While the proposed concept of processing hybrid bicomponent fibres into continuous fibre-reinforced laminates is an established idea,[30] the fabrication thereof has long eluded public knowledge.[44,62] It is asserted that the melt-spinning of glass, in particular the direct roving process, presents an ideal base for first experimental trials for manufacturing continuous bicomponent fibres for structural purposes. During the direct roving process, the individual filaments are drawn from geometrically separate nozzles before being bundled, presenting an opportunity to insert an in-line coating stage for the application of a thermoplastic polymer sheath. The challenge in doing so presents itself in the form of the high velocities at which glass fibres can be spun to a fine enough diameter to carry the high strength required in lightweight composite structures. This thesis therefore reports on investigations into the suitability of different coating methods for the implementation into the direct roving process.

A theoretical treatment on the use of solution dip-coating and supported by experimental data concludes that it is possible to fabricate glass/thermoplastic polymer bicomponent fibres by drawing the continuously spun filaments through a dilute solution of the polymer followed by drying. This requires the use of a solvent with low viscosity, high volatility, and low risk of ignition or explosion. Trichloromethane presents an ideal basis for such a solvent, primarily because of its low boiling point and because it is inflammable and does not form explosive mixtures with air. Furthermore, the in-line integration of dip-coating into glass melt spinning requires a rather low glass flow rate compared to industrial settings, if thin fibres with high strength are to be spun. The theoretical study found that an overlap of fibre velocities for both spinning and coating of the filaments exists over a range from ~$0.38\,\mathrm{m\,s^{-1}}$ to $1.15\,\mathrm{m\,s^{-1}}$. This window is limited on the lower end by the achievable speed at which glass fibres thinner than 20 µm can still be spun and on the upper end by the dip-coating process when considering solutions of poly(ester-amide) in trichloromethane. Coating experiments yielded bicomponent monofilaments with glass volume fractions as low as 0.56, which are already suitable for high-performance structural composites, therefore proving the validity of the chosen approach and providing a first feasible method for the successful fabrication of hybrid bicomponent fibres based on glass cores.

One key finding of the dip-coating investigation is that even the melt viscosity of low-molecular-weight polymers is on an order of magnitude too high to be applied in a coating stage with fibre velocities useful for the direct roving process. As an alternative to polymer solutions for the purposes of lowering the coating fluid's viscosity, an approach based on a sparsely nanofilled polymer melt was investigated. A variety of studies report that the dispersion of a small but targeted amount of nanoparticles in a polymer can lower its apparent melt viscosity by as much as one order of magnitude,[78–81,85] contrary to the prediction of Einstein's equation.[82] A series of experimental trials was launched to gauge the potential of this approach for the fabrication of bicomponent fibres. It was found that for a poly(ester-amide) melt filled with fumed silica nanoparticles of an average primary particle size of ~ 24 nm, a relative reduction of melt viscosity of 49 % is achieved at a particle concentration of 0.23 vol% and using a mixture of 50 vol% ethanol, 5 vol% 1-decanol and 45 vol% trichloromethane to dissolve the polymer and disperse the silica. Experiments in which glass fibres were dip-coated in both the sparsely nanofilled and the pure polymer melt show that the nanofilling approach allows to double the coating velocity while maintaining the same coating thickness, as is predicted by the Landau-Levich-Derjaguin relationship. It is therefore expected that the use of more sophisticated methods[81,85] to achieve a better particle dispersion would lead to a higher increase of achievable coating velocities. It is concluded that while the opportunities of polymer melt viscosity reduction through nanofilling can not produce an overlap of processing windows for dip-coating and glass melt spinning, the approach provides a valuable tuning mechanism for other melt-based processes.

To expand on the results of the solution dip-coating study, a modified approach based on the use of a kiss-roll was proposed. In this method, the fibre is drawn over a rotating roll which is partially immersed in the polymer solution, withdrawing a thin film thereof and transferring it onto the fibre. This method is already established in glass fibre production for the application of sizing solutions. However, using a kiss-roll to apply a comparatively thick coating which has to solidify prior to bundling of the filaments requires more accurate knowledge on the sensitivity of the resulting coating to the process parameters. An experimental parameter study investigated the effects of roll radius, peripheral velocity, and polymer concentration in the coating solution on both the resulting glass volume fraction of the bicomponent fibre and its sensitivity to changes in fibre velocity. It was found that higher fibre velocities, and therefore thinner filaments, are realized using more diluted solutions while increasing both roll radius and velocity. A coating stage was designed based on these results and implemented into a glass monofilament spinning machine. The establishment of this pilot plant provides proof that bicomponent fibres with advantageous characteristics for the production of advanced composite structures can be manufactured by solution kiss-roll coating in-line with glass melt-spinning. Furthermore, the experimental characterization of the kiss-roll method was continued at higher fibre velocities. It was found that upon increasing the fibre velocity, the coating thickness first increases as well, before reaching a maximum value which depends on the various process parameters. Further increase of the fibre velocity then leads to an asymptotic reduction of the film thickness deposited on the fibre. It is concluded that maintaining constant settings other than the fibre velocity results in a steady film thickness on the kiss-roll and therefore a constant supply of fluid to the fibre. As long as this supply is sufficiently large, the capillarity of the flow at the fibre governs the entrainment of the fluid layer and therefore the coating thickness still depends on the fibre velocity. However, the supply of fluid on the roll limits this behaviour at higher fibre velocities, where the fibre empties the fluid layer on the roll, but distributes the supplied solution over a longer distance on the fibre. In between these regions, an equilibrium exists where the entrainment of fluid on the fibre caused by the capillarity of the flow equals the supply provided by the kiss-roll. These findings provide further insights into the fluid dynamics at play in this approach and motivate future investigations into the optimization of the process design for the purposes of producing high volumes of hybrid bicomponent fibres with high performance at low cost.

13.2 Processing hybrid bicomponent fibres

The commissioning of the pilot plant for the continuous spinning and coating of a glass monofilament enabled the fabrication of sample materials for further investigation. Glass fibres coated with polycarbonate were arranged into unidirectional preforms and processed in evacuated compression moulding and stamp forming. Prior to conducting the trials themselves, a selection of phenomena occurring during these steps were discussed based on theoretical approaches. The following paragraphs discuss the collected conclusions drawn from these studies and place them in relation to the hypotheses on the processing of hybrid bicomponent fibres outlined in the introduction (section 3.2).

Hypothesis 1 *Preforms made from hybrid bicomponent fibres can be stamp formed with cycle times similar to those of pre-consolidated blanks.*

Pre-consolidated intermediate materials like organosheets are commonly stamp formed with holding times around half a minute. For example, Wakeman et al. report on trials with consolidated laminate thicknesses of ~ 3 mm and holding times from 20 s to 30 s, resulting in void contents below 1 %.[34] For comparison, this study reports equal levels of void content (< 0.7 %) for bicomponent fibre preforms stamp formed with holding times from 5 s to 12 s for final laminate thicknesses of 1 mm and with holding times from 15 s to 40 s for final laminate thicknesses of 1.5 mm to 2 mm. However, these values are not optimized and were defined for first experimental trials which already yielded excellent laminate quality throughout all parameter combinations. It is therefore concluded that bicomponent fibre preforms can certainly be stamp formed with holding times in the same range as those used to process organosheets. Further experimental investigation is required to determine the exact boundary of the minimum achievable cycle times, also considering different laminate thicknesses.

Hypothesis 2 *The void content of laminates stamp formed from hybrid bicomponent fibre preforms is greatly influenced by sintering mechanisms and the removal and/or collapse of air pockets.*

The cross-sectional micrograph of a heated bicomponent fibre preform which was never subjected to external loads other than gravitation, shown in Fig. 11.3, illustrates that prior to stamping, there is indeed a large amount of air trapped within the matrix. More notably, the tested sample exhibits almost exclusively large air pockets and only few, if any voids with similar size as the reinforcing fibres. However, it could be shown with a quick calculation that the pressures available in hydraulic presses significantly supersede the total internal void pressures which commonly occur in polymer composite processes. The polished specimens of consolidated samples all exhibit void contents below 0.7 %, with microcracks located at the fibre-matrix interfaces being the major contributor and only very few voids within the matrix itself being visible. These experimental results support the conclusion that void collapse is not a significant issue in stamp forming of bicomponent fibres. Furthermore, polymer sintering mechanisms classically depend on the diffusion and entanglement of the macromolecules across newly closed interfaces. A simplified treatment of this issue based on reptation theory concludes that at the temperatures used in the presented stamp forming study, the reptation times of the polymer chains are multiple orders of magnitude shorter than the time it takes for the material to cool below itse glass transition temperature. It can therefore be assumed that autohesion of the matrix in the regions of collapsed voids is complete long before the polymer solidifies. Due to the large difference between reptation time and holding time in the press found in the presented experiments, it is expected that this conclusion holds true even for temperature settings and holding times which are optimized for shortest cycle times.

Overall, it is concluded that the concept of hybrid bicomponent fibres as a novel type of preform provides enormous advantages for manufacturing continuous fibre-reinforced thermoplastic polymer composites. Employing the kiss-roll coating approach in-line with the direct roving process results in a fast and scalable production method which is able to supply large volumes. Furthermore, this innovative and efficiently produced material can be converted into consolidated laminates using the most cost-efficient state-of-the-art methods, such as rapid stamp forming. In combination, this proposed value chain offers a first opportunity for the production of continuous fibre-reinforced polymer composites without relying on Darcian impregnation flows anywhere between fibre formation and part production. The research presented in this thesis provides experimental proof for these claims and has established pilot equipment for the continuous spinning of glass/thermoplastic polymer bicomponent fibres, bringing this potentially disruptive technology closer to reality.

14

OUTLOOK

> *We live on an island surrounded by a sea of ignorance. As our island of knowledge grows, so does the shore of our ignorance.*
>
> John Archibald Wheeler

As can be expected from any efforts in the realm of basic research, this thesis does not only add terrain to Prof. Wheeler's proverbial island of knowledge, but also increases the length of its shores. This last chapter shall serve as a lookout into the ocean around that island and outline what sediments can be expected to further extend its reach.

The approach of solvent-coating in-line with glass melt spinning provides a promising first approach which has been proven to yield hybrid bicomponent fibres (BCF) useful for the production of structural composites. As next steps in the further development of this technology, the established pilot plant should be scaled up from spinning a monofilament to producing an actual roving comprised of a multitude of fibres. This has implications for the coating stage, which exploits the dynamics of free-surface flow. It is crucial to ensure that coating multiple filaments in parallel does not lead to a coalescence of the sheaths already at this stage, otherwise the flexibility of the resulting yarn is lost. Optimizing the design of the coating stage for spatial efficiency while ensuring the application of separated coatings requires specific investigation. Similarly, further scaling of the production would profit from efforts to automate the coating process in terms of the yielded glass volume fraction and to optimize the coating parameters for cost- and energy-efficiency while ensuring constant quality of the spun material. This can be achieved through the implementation of suitable sensors which ideally monitor the spun fibre diameter, deposited film thickness, and coating fluid properties and control parameters like roll velocity or polymer concentration through corresponding actuators. Furthermore, special attention is to be paid to the strength of the fibre-matrix interface. The approach presented in this research has so far neglected the modification of said interface through sizing agents, surface activation, or other suitable methods. While the application of tensile or compressive loads perfectly aligned with the reinforcing fibres does not significantly depend on interfacial strength, a laminate's ability to withstand shear or transverse tension can be highly affected by this property. The observation of microcracking within the stamp formed specimens presented in chapter 12 further motivates future efforts to incorporate measures to improve fibre-matrix adhesion in glass/thermoplastic polymer BCF.

On the matter of the constituent materials themselves, the presented studies focus on the coating of aluminium borosilicate glass with either poly(ester-amide) or polycarbonate. Extending this range of materials is possible within the same method, as other amorphous polymers like acrylonitrile butadiene styrene (ABS), polyetherimide (PEI), poly(methyl methacrylate) (PMMA), or polystyrene (PS) are soluble in trichloromethane or highly concentrated mixtures with other solvents. However, the range of polymers to be used in the coating process could be significantly expanded if an alternative application method is found which does not rely on the use of solvents. Furthermore, the use of alternative reinforcing materials is certainly of interest for a variety of applications. While other glass compositions or minerals like basalt can easily be processed in the direct roving process, the fabrication of BCF with a core comprised of highly stiff and strong stretched polymer fibres, e.g. aramid or ultra-high-molecular-weight polyethylene, or even carbon fibres requires completely alternate approaches. Chapter 4 discusses advantages of the chosen approach, but also outlines methods tied to the processing of alternative materials, providing potential starting points to investigate their use for BCF production.

Seeing as this study is in part motivated by the efforts of the Swiss Competence Center for Energy Research (SCCER) Efficient Technologies and Systems for Mobility, the manufacturing of BCF rovings and higher level intermediate materials comprised thereof requires ecological assessment as well. The benefits of high volume stamp forming combined with an efficiently manufactured BCF preform certainly carry the potential to reduce overall production costs in lightweight structures for mobility systems. However, this positive impact on the reduced energy demand in vehicles shall not be offset by increased emissions and unsustainable practices during production when compared to prior established value chains. These aspects of the technology proposed and developed in the presented work are currently under ongoing investigation within the SCCER Mobility research program. As further cases for the use of BCF processes in the mobility sector will be discussed, the evaluation of the possible ecological impact of said use shall become an integral component of these discussions.

Staying with the challenges related to part production, the further processing of rovings comprised of hybrid bicomponent fibres does not solely encompass the direct stamping of flat unidirectional layups to produce end-use structures. This is not what the presented study suggests. Rather, stamp forming of three-dimensional components requires drapeable preforms, such as woven textiles or non-crimp fabrics. The question then arises whether BCF bundles behave similarly to sized glass rovings during weaving, stitching, or even other textile processes like braiding or knitting. In particular, potential issues related to fraying, fibre breakage, or loss of coatings due to frictional loads require special attention and should be assessed in empirical trials. Furthermore, the mechanisms related to draping of a BCF preform in the molten state might exhibit qualitative differences to the behaviour known from organosheets, commingled yarn textiles, or other hybrid intermediate materials. One possibility to leverage potential issues related to draping in the molten state is certainly the fact that the flexibility of BCF rovings enables draping at room-temperature. This might prove beneficial for the production of complex geometries, particularly when using moulds which close from multiple sides and considering that other flexible preform types can not be stamp formed without pre-consolidation. Finally, the intimate mixture of constituent materials in BCF can also be exploited in entirely different process families. For example, additive manufacturing methods akin to fused deposition modelling could employ BCF filaments to directly print composites with aligned fibres, similarly to the continuous lattice fabrication process.[105] In general, methods which exploit the deposition of fibres aligned with the loads in the final part could benefit from bicomponent fibre technology for the purposes of miniaturization, e.g. for the fabrication of micromechanical devices in sensory or medical equipment or for watchmaking.

It is yet to be shown which end-use applications may benefit most from the use of bicomponent fibre preforms. The benefits already outlined for press processes can serve a great many industries, not only the automotive sector. The potential cost- and energy-savings during part production might also prove valuable for the realization of energy-efficient lightweight structures in the fields of aviation, travel goods, packaging, sports equipment, or robotics. Furthermore, the presented approach for the fabrication of BCF carries potential to incorporate functionalized materials in the coatings, opening an entirely new direction for further research and development.

It seems that hybrid bicomponent fibres carry significant potential for various uses which are yet to be explored and exploited. It is the author's sincere hope that this work may provide a basis to launch further investigations and to stir both concepts of exploitation as well as criticism of the developed methods, such that the idea of hybrid bicomponent fibres may find its way into many innovative minds and lead to technological advances for the economical and ecological betterment of humankind. While this future is in no way certain, one can only hope that the soil this thesis deposits on the beaches of the island of knowledge is put at the right place, at the right time, and that it is firmly packed, so we may conquer new shores in the battle against the ocean of ignorance.

BIBLIOGRAPHY

[1] Swiss Federal Office for the Environment FOEN. Swiss green house gas emissions 2016, 2018.

[2] Isaac Newton. *Philosophiæ Naturalis Principia Mathematica*. London, first edition, 1687.

[3] Brian Cox. *Mobility and the Energy Transition: A Life Cycle Assessment of Swiss Passenger Transport Technologies including Developments until 2050*. Doctoral thesis, ETH Zürich, 2018.

[4] Frédéric Reux, Aïcha Mikdam, Marie-Hélè Corbin, Franck Glowacz, Antoine Morel, and Archal Shah. Overview of the Global Composite Market 2018-2023: Continuing Growth. *JEC Composites Magazine*, 1(127):34–42, March 2019.

[5] Elmar Witten, Volker Mathes, Michael Sauer, and Michael Kühnel. Composites-Marktbericht 2018: Marktentwicklungen, Trends, Ausblicke und Herausforderungen. Technical report, AVK Federation of Reinforced Plastics and Carbon Composites, November 2018.

[6] Jochen Kopp. BMW i – Automotive CFRP-Production and Potentials for Thermoplastic FRP. In *2nd International Conference and Exhibition on Thermoplastic Composites (ITHEC 2014)*, Bremen, October 2014.

[7] Matt Gasnier. World Full Year 2013: Discover the Top 1000 best-selling models! *https://bestsellingcarsblog.com/2014/07/world-full-year-2013-discover-the-top-1147-best-selling-models*, July 2014.

[8] BMW Group Press Release. BMW Group sells more than 2 million vehicles in 2014. *https://www.press.bmwgroup.com/global/article/detail/T0199942EN/bmw-group-sells-more-than-2-million-vehicles-in-2014*, January 2015.

[9] BMW Group Press Release. BMW Group achieves fifth consecutive record sales year. *https://www.press.bmwgroup.com/global/article/detail/T0249765EN/bmw-group-achieves-fifth-consecutive-record-sales-year*, January 2016.

[10] Jeff Cobb. Tesla Model S Is World's Best-selling Plug-in Car For Second Year In A Row. *https://www.hybridcars.com/tesla-model-s-is-worlds-best-selling-plug-in-car-for-second-year-in-a-row*, January 2017.

[11] BMW Group Press Release. Record sales for BMW Group worldwide during 2017 while it boosts the Premium car market in Mexico, Latin America and the Caribbean. *https://www.press.bmwgroup.com/latin-america-caribbean/article/detail/T0278223EN/record-sales-for-bmw-group-worldwide-during-2017-while-it-boosts-the-premium-car-market-in-mexico-latin-america-and-the-caribbean*, January 2018.

[12] BMW Group Press Release. BMW Group remains world's leading premium automotive company in 2018. *https://www.press.bmwgroup.com/global/article/detail/T0289883EN/bmw-group-remains-world%E2%80%99s-leading-premium-automotive-company-in-2018*, January 2019.

[13] Benjamin Preston. BMW Unveils i3 Electric Car. *https://wheels.blogs.nytimes.com/2013/07/29/bmw-unveils-i3-electric-car*, July 2013.

[14] Green Car Congress. US MSRP for BMW i3 EV will be $41,350, before incentives. *https://www.greencarcongress.com/2013/07/i3-20130722.html*, July 2013.

[15] Jay Cole. BMW Sets Lease Price On i3 At $565 In The UK (£369) – Priced from £25,680. *https://insideevs.com/bmw-sets-lease-price-on-i3-at-565-in-the-uk-369-priced-from-25680*, July 2013.

[16] Ginger Gardiner. Is the BMW 7 Series the future of autocomposites? *https://www.compositesworld.com/articles/is-the-bmw-7-series-the-future-of-autocomposites*, October 2016.

[17] BMW Group. Annual Report 2018. *https://annual-report2018.bmwgroup.com/build/dl/en/Annual_Report_2018.pdf*, March 2019.

[18] BMW Group Press Release. The All-New BMW 7 Series. *https://www.press.bmwgroup.com/usa/article/detail/T0221442EN_US/the-all-new-bmw-7-series*, June 2015.

[19] Nickel. Average Price of a New Car? *https://www.forbes.com/sites/moneybuilder/2012/05/10/average-price-of-a-new-car/#2b0ecb8b7f92*, May 2012.

[20] CRC Press. Polymers: A Property Database. *http://www.polymersdatabase.com*, June 2015.

[21] Henry Darcy. *Les fontaines publiques de la ville de Dijon: exposition et application des principes à suivre et des formules à employer dans les questions de distribution d'eau.* Victor Dalmont, Libraire des corps impériaux des ponts et chaussées et des mines, Paris, 1856.

[22] Krishna M. Pillai and Kamel Hooman. *An Introduction to Modeling Flows in Porous Media, in: Wicking in Porous Materials: Traditional and Modern Modeling Approaches*, chapter 4. CRC Press, Boca Raton, 2013.

[23] Christoph Schneeberger, Joanna C.H. Wong, and Paolo Ermanni. Hybrid bicomponent fibres for thermoplastic composite preforms. *Composites Part A: Applied Science and Manufacturing*, 103:69–73, 2017.

[24] M. J. Folkes and S. T. Hardwick. The mechanical properties of glass/polypropylene multilayer laminates. *Journal of Materials Science*, 25(5):2598–2606, 1990.

[25] C. Houphouët-Boigny, C. J. G. Plummer, M. D. Wakeman, and J.-A. E. Månson. Towards textile-based fiber-reinforced thermoplastic nanocomposites: Melt spun polypropylene-montmorillonite nanocomposite fibers. *Polymer Engineering & Science*, 47(7):1122–1132, 2007.

[26] Niccolo Pini, Chiara Zaniboni, Stephan Busato, and Paolo Ermanni. Perspectives for Reactive Molding of PPA as Matrix for High-performance Composite Materials. *Journal of Thermoplastic Composite Materials*, 19(2):207–216, 2006.

[27] Roland A. Ganga. Flexible composite material and process for producing same, US Patent 4614678, 1986.

[28] N. Svensson, R. Shishoo, and M. Gilchrist. Manufacturing of Thermoplastic Composites from Commingled Yarns-A Review. *Journal of Thermoplastic Composite Materials*, 11(1):22–56, 1998.

[29] U. I. Thomann and P. Ermanni. The Influence of Yarn Structure and Processing Conditions on the Laminate Quality of Stamp-formed Carbon and Thermoplastic Polymer Fiber Commingled Yarns. *Journal of Thermoplastic Composite Materials*, 17(3):259–283, 2004.

[30] C. Cinquemani, N. Quick, and M. Nitschke. Verfahren und Halbzeug zur Herstellung eines Faserverbundformteils und Faserverbundformteil, European Patent 2762295, 2013.

[31] Urs Ivan Thomann. *Direct Stamp Forming of Non-Consolidated Carbon/Thermoplastic Fibre Commingled Yarns.* Doctoral thesis, ETH Zürich, 2003.

[32] N. Bernet, V. Michaud, P.-E. Bourban, and J.-A. E. Månson. Commingled yarn composites for rapid processing of complex shapes. *Composites Part A: Applied Science and Manufacturing*, 32(11):1613–1626, 2001.

[33] A. Greco, A. Strafella, C. La Tegola, and A. Maffezzoli. Assessment of the Relevance of Sintering in Thermoplastic Commingled Yarn Consolidation. *Polymer Composites*, 32(4):657–664, 2011.

[34] Martyn D. Wakeman, P. Blanchard, and J.-A. E. Månson. Void evolution during stamp-forming of thermoplastic composites. In *15th International Conference on Composite Materials (ICCM-15)*, Durban, June – July 2005.

[35] R. Hufenus, C. Affolter, M. Camenzind, and F. A. Reifler. Design and characterization of a bicomponent melt-spun fiber optimized for artificial turf applications. *Macromolecular Materials and Engineering*, 298(6):653–663, 2013.

[36] A. K. Moghe and B. S. Gupta. Co-axial Electrospinning for Nanofiber Structures: Preparation and Applications. *Polymer Reviews*, 48(2):353–377, 2008.

[37] Tong Lin, Hongxia Wang, and Xungai Wang. Self-Crimping Bicomponent Nanofibers Electrospun from Polyacrylonitrile and Elastomeric Polyurethane. *Advanced Materials*, 17(22):2699–2703, 2005.

[38] Takeshi Kikutani, J. Radhakrishnan, Sadaaki Arikawa, Akira Takaku, Norimasa Okui, Xia Jin, Fumio Niwa, and Yosuke Kudo. High-speed

melt spinning of bicomponent fibers: Mechanism of fiber structure development in poly(ethylene terephthalate)/polypropylene system. *Journal of Applied Polymer Science*, 62(11):1913–1924, 1996.

[39] J. Radhakrishnan, Takeshi Kikutani, and Norimasa Okui. High-Speed Melt Spinning of Sheath-Core Bicomponent Polyester Fibers: High and Low Molecular Weight Poly(ethylene Terephthalate) Systems. *Textile Research Journal*, 67(9):684–694, 1997.

[40] D. Godshall, C. White, and G. L. Wilkes. Effect of compatibilizer molecular weight and maleic anhydride content on interfacial adhesion of polypropylene-PA6 bicomponent fibers. *Journal of Applied Polymer Science*, 80(2):130–141, 2001.

[41] Frederick T. Wallenberger and Paul A. Bingham. *Fiberglass and Glass Technology Energy-Friendly Compositions and Applications.* Springer Science+Business Media, New York Dordrecht Heidelberg London, 2010.

[42] G. Curran. Bicomponent extrusion of ceramic fibers. *Advanced Materials and Processes*, 148(5):25–27, 1995.

[43] Zhaoyang Liu, Darren Delai Sun, Peng Guo, and James O. Leckie. An Efficient Bicomponent TiO2/SnO2 Nanofiber Photocatalyst Fabricated by Electrospinning with a Side-by-Side Dual Spinneret Method. *Nano Letters*, 7(4):1081–1085, 2007.

[44] Robert L. Houston, Charles F. Rapp, Michael T. Pellegrin, James E. Loftus, and Patrick F. Aubourg. Bicomponent glass and polymer fibers made by rotary process, International Patent WO 97/33841, 1997.

[45] Christiane Freudenberg. *Textile Materials for Lightweight Constructions*, chapter Textile Fiber Materials. Springer-Verlag, Berlin Heidelberg, 2016.

[46] M. Flemming, G. Ziegmann, and S. Roth. *Faserverbundbauweisen: Fasern und Matrices.* Springer-Verlag, Berlin Heidelberg, 1995.

[47] W. Bobeth, H. Faulstich, and A. Mally. *Textile Faserstoffe: Beschaffenheit und Eigenschaften*, chapter Mechanische Eigenschaften. Springer-Verlag, Berlin Heidelberg, 1993.

[48] W. Michaeli and M. Wegener. *Einführung in die Technologie der Faserverbundwerkstoffe.* Carl Hanser Verlag, München Wien, 1989.

[49] B. Wulfhorst, R. Kaldenhof, and K. Hörsting. *Technische Textilien*, volume 36, chapter Faserstofftabelle nach P.-A. Koch: Glasfasern, pages T68–T86. 1993.

[50] M. Mansmann, R. Klingholz, K. Wiedemann, A. F. Kurt, D. Gölden, and D. Overhoff. *Synthesefasern: Grundlagen, Technologie, Verarbeitung und Anwendung*, chapter Anorganische Fasern. Verlag Chemie, Weinheim, 1981.

[51] M. Neitzel, P. Mitschang, and G. Beresheim. *Handbuch Verbundwerkstoffe.* Carl Hanser Verlag, München Wien, 2004.

[52] M. Butler, S. Hempel, and V. Mechtcherine. Zeitliche Entwicklung des Verbundes von AR-Glas- und Kohlenstofffaser-Multifilamentgarnen in zementgebundenen Matrices. In F. Curbach, editor, *Textilbeton – Theorie und Praxis: Tagungsband zum 4. Kolloquium zu Textilbewehrten Tragwerken (CTRS4) und zur 1. Anwendertagung*, pages 213–226, Dresden, June 2009. Technische Universität Dresden.

[53] B. Wulfhorst and G. Becker. *Chemiefasern/Textilindustrie*, volume 39/91, chapter Faserstofftabelle nach P.-A. Koch: Carbonfasern, pages 1277–1284.

[54] Gottfried W. Ehrenstein. *Faserverbund-Kunststoffe: Werkstoffe – Verarbeitung – Eigenschaften.* Carl Hanser Verlag, München Wien, 1992.

[55] B. Clauss. Fasern und Preformtechniken zur Herstellung keramischer Verbundwerkstoffe. In *DGM-Fortbildungsseminar "Keramische Verbundwerkstoffe"*, Würzburg, 2004.

[56] Suter Kunststoffe AG. Fasern und Gewebe – Basalt. *http://www.swiss-composite.ch*, June 2011.

[57] K. L. Loewenstein. *The manufacturing technology of continuous glass fibers.* Elsevier, Amsterdam, 2 edition, 1983.

[58] Oleg Testoni, Andrea Bergamini, Sampada Bodkhe, and Paolo Ermanni. Smart material based mechanical switch concepts for the variation of connectivity in the core of shape-adaptable sandwich panels. *Smart Materials and Structures*, 28(2):25–36, 2019.

[59] Oleg Testoni, Sampada Bodkhe, Andrea Bergamini, and Paolo Ermanni. A Novel Concept of a Modular Shape-Adaptable Sandwich Panel Able to Achieve Multiple Shapes. In *9th ECCOMAS Thematic Conference on Smart Structures and Materials SMART 2019*, Paris, July 2019.

[60] Amaël Cohades and Véronique Michaud. Shape memory alloys in fibre-reinforced polymer composites. *Advanced Industrial and Engineering Polymer Research*, 1(1):66–81, 2018.

[61] Roland Beyreuther and Harald Brünig. *Dynamics of Fibre Formation and Processing: Modelling and Application in Fibre and Textile Industry*. Springer, Berlin Heidelberg, 2007.

[62] Alexander Lüking, Robert Brüll, Thomas Köhler, Davide Pico, Gunnar Seide, and Thomas Gries. One Step Production of Bicomponent Yarns with Glass Fibre Core and Thermoplastic Sheath for Composite Applications. *Key Engineering Materials*, 742:506–511, 2017.

[63] G. W. Morey. *The properties of glass*. Reinhold, New York, second edition, 1954.

[64] A. R. Bunsell. *Composite Materials Series: Fibre Reinforcements for Composite Materials*, volume 2. Elsevier, Amsterdam, 1988.

[65] Harro Hagen. *Glasfaserverstärkte Kunststoffe*. Springer Verlag, Berlin Göttingen Heidelberg, 1956.

[66] T. P. Seward III and T. Vascott, editors. *High temperature glass melt property database for process modeling*. The American Ceramic Society, Westerville, Ohio, 2005.

[67] D. Quéré. Fluid Coating on a Fiber. *Annual Review of Fluid Mechanics*, 31(1):347–384, 1999.

[68] Alejandro G. González, Javier A. Diez, Roberto Gratton, Diego M. Campana, and Fernando A. Saita. Instability of a viscous liquid coating a cylindrical fibre. *Journal of Fluid Mechanics*, 651:117–143, 2010.

[69] L. Landau and B. Levich. Dragging of a liquid by a moving plate. *Acta Physicochimica URSS*, 17:42–54, 1942.

[70] B. V. C. R. Derjaguin. Thickness of liquid layer adhering to walls of vessels on their emptying and the theory of photo- and motion-picture film coating. In *Dokl. Acad. Sci. USSR*, volume 39, pages 13–19, 1943.

[71] David A. White and John A. Tallmadge. A theory of withdrawal of cylinders from liquid baths. *AIChE Journal*, 12(2):333–339, 1966.

[72] Alain De Ryck and David Quéré. Inertial coating of a fibre. *Journal of Fluid Mechanics*, 311:219–237, 1996.

[73] H. R. Stapert, P. J. Dijkstra, and J. Feijen. Synthesis and characterization of aliphatic poly(ester-amide)s containing symmetrical bisamide blocks. *Macromolecular Symposia*, 130:91–102, 1998.

[74] The MathWorks Inc. *Image Processing Toolbox™ User's Guide.* 2018.

[75] Irwin Sobel and Gary Feldman. A 3x3 Isotropic Gradient Operator for Image Processing. In *Stanford Artificial Intelligence Project (SAIL)*, 1968.

[76] Nobuyuki Otsu. A Threshold Selection Method from Gray-Level Histograms. *IEEE Transactions on Systems, Man, and Cybernetics*, 9(1):62–66, 1979.

[77] J. S. Vrentas and C. M. Vrentas. Drying of solvent-coated polymer films. *Journal of Polymer Science Part B: Polymer Physics*, 32:187–194, 1994.

[78] Michael E. Mackay, Tien T. Dao, Anish Tuteja, Derek L. Ho, Brooke van Horn, Ho-Cheol Kim, and Craig J. Hawker. Nanoscale effects leading to non-Einstein-like decrease in viscosity. *Nature materials*, 2:762–766, November 2003.

[79] Anish Tuteja, Michael E. Mackay, Craig J. Hawker, and Brooke Van Horn. Effect of Ideal, Organic Nanoparticles on the Flow Properties of Linear Polymers: Non-Einstein-like Behavior. *Macromolecules*, 38(19):8000–8011, 2005.

[80] Anish Tuteja, Phillip M. Duxbury, and Michael E. Mackay. Multifunctional nanocomposites with reduced viscosity. *Macromolecules*, 40(26):9427–9434, 2007.

[81] Sachin Jain, Johannes G. P. Goossens, Gerrit W. M. Peters, Martin van Duin, and Pieter J. Lemstra. Strong decrease in viscosity of nanoparticle-filled polymer melts through selective adsorption. *Soft Matter*, 4:1848, 2008.

[82] Klaas Nijenhuis, Gareth McKinley, Stephen Spiegelberg, Howard Barnes, Nuri Aksel, Lutz Heymann, and Jeffrey Odell. *Springer Handbook of Experimental Fluid Mechanics*, chapter Non-Newtonian Flows, pages 619–743. Springer, Berlin, Heidelberg, 2007.

[83] Albert Einstein. Eine neue Bestimmung der Moleküldimensionen. *Annalen der Physik*, 324(2):289–306, 1906.

[84] E. Guth and R. Simha. Untersuchungen über die Viskosität von Suspensionen und Lösungen. 3. Über die Viskosität von Kugelsuspensionen. *Kolloid-Zeitschrift*, 74(3):266–275, 1936.

[85] Sachin Jain, Han Goossens, Francesco Picchioni, Pieter Magusin, Brahim Mezari, and Martin van Duin. Synthetic aspects and characterization of polypropylene-silica nanocomposites prepared via solid-state modification and sol-gel reactions. *Polymer*, 46(17):6666–6681, 2005.

[86] Charles A. Harper. *Handbook of plastics technologies: the complete guide to properties and performance.* McGraw-Hill handbooks. McGraw-Hill, New York, 2006.

[87] Michael L. Hair. Hydroxyl groups on silica surface. *Journal of Non-Crystalline Solids*, 19:299–309, 1975.

[88] T. B. Lewis and L. E. Nielsen. Viscosity of Dispersed and Aggregated Suspensions of Spheres Viscosity of Dispersed and Aggregated Suspensions of Spheres. *Transactions of the Society of Rheology*, 12(3):421–443, 1968.

[89] Bernard P. Binks and Tommy S. Horozov, editors. *Colloidal Particles at Liquid Interfaces.* Cambridge University Press, August 2006.

[90] Gerald G. Fuller and Jan Vermant. Complex fluid-fluid interfaces: rheology and structure. *Annual review of chemical and biomolecular engineering*, 3:519–543, 2012.

[91] André R. Studart, Urs T. Gonzenbach, Elena Tervoort, and Ludwig J. Gauckler. Processing Routes to Macroporous Ceramics: A Review. *Journal of the American Ceramic Society*, 89(6):1771–1789, 2006.

[92] Ilke Akartuna, Elena Tervoort, Joanna C.H. Wong, André R. Studart, and Ludwig J. Gauckler. Macroporous polymers from particle-stabilized emulsions. *Polymer*, 50(15):3645–3651, 2009.

[93] B. Scheid, J. Delacotte, B. Dollet, E. Rio, F. Restagno, E. a. van Nierop, I. Cantat, D. Langevin, and H. a. Stone. The role of surface rheology in liquid film formation. *EPL (Europhysics Letters)*, 90(2):24002, 2010.

[94] S. Tharmalingam and W. L. Wilkinson. The coating of Newtonian liquids onto a rotating roll. *Chemical Engineering Science*, 33(11):1481–1487, 1978.

[95] S. Tharmalingam and W. L. Wilkinson. The coating of Newtonian liquids onto a roll rotating at low speeds. *Polymer Engineering and Science*, 18(15):1155–1159, 1978.

[96] Makrolon® 3108 ISO Datasheet. Covestro AG Polycarbonates Business Unit, Edition 30.11.2017.

[97] SiLibeads Glaskugeln Typ SL Produktdatenblatt. Sigmund Lindner GmbH, Version V14/2017.

[98] Timothy G. Gutowski, editor. *Advanced Composites Manufacturing*. John Wiley & Sons, New York, 1997.

[99] P. Ermanni, editor. *Script for ETH lecture 151-0548-00L Manufacturing of Polymer Composites*. Zürich, fourth edition, 2017.

[100] C. Ageorges, L. Ye, and M. Hou. Advances in fusion bonding techniques for joining thermoplastic matrix composites: a review. *Composites Part A: Applied Science and Manufacturing*, 32(6):839–857, 2001.

[101] L. J. Bastien and J. W. Gillespie. A non-isothermal healing model for strength and toughness of fusion bonded joints of amorphous thermoplastics. *Polymer Engineering & Science*, 31(24):1720–1730, 1991.

[102] C. McIlroy and P. D. Olmsted. Disentanglement effects on welding behaviour of polymer melts during the fused-filament-fabrication method for additive manufacturing. *Polymer*, 123:376–391, 2017.

[103] Z. Dobkowski. Influence of molecular weight distribution and long chain branching on the glass transition temperature of polycarbonate. *European Polymer Journal*, 18(7):563–567, 1982.

[104] G. C. Berry and T. G. Fox. The viscosity of polymers and their concentrated solutions. *Advances in Polymer Science*, 5:261–357, 1968.

[105] Martin Eichenhofer, Joanna C.H. Wong, and Paolo Ermanni. Continuous lattice fabrication of ultra-lightweight composite structures. *Additive Manufacturing*, 18:48–57, 2017.

LIST OF PUBLICATIONS

The following provides a list of publications and student reports related to this thesis which Christoph Schneeberger has authored, co-authored, or supervised.

Journal articles

- Christoph Schneeberger, Joanna C.H. Wong, and Paolo Ermanni. Hybrid bicomponent fibres for thermoplastic composite preforms. *Composites Part A: Applied Science and Manufacturing*, 103:69–73, 2017.

Conference contributions

- Nicole Aegerter, Christoph Schneeberger, Shelly Arreguin, Joanna C. H. Wong, and Paolo Ermanni. A scalable process for making hybrid bicomponent fibers for the efficient manufacturing of thermoplastic composites. In *4th International Conference & Exhibition on Thermoplastic Composites (ITHEC 2018)*, Bremen, Germany, October 2018.

- Nicole Aegerter, Christoph Schneeberger, Joanna C. H. Wong, and Paolo Ermanni. Empirical Optimization of Kiss-Roll Coating for High-Speed Bicomponent Fibre Production. In *Proceedings of the SAMPE Europe Students Conference 17*, Stuttgart, Germany, November 2017.

- Christoph Schneeberger, Nicole Aegerter, Joanna C. H. Wong, and Paolo Ermanni. Manufacture of Hybrid Bicomponent Fibers by Kiss-roll Coating. In *21st International Conference on Composite Materials (ICCM-21)*, Xi'an, China, August 2017.

- Christoph Schneeberger, Joanna C. H. Wong, and Paolo Ermanni. Bicomponent Polymer/Glass Fibres for Stamp Forming. In *Proceedings of the SAMPE Europe Conference 16*, Liège, Belgium, September 2016.

- Christoph Schneeberger, Joanna C H Wong, and Paolo Ermanni. Manufacturing of Bicomponent Fibers for Thermoplastic Composites: A Feasibility Study. In *17th European Conference on Composite Materials (ECCM17)*, Munich, Germany, June 2016.

Student theses and reports

- Sara Birk. The Consolidation Behavior of Hybrid Bicomponent Fiber Preforms. *Master's thesis*, ETH Zürich, August 2019.
- Philipp Keller. Life Cycle Analysis of Hybrid Bicomponent Fiber Production. *Bachelor's thesis*, ETH Zürich, June 2019.
- Kerstin Unmüssig. Formability Testing of Hybrid Thermoplastic Noncrimp Fabrics. *Bachelor's thesis*, ETH Zürich, May 2019.
- Manuela Heinrich. Concept for an Automotive Demonstrator Component Stamp Formed from Bicomponent Fibers. *Bachelor's thesis*, ETH Zürich, May 2019.
- Philipp Bischof. Thermomechanical Modelling for the Consolidation of Hybrid Bicomponent Fiber Preforms. *Semester thesis*, ETH Zürich, May 2019.
- Ivo Marti. Cost Analysis of Hybrid Bicomponent Fiber Production. *Bachelor's thesis*, ETH Zürich, December 2018.
- Paul Schwager. Continuous Fabrication of Hybrid Bicomponent Fibers. *Semester thesis*, ETH Zürich, June 2018.
- Nicole Aegerter. Empirical Optimization of Kiss Roll Coating for High-Speed Bicomponent Fibre Production. *Master's thesis*, ETH Zürich, September 2017.
- Audrey Blondé. Numerical Modeling of Dip Coating for the Fabrication of Bicomponent Fibers. *Semester thesis*, ETH Zürich, June 2017.
- Dominik Kläusler. Characterization of Hybrid Yarns for Press Processes. *Semester thesis*, ETH Zürich, June 2017.

- Jialu Chen. Investigation of Nanofilling on the Coating Process for the Manufacture of Bicomponent Fibers. *Internship report*, ETH Zürich, April 2017.
- Nicole Aegerter. Experimental Investigation of Fluid Coating Methods on the Microscale. *Master project II*, ETH Zürich, January 2017.
- Vincent Werlen. Investigation of Continuous Fiber Coating Processes for the Lab Scale Manufacture of Thermoplastic Sheath Bicomponent Fibers. *Semester thesis*, ETH Zürich, June 2016.

CURRICULUM VITAE

Christoph Schneeberger
born on June 7th 1988 in Rothrist AG
citizen of Madiswil BE
married to Elena Schneeberger

Education

2015 – 2020	Doctor of Science ETH at the Laboratory of Composite Materials and Adaptive Structures
2013 – 2015	Master of Science ETH in Mechanical Engineering
2009 – 2012	Bachelor of Science ETH in Mechanical Engineering
2004 – 2008	Swiss Federal Matura, Kantonsschule Zofingen

Professional career

since 2020	Pioneer fellow at ETH Zürich
2019	Visiting researcher at the Laboratory of Engineering Materials, University of Calgary
2015 – 2020	Scientific assistant at the Laboratory of Composite Materials and Adaptive Structures, ETH Zürich
2013	Engineering intern at business unit Instruments & Tools, Helbling Technik, Wil SG
2012 – 2013	Engineering intern at series development of conventional springs/dampers, BMW Group, Munich
2011 – 2012	Teaching assistant at the Centre of Structure Technologies, ETH Zürich

Current appointments

since 2015	Member of the Society for Advancement of Material and Process Engineering (SAMPE), Swiss chapter
since 2011	Member of the Society of Automotive Engineers (SAE)

Past appointments

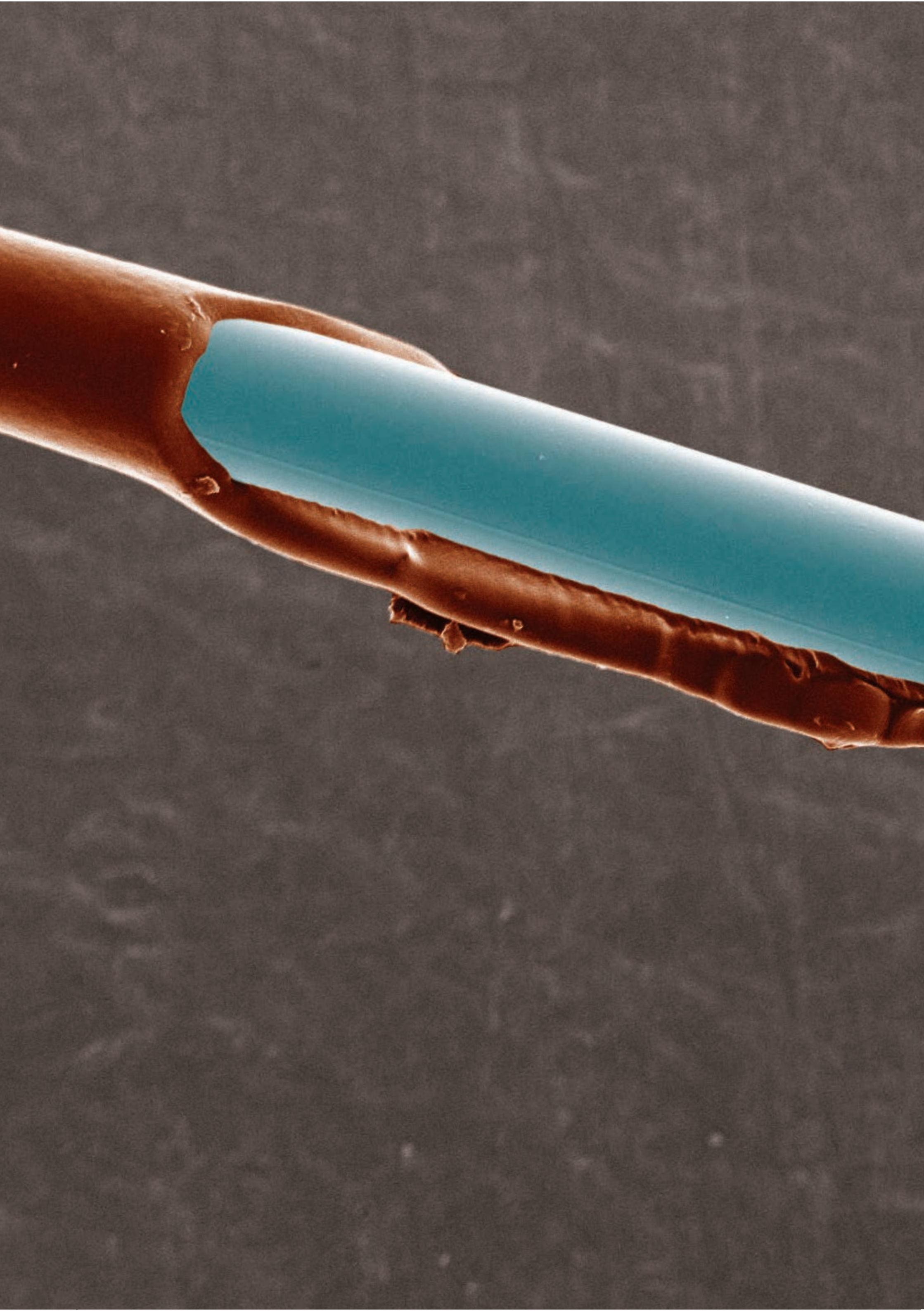2015 – 2020	Alumnus of the SCCER Mobility research program
2010 – 2012	Alumnus of the Academic Motorsports Club Zurich (AMZ)